This is to certify that the

dissertation entitled

"Time-Resolved Fluorescence From Sodides"

presented by

Guangzhou Xu

has been accepted towards fulfillment
of the requirements for

Ph.D. degree in Chemical Physics

James L. Dye
Major professor

Date 14 July 1992

TIME-RESOLVED FLUORESCENCE FROM SODIDES

by

Guangzhou Xu

A DISSERTATION

Submitted to
Michigan State University
In partial fulfillment of the requirements
for the degree of

DOCTOR OF PHILOSOPHY

Department of Chemistry

1992

ABSTRACT

TIME-RESOLVED FLUORESCENCE FROM SODIDES

by
Gaungzhou Xu

Fluorescence from Sodium Cryptand[2. 2. 2.] ($Na^+C222Na^-$) as well as from other sodides has been investigated. Most of the studies were done on $Na^+C222Na^-$ at temperature below 77 K and at low excitation densities, such that the fluorescence could be observed reversibly over three orders of light intensities.

The shape of the fluorescence spectra was found to fit a Gaussian function on the high energy side of the peak, and to obey Urbach's rule on the low energy side; that is, the spectrum on the low energy side exhibits an exponential dependence on the emission energy. When the temperature is raised, a logarithmic plot of the intensity shows a lower slope and the straight lines at different temperatures converge at approximately one point, another characteristic of the Urbach rule.

When the temperature is raised above 77 K the fluorescence spectrum has structure. For example, two bands with peak energies at 1.847 eV and 1.822 eV are observed at 125 K.

Time-resolved fluorescence from $Na^+C222Na^-$ was extensively studied by using a single-photon counting system in which a 6-ps pulsed dye laser was employed as the excitation source. It was found that, in addition to radiative emission, intra-band and interband spectral transfers also take place. The intra-band transfer occurs between a state centered at approximately 1.847 eV (state A) and a state at 1.822 eV (state B).

At high excitation densities, fluorescence bleaching and recovery processes occur.

The fluorescence spectra from ten sodides were found to have common properties. For example, the main emission band is structureless, most of them have a Stoke's shift of about 0.1 eV and the lifetimes have plateau shapes as functions of energy. However, the fluorescence intensity from the other sodides is at least three orders of magnitude weaker and the decay time constants are much shorter than those of $Na^+C222Na^-$. It was also observed that the decay time constants of defect-doped $Na^+C222Na^-$ are shorter than those of undoped samples.

Optical absorption studies of thin films of $Na^+C222Na^-$ and $Rb^+(15C5)_2Na^-$ were carried out at 121 K to 270 K. When the temperature increases, the absorbance on the low energy side of the spectrum, which has approximately the same position as that of fluorescence at low temperature, increases slightly for T<200 K, but dramatically above 200 K.

The observations are explained and discussed by using the concepts of excitons, energy transfer, phonons, traps and local temperatures.

ACKNOWLEDGEMENTS

I would like to express my sincere gratitude to my Ph. D. adviser, Professor James L. Dye for his constant support and guidance during the course of this research. I thank my other guidance committee Professors: James Harrison (who taught me Quantum Chemistry also), William P. Pratt, Jr., Subhendra D. Mahanti (who taught me Solid State Physics also), Daniel G. Nocera (who taught me Inorganic Chemistry and kindly allowed me to use his fluorescence photospectrometer for this study also). I appreciate Professor Estelle McGroarty for her financial support during my first year of graduate study and the time before, which makes the things happened today, possible.

Appreciation is also extended to all of the members of my research group with whom I have worked, in particular Rui-He Huang, Jineun Kim, Marc G. De Backer, Ahmed S. Ellaboudy, Dae-Ho Shin, Kuo-lih Tsai and Professor Solin's group, T. Park, P. Zhou for their advice, support and cooperation.

I am grateful to have received financial support from the National Science Foundation grants Nos. 87-17763 and 90-24525.

Thank to those people in my motherland and in the United States, who helped me. Thanks to my mother, to my sister, Shusan, Shuzen and my brothers for their encouragement and help. Finally a special "thank you" goes to my wife, Mingsong, my daughter, Xiaolin, and my son, Chunxiao, whose deep love to me was the driving force in the completion of this degree.

TABLE OF CONTENTS

LIST OF FIGURES

CHAPTER I

INTRODUCTION

1. Sodides.

Sodides are compounds with the formula $M^+C_nNa^-$ where M^+ represents the alkali metal cation, n = 1 or 2, and C represents the complexant. Three representative complexants, 18-crown-6 (18C6), Cryptand [2.2.2] (C222) and Hexamethyl Hexacyclen (HMHCY) are shown in Fig. 1.1.

Sodides belong to a class of compounds called *alkalides*. There is another new class of compounds called *electrides* which are closely related to the *alkalides*. An *electride* has the formula $M^+C_ne^-$ where M^+, n and C have the same meaning as for *alkalides*, while e^- represents an electron. *Alkalides* and *electrides* were discovered and have been investigated in Dye's Laboratory at Michigan State University during the last two decades.[1.1-1.6] Pictures of alkalide and electride crystal structures have been published on the cover pages of "NATURE" and "SCIENTIFIC AMERICAN" and a photograph of $Na^+C222Na^-$ is featured in a "GENERAL CHEMISTRY" textbook. [1.7-1.9] In the *alkalide* family there are also *potassides* (K^-), *rubidides* (Rb^-) and *cesides* (Cs^-). They have the same formula as sodides except that the alkali metal anion is different. For example, when Na^- in the formula of $M^+C_nNa^-$, is substituted by K^-, we have *potassides*, and so on. In *electrides*, the position of Na^- is occupied by an electron.

A number of physical properties of sodides have been studied. For example, powder DC conductivity measurements show that the

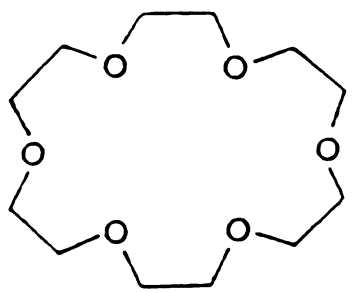

18 Crown-6

A

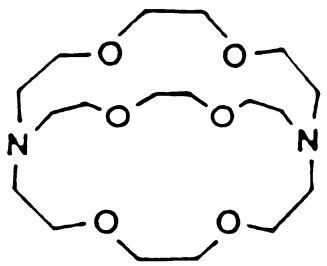

Cryptand-2.2.2

B

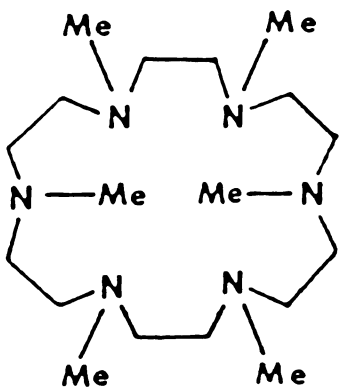

HMHCY

C

Fig. 1.1. Representative complexants: A), 18-crown-6 1,4,7,10,13, 16- Hexaoxacyclooctadecane); B), Cryptand [222] (1,4,13,16,21,24-Hexaoxa-1,10-diazabicyclo [8.8.8] Hexacosane); C), HMHCY (1,4,7,13,16-Hexaaza-1,4,7,13,16-Hexamethylcyclooctadecane).

parent compound, $Na^+C222Na^-$, has a band gap of 2.5 eV which is within the range of semiconductors.[1.10, 1.11] The absorption spectrum of a thin film of $Na^+C222Na^-$ consists of a broad band with a width of about 0.37 eV, and a high energy shoulder. [1.12] At about 150 K, the peak energy of the band is at 2 eV and the shoulder is at approximately 2.5 eV. Recently it was also observed that at low temperature, single crystals subjected to blue or yellow light emit luminescence which has a lifetime of about 5 ns at 20 K. The luminescence has a peak energy of 1.85 eV at 7 K and a bandwidth of 30 meV. It was also observed that the emission band shifts to the red with time. The observations of the original photoluminescence study were well-explained with a model that had two energy levels.[1.13]

The optical and electronic properties of this compound were not yet fully understood at the start of this research. A number of questions remained. For example, how does the absorption and emission change with temperature? What is the line shape of the emission spectrum, and how does it change with temperature? How does the emission respond to changes in the excitation energy, excitation intensity, and duration of the excitation? And how will the emission be affected if we dope the sodide with defects (trapped electrons)? All the questions mentioned above are the subjects that have been studied and will be reported in this dissertation.

2. Introduction to Luminescence.

A one dimensional band structure for a non-metallic crystalline solid is shown in Fig. 1.2. In this figure, there are two bands, the V

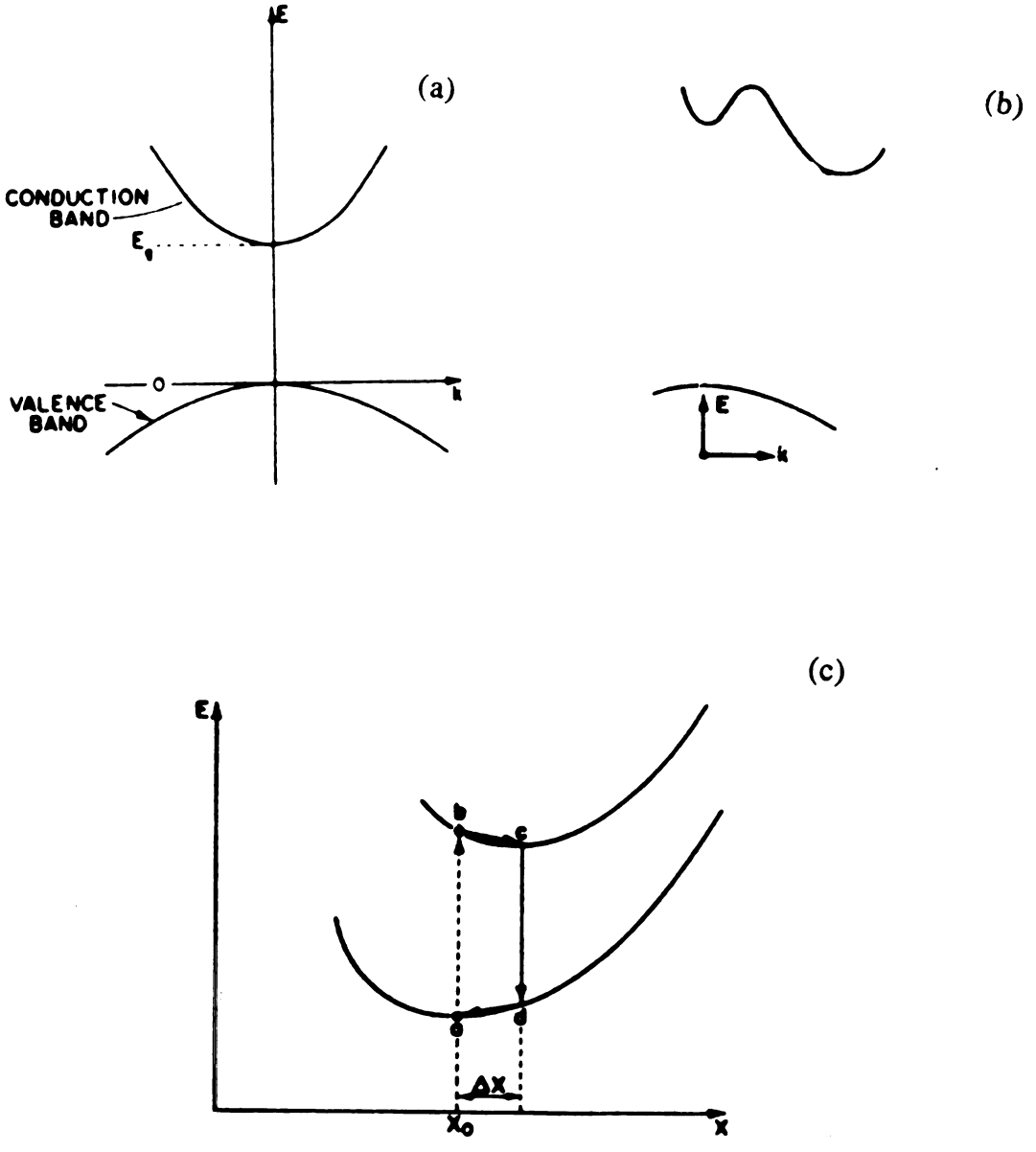

Fig. 1.2. Energy vs. momentum in a two-band system. (a) has a direct-gap, (b) has an indirect-gap. (c). The C.C (Configuration Coordinate) diagram.

(valence) band and the C (conduction) band with a band gap energy value $E_g = E_C - E_V$, where E_C is the energy of the bottom of the C band and E_V is the energy value of the top of the V band. For insulators, the E_g values are much larger than the energy of visible light which has an energy range of about 1 to 3 eV. The reason that we normally do not study pure insulators optically is that insulators have large band gaps, which makes them transparent to light. However, optical studies are very powerful in the case of materials which have excited state energy levels within the visible region.

Absorption and luminescence processes are demonstrated in Fig. 1.2 as shown in (a) for a direct transition and (b) for an indirect transition. The absorption process corresponds to the electronic transition from the V band to the conduction band, while an emission process corresponds to the reverse process. In (a) of Fig. 1.2, the lowest point of the conduction band has the same value of the wave vector as that at the top of the valence band. In optical studies a photon absorbed or emitted has a very small wave vector, and the absorption or emission corresponds to a vertical transition Therefore, for a direct gap, a transition between the minimum of the conduction band and the top of the valence band yields the energy gap E_g. The indirect transition in (b) involves both a photon and a phonon, because the band edge of the conduction band and the valence band are widly separated in K space.

The configuration coordinate diagram, Fig. 1.2 (c) is very useful in examining optical processes in which phonons are involved. In (c) the horizontal axis represents either the position or the rate of position change of the emission center. The vertical axis represents energy. The lower curve in the diagram is the ground state energy curve, and the upper curve represents the first excited state. In both states there are vibrational levels of the lattice which correspond to the phonon energies. According to the theories of solid state physics, there are two kinds of phonon modes, transverse and longitudinal. For each mode there are two branches, optical and acoustical, depending on the dispersion relation in k-space. In Fig. 1.2 (c), the transition from a to b corresponds to an absorption process. The center then relaxes from b to c. The relaxation process takes place rapidly, in about 10^{-13} seconds in crystals. Phonons are emitted during this relaxation process. When the center returns to its ground state, from c to d, luminescence light can be emitted. The center can relax to the original configuration a by emitting phonons. The energy absorbed in the transition a-->b is higher than the energy emitted in the transition c-->d. The difference between the two energies is called the Franck-Condon shift or Stokes shift.

The emission signal decays with time. We assume that it has roughly an exponential decay function, $I(E,t)$, with a decay time constant τ. When τ is in the range of ns, by convention the emission process is called fluorescence. If τ is much longer than ns, i. e. ms to seconds, the process is called phosphorescence. Normally allowed transitions have shorter lifetimes, which gives fluorescence, and

forbidden transitions have longer lifetimes, which gives phosphorescence. The term luminescence includes both fluorescence and phosphorescence. Luminescence differs from the light emitted by an incandescent body, such as black body radiation, in which the emitting material is hot. Therefore, luminescence can be described as cold light emission.

Depending on the excitation methods used, luminescence can take a variety of forms such as photoluminescence, cathodoluminescence, X-ray luminescence, thermoluminescence, chemiluminescence, bioluminescence, electroluminescence and so on. When the luminous material is excited with ultraviolet or visible radiation the emission induced by the excitation is called photoluminescence. If it is excited by bombardment of electrons or X-rays, it is called cathodoluminescence or X-ray luminescence respectively. Thermoluminescence is excited with thermal excitation. Chemiluminescence and bioluminescence follow by chemical or biochemical reaction. Electroluminescence is excited by applying an electric field to the material.

Photoluminescence is the most common method used for luminescence studies because the excitation can be easily adjusted. By using lasers we have broad freedom to select the excitation energy, intensity, polarization and pulse width. From now on, we will use the term luminescence to mean photoluminescence, because we only use light as the excitation source.

Light emitted from a pure crystal is called intrinsic luminescence. We consider a pure crystal as: (a) perfect in periodicity of the crystal lattice and (b) accurate in stoichiometry.

But in reality, we can only find approximations to pure crystals. For example, trapped electrons can be detected by EPR (Electron Paramagnetic Resonance). In this sense it is possible to obtain $Na^+C222Na^-$ as nearly pure crystals, because EPR results show that there are only trace amounts of trapped electrons found in the compound. Compared with $Na^+C222Na^-$, other sodides always have significant concentrations of trapped electrons. [1.11]

3. Principles of Fluorescence Lifetime Measurements with Single-Photon Counting Systems.

The principle of the technique for single-photon counting relies on the following fact: the evolution probability of one photon being emitted from a sample is the same as for all of the photons. This is based on a statistical principle (ergodic hypothesis) which says that, the time average of the photon ensemble is equal to the ensemble average of the system.[1.14]

The data collected by a single-photon counting system is a convolution of the real fluorescence decay curve with the response of both the excitation and the detection instrumentation. In a standard photon-counting system, such as that used in this study, the width of the exciting laser pulse is only 6 ps. Compared with the lifetime, which is the order of ns, the excitation can be considered to be a delta function. Under this condition we can get a real luminescence decay curve by deconvoluting the signal with P(E,t), the Instrument Response Function or IRF, where E is energy. The function P(E,t) represents the response of the instrument, mainly the photomultiplier tube, to the excitation without sample. The observed

fluorescence decay curve $I_{obs}(E,t)$ is related to the real decay function $I(E,t)$ by the convolution integral:

$$I_{obs}(t) = \int_0^t P(t')\ I(t-t')\ dt' \qquad (1.1)$$

The real decay curve can be obtained by using a trial function for $I(t)$ to fit the experimental data. The data can be analyzed by using a commercial software program [1.15] in which it is possible to use up to four exponentials:

$$I(t) = \Sigma\ a_i\ \exp(-t/\tau_i) \qquad i = 1 \text{ to } 4 \qquad (1.2)$$

In this expression τ_i and a_i represent the decay time constant and the pre-exponential factor, respectively for the luminescence step i. Once the real decay curve is obtained, we can synthesize (reconstruct) the spectra to yield time-resolved fluorescence spectra.[1.15]

References

1.1). J. L. Dye, J. M. Ceraso, M. T. Lok, B. L. Barnett and F. J. Tehan, J. Am. Chem. Soc. 96, 608, (1974).

1.2). F. J. Tehan, B. L. Barnett, and J. L. Dye, J. Am. Chem. Soc. 96, 608, (1974).

1.3). J. L. Dye, Prog. Inorg. Chem. 32, 327 (1984).

1.4). J. L. Dye, Scientific American, 257 (1987). J. L. Dye J. Phy. Chem., 1980. 84, 1084

1.5). J. L. Dye J. Phy. Chem., 1984. 88, 3842.

1.6). J. L. Dye Pure Appl. Chem., 1989. 61, 1555.

1.7). See cover page of "Nature", London, vol. 331, No. 6157 (1988).

1.8). See cover page of "Sientific American" Sept. 1987.

1.9). See Chang's GENERAL CHEMISTRY" text book 1990.

1.10). Papaioanou, J., Jaenicke, S., Dye, J. L., Solid. State. Chem. 67 (1987) 122.

1.11). K. J. Moeggenborg, Dissertation, MSU 1990

1.12). Jaenicke, S., Faber, M. K.; Dye, J. L.;Pratt, Jr.,W. P. J. Solid State Chem. 1987, 68, 239-246.

1.13). Banwart, R. S., Solin, S. A., De Baker, M. G. and Dye, J. L. J.Am. Chem. Soc. 111 (1989) 5552.]

1.14).C.H. Wang, Spectroscopy of condenced media, Chapter 1, 1985.

1.15). O'Connor, D.; Phillips, D. Time-correlated Single Photon Counting; Academic Press; London, 1984.

CHAPTER II

EXPERIMENTATION

1. Sample Preparation

1.1. Glassware cleaning.

The glassware was first treated with an HF solution which contains 28 M HF, acid detergent, HNO_3 and deionized water with 5, 2, 35 and 60 V/V percentages respectively. The glassware was rinsed with deionized water five times, then filled with freshly prepared *aqua regia* (3 HCl/1 HNO_3) and allowed to remain for ten hours. The glassware was then rinsed with deionized water 5 times, followed by seven rinses with conductance water. The cleaned glassware was oven-dried at about 200 ^{o}C overnight and the openings were covered with laboratory Para-film before the glassware was used.

1.2. Sample Preparation.

The preparation of sodides has been described in detail elsewhere.[2.1, 2.2, 2.3] Alkali metal(s) and complexant were introduced into a K-cell of the type shown in Fig. 2.1 in a helium glove box. Complexant was loaded through channel B to chamber C, to which the fingers for crystal harvest were attached. The K-cell was removed from the helium glove box and was evacuated to a pressure of 2 x 10^{-5} torr. At the same time the temperature in chamber C which contained complexant, was kept low with dry ice. The Ultra-

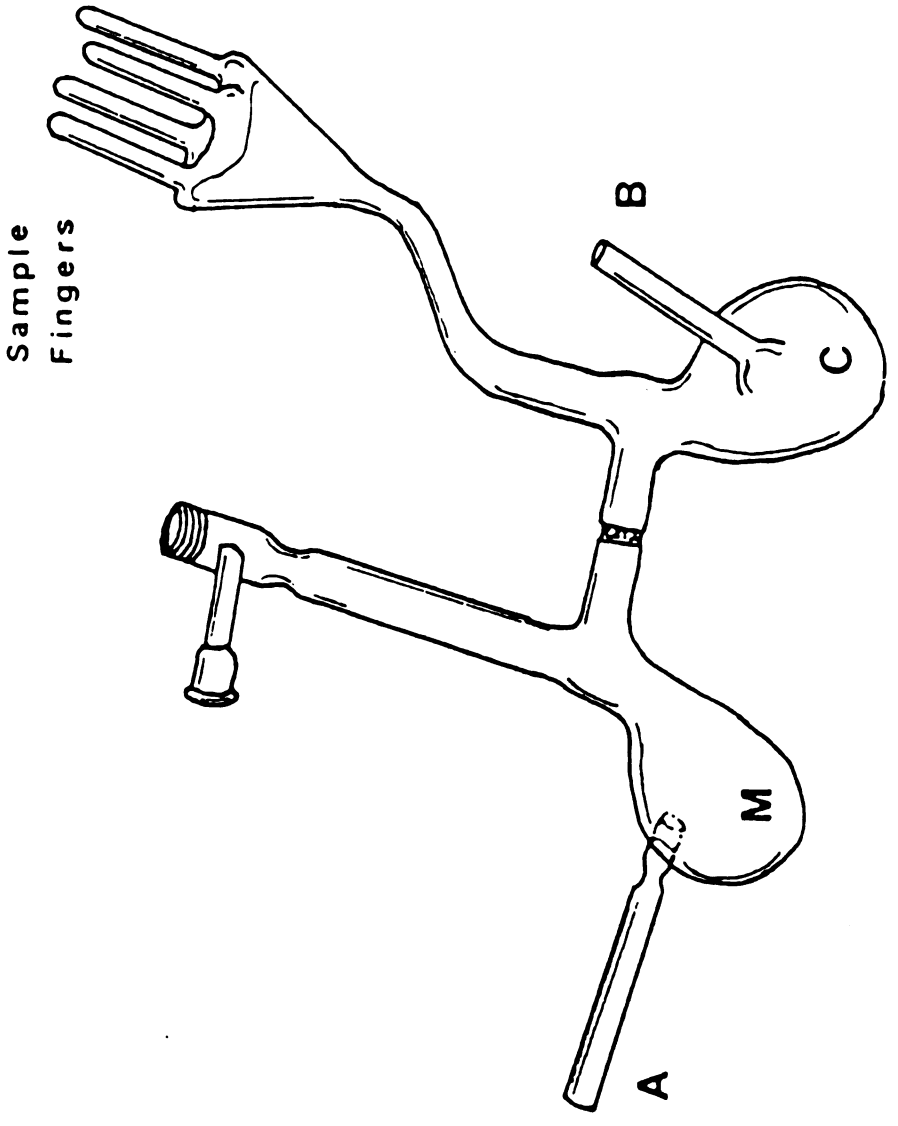

Fig. 2.1. Apparatus (K-cell) used in synthesis of sodides.

Torr unions (Cajon) and closed end glass caps were removed by a vacuum seal-off of the glass side arm. The metal was then distilled to form a thin shiny metal mirror in chamber M. [2.4]

The side-arms were removed and both chamber were immersed into a bath which contained dry ice and isopropanol. Methyamine, the solvent used to dissolve the complexant and the metal, was then added by distillation into the compartment. After the complexant had been dissolved in the solvent, the solution was poured into the other side to dissolve the mirror. Then the solution was poured back and forth several times until all the complexant was dissolved. The solution was poured into chamber M when the process was completed. To harvest the solid compounds, a collection bottle was kept at liquid nitrogen temperature to remove part of the solvent. Trimethylamine was added as a co-solvent to precipitate the polycrystalline alkalides. Solvents were then poured off and the crystals were washed with solvent distilled into the chamber and finally dried by evacuation. The K-cell was removed from the vacuum line and cooled by being placed into a large cold chamber for three to five minutes while the Teflon stopper was kept warm with a cotton cloth. The polycrystals were distributed into the cold fingers and the fingers were immersed into liquid nitrogen (LN) in a Dewar before the fingers warmed up. The fingers were flame-sealed off and stored in LN before being used.

To avoid any possible introduction of an impurity metal, all the metallic tools for complexant handling were substituted by non-metallic ones. The molar ratio of alkali metal and complexant was carefully controlled when loaded into the K-cell. In order to dope

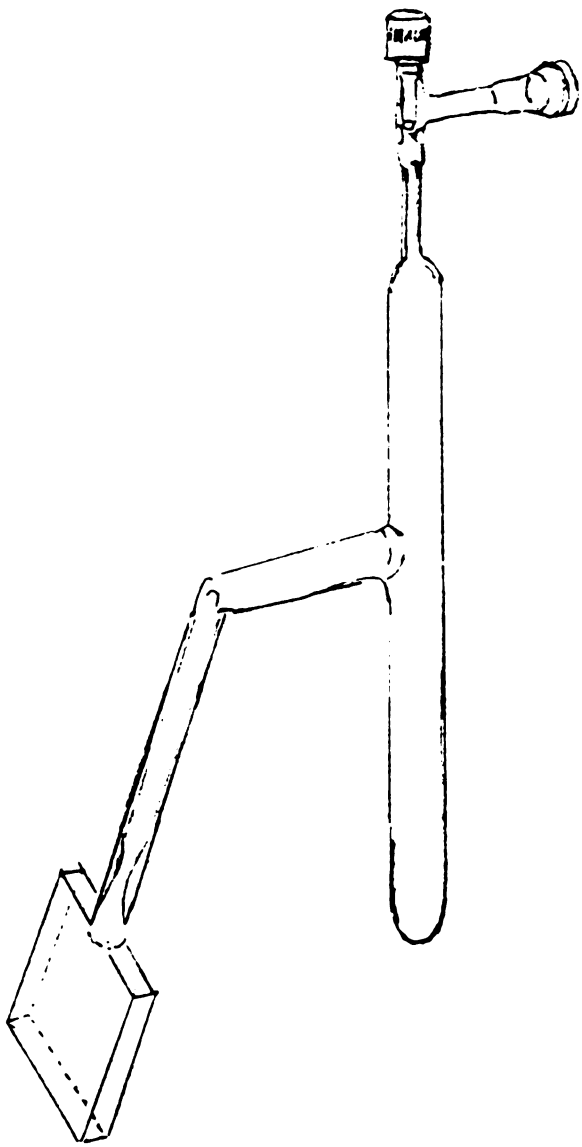

Fig. 2.2. Apparatus used to prepare sodide films.

defects or trapped electrons into $Na^+C222Na^-$, the ratio of C222 to Na metal was controlled to be 1:1.

Preparation of $Na^+C222Na^-$ and $Rb^+(15C5)_2Na^-$ films.

A cell in the shape of an "h" as shown in Fig. 2.2, was used for film preparation. The right side branch was used to load sodide single crystals while the other side consisted of an optical quartz cell at the bottom of the branch. The lower part of the left branch was made from a quartz optical cell with an interior dimension of 2 mm x 5 mm x 5 mm.

One to two mg sample of sodide crystals was loaded into the right-hand tubing under an atmosphere of inert gas. The crystals were then dissolved in methylamine or dimethylether at temperatures below -20 ^{o}C. The solution was poured into the quartz cell with the whole apparatus, except the stopcock, kept at -50 ^{o}C or lower. Then the optical cell was shaken vigorously, while keeping the other side of the "H" cell at 77 K. With a temperature gradient applied in this way, the solution in the quartz cell evaporated rapidly and a film was formed on the quartz window. This process was repeated until a uniform blue, transparent film was formed. Before being sealed off in LN, the cell was filled with helium gas up to about 10^{-3} torr. The sample was then stored in LN.

Preparation of single crystals of $Na^+C222Na^-$ from polycrystals.

The initial sample was a saturated methylamine $Na^+C222Na^-$ solution containing co-solvent (either trimethylamine or diethyl ether). The solution was in a K-cell and the temperature was about

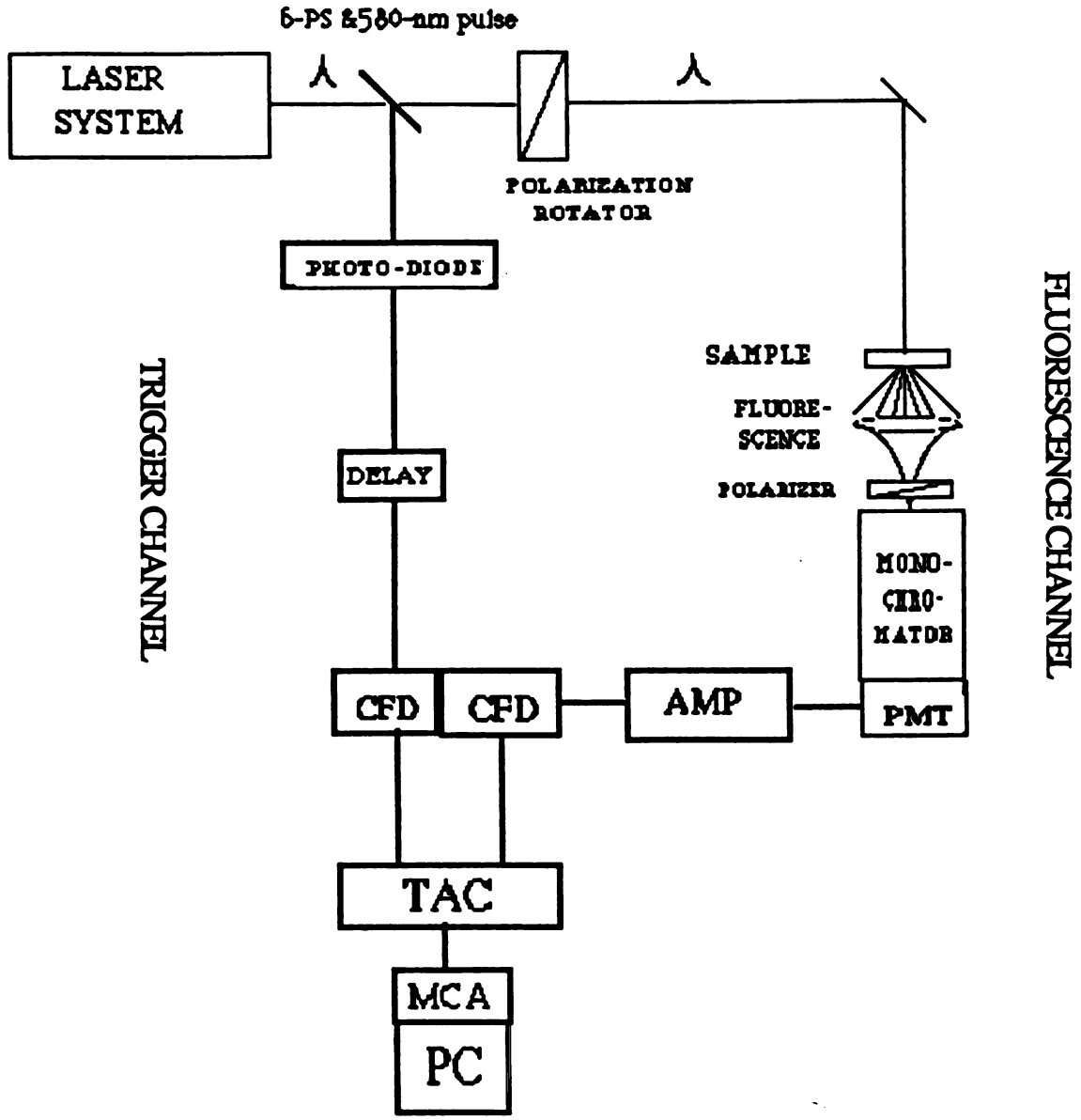

Fig. 2.3. Diagram of the single-photon counting system used to obtain decay curves and time-resolved fluorescence spectra. CFD, constant fraction discriminator; PMT, photo multiplier tube; AMP, amplifier; TAC, time-to-amplitude convertor; MCA, multi-channel-analyzer; PC, personal computer.

-20 °C. The cell was placed in a programmable NESLAB LT-9 ethanol-filled bath at -20 °C. The temperature of the bath was scanned from -20 to -70 °C over a 48 hr period. During the slow cooling process, single crystals grew, starting on the bottom of the K-cell. The mother liquor, solvent and co-solvent, were poured away and distilled into a liquid nitrogen trap. Single crystals were harvested and stored as described before.

2. Absorption Studies.

Optical absorption studies of thin films of $Na^+C222Na^-$ and $Rb^+(15C5)_2Na^-$ were carried out at 120 K to 270 K. A Guided Wave, model 260 Fiber Optical Spectrophotometer was used. The model provides a microcomputer (IBM-PC) to control the spectrophotometer and to analyze the data collected. The resolution of the spectrophotometer can be adjusted. For the absorption study of the two sodides, the resolution was 2 nm.

To control temperature, a cooling chamber was used. The chamber has two plane quartz windows with a diameter of one inch for each. The two windows are parallel to each other. The temperature of the chamber was adjusted by nitrogen gas passing through. The temperature of the nitrogen gas was 120 K to 300 K. The flat quartz optical cells containing the sample films were mechanically fixed between the windows in the chamber. The temperature was monitored by a thermocouple next to the sample cell.

The films actually consist of microcrystals with an average size of *nanometers*. Because the film is not uniform, the absorbance of one

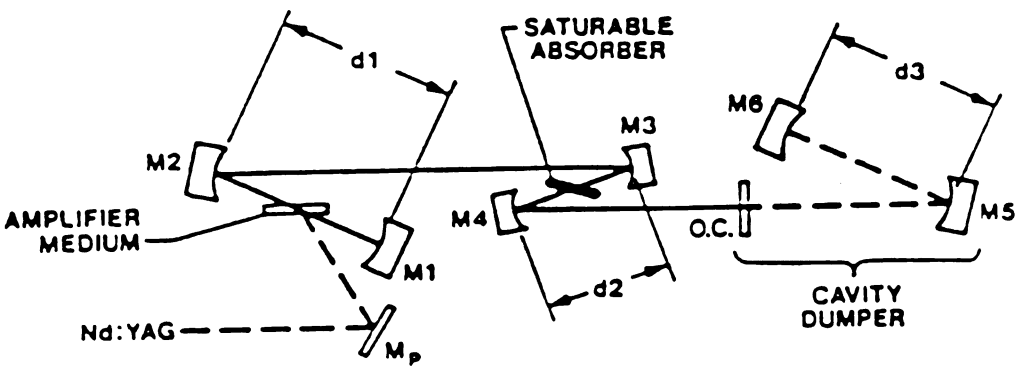

Fig. 2.4. Diagram of dye laser configuration.

illuminated spot may be different from that of another. Therefore, to study the effect of temperature on absorption, the data collected and analyzed were from one spot only. The general results were then reproduced at other spots.

3. Fluorescence Spectroscopy

3.1. Conventional Fluorescence Spectroscopy

Excitation spectra and some of the steady-state luminescence spectra were obtained by using an emission spectrometer constructed at Michigan State University.[2.5] The excitation beam of the spectrometer originated from a 150 W Xe lamp, mounted in a Spex 1909 lamp housing (f/4). The light was focused onto the entrance slit of a Spex 1680A double monochromator (0.22 m, f/4). The wavelength-selected excitation light, was collimated by a f/4 fused silica lens, and focused onto the sample cell with a f/l fused silica lens. The luminescence signals emitted from the sample were collected at 90 degrees to the excitation beam and then focused by a second lens (f/8). The emission light was detected by a Hamamatsu R1104 photomultiplier tube which was kept at - 62 ^{o}C with Dry Ice powder. The signal from the PMT was passed through a LeCroy VV 100B single-channel fast-pulse amplifier to the input of an EG & G Model 128A lock- in amplifier. The input signal to the lock-in amplifier was phase-matched to the reference signal generated by a PAR Model 125A light chopper which was located between the excitation monochromator and the sample chamber. The output from

the lock-in amplifier was fed into a Soltec Model 124A strip chart recorder and also collected by a Zenith ZQ-151-52 minicomputer.

3.2. Instrumentation of the single-photon counting system

The diagram of a single-photon-counting system used in this study is shown in Fig. 2-3. The overall system consists mainly of a two-laser system (a), and a detection system (b).

3.2.1). Laser system.

The laser system includes two pulsed lasers, a Nd:YAG laser and a dye laser. The laser beam used for the kinetics study is from the dye laser, which is synchronously pumped by the Nd:YAG laser.

3.2.1.1). Dye laser.

The dye laser used in this study is a Coherent 702-CD system, which is diagrammed in Fig. 2-4. The dye used is rhodamine 6G in glycose solution. The rhodamine 6G solution absorbs the light coming from the Nd:YAG laser and emits a broadened emission band peaking at a wavelength of 580 nm, which makes the dye laser tunable within the range of 560 nm to 618 nm, with its peak power at 580 nm. The repetition rate of the dye laser pulse, 1 MHz, is controlled by the cavity dumper (CD). The pulse shape is monitored by an autocorrelator (Femtochrome FR-103). The autocorrelator has a rotating parallel pair of mirrors, a second harmonic generator and a PMT. The function of the rotating mirrors is to maintain a periodically alternating time delay in one arm of a Michelson interferometer. The split and then combined beam with time delay

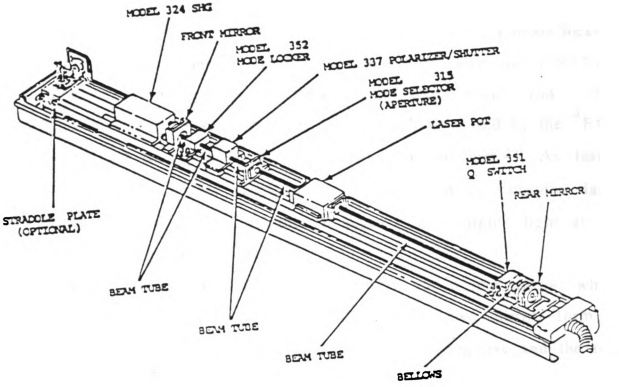

Fig. 2.5. Location of the components of the Nd:YAG pulse laser.

is focused onto a nonlinear crystal and the generated second harmonic is detected by the PMT and monitored with an oscilloscope.

3.2.1.2). Nd:YAG pulse laser.

The Nd:YAG laser (Quantronix 416 MLSH), as shown in Fig. 2-5, serves as a laser pump for the dye laser. This pumping laser basically consists of four parts: (a), laser head, (b), a front and a rear mirror, (c), SHG (second Harmonic Generator) and (d) a mode locker.

(a), The laser head consists of a krypton arc lamp and a Nd:YAG (Yttrium Aluminum Garnet doped with Neodymium) rod. The Nd:YAG has a 1064 nm resonance line which is caused by the $^4F_{3/2}$ <--> $^4I_{11/2}$ transition of the Nd in the YAG medium.[2.6] As lasing occurs, the Nd:YAG rod absorbs energy from the krypton lamp (krypton emits strongly in the IR region) and outputs light at the transition frequency of the Nd.

(b), There are also two mirrors, a front and a rear mirror, which are mounted parallel to the laser head. These two mirrors form an optical resonator. The front mirror is 12% transmissive and the rear one is heavily reflective. By using a differential micrometer, the distance between the two mirrors can be adjusted. During operation, a distance change of only one μm has a noticeable effect on the pulse width and the pulse-to-pulse timing jitter. Therefore, an Invar rod which connects the two mirrors is used to stabilize the resonance condition.

(c) The function of the SHG (second Harmonic Generator) is to convert the 1064-nm light to 532-nm light.

(d). To get picosecond (ps) pulses from the dye laser, the pumping beam must also be pulsed. In the Nd:YAG laser, this pulsing is realized by mode-locking. The mode-locker is an acoustic-optic modulator acting as a fast optical gate. When mode locked, harmonically spaced resonator modes have a coherent phase relation.[2.6] Under this condition, it has a repetitively pulsed output. When the period of the loss modulation is exactly equal to the round trip transit time of photons in the resonator, a pulse traverses the modulator during the low loss state on every succeeding pass. The intensity of such a pulse grows to have a stable value. On the other hand, pulses traversing the modulator at a time period of high loss are unable to grow. As a result, the output beam from the Nd:YAG laser is pulsed.

3.2.2). Detection System

3.2.2.1). Conventional Applications.

This single-photon counting system can be used as a conventional spectrophotometer. Fig. 2.3 gives the schematic diagram for both static and kinetic studies. In the figure, the fluorescence signal is collected and passed through a double monochromator (Model 25-100 Jarrell-Ash One Meter Double Czerny-Turner Scanning Spectrometer), which has a double grating configuration and 1800 grooves per mm. The focal length used is 1 m and the f-number is 8.7, so that it matches the external optical system precisely. The monochromator can be set at any wavelength manually or by using a stepping motor controlled by commercial software. The fluorescence signal is then amplified and converted to an electronic signal by a

photomultiplier tube (Hamamatsu R955) which is thermoelectrically cooled to 20 °C. The electronic signal is then amplified and either displayed on a rate meter or recorded by a chart recorder.

3.2.2.2). Application to Kinetics Studies.

Fig. 2.3 is the diagram of the single-photon counting system used also for lifetime studies. To measure the lifetimes at a fixed emission wavelength, the system works as follows:

1). A pulsed dye laser beam splits into a main beam and a minor beam. The main beam follows the fluorescence channel to excite the sample and the minor beam is used for the trigger channel.

2). In the trigger channel, to which the minor beam is conducted, the laser pulse is converted to an electrical signal and starts the charging of a capacitor in a time-to-amplitude converter (TAC).

3). In the fluorescence channel, only a fraction of the main beam is absorbed and a luminescence signal is emitted by the sample.

4). The emitted fluorescence is collected by two optical lenses, then passed through the monochromator and amplified by the PMT which amplifies and converts the signal from the optical mode into an electronic signal.

5). The electronic signal is amplified again by an amplifier and re-shaped by a discriminator (Tennel TC 455). Then it stops the charging of the capacitor in the TAC.

6). The TAC provides a pulsed output voltage, which is directly proportional to the charge on the capacitor, or equivalently, to the time period between the start and the stop pulses.

7). The pulsed voltage output signal from the TAC is input to a computer and converted into a digital signal by using a commercial multi-channel-analyzer (PCA) by which each count is stored in the appropriate channel of the PCA. The data are then transferred automatically to the computer.

8). The decay data of instrument response function (IRF) is obtained similarly, but in this case, only very weak excitation light is allowed to enter the monochromator and the PMT. To do so, the monochromator is set at a resonance wavelength, and the entrance slit of the monochromator is blocked by paper).

3.3. Monitoring of excitation intensity and sample temperature.

3.3.1). Monitoring of excitation intensity.

The laser power was monitored by a power meter which can be recorded directly by a chart recorder or by a programmed voltmeter (Keithly Model 199 System DMM/Scanner). The voltmeter is equipped with an analog-to-digital converter to convert the excitation intensity to a voltage value and transferred to the PCA.

3.3.2). Sample temperature control.

In the fluorescence study, the sodide sample was contained in a 4-mm OD quartz EPR tube which was held by a copper holder. The holder was attached directly to the cold finger in a helium closed-cycle optical cryostat (CTI-Cryogenics). A thermal sensor was mechanically fixed on the sample holder. The EPR tube was clamped onto the holder at 120 K to prevent any possible decomposition, with

a glove bag flushed with pure nitrogen to prevent ice condensation onto the EPR tube.

References

2.1). Mary L. Tinkham, Ph.D. Dissertation, Michigan State University, (1985).

2.2). Ahmed S. Ellaboudy, Ph.D. Dissertation, Michigan State University, (1984).

2.3). B. Van Eck, L. D. Le, D. Issa and J. L. Dye Inorg., Chem., 1982, 21, 1966.

2.4). A. L. Wayda, and J. L. Dye, J. Chem. Educ., 62, 356 (1985).

2.5). Mussell, R. D., and Nocera, D. G.,J. Am. Chem. Soc. 110 (1988) 2764.

2.6). B. Couillaud and V. F. Bellani, Lasers & applications, 79-83 (1985)

CHAPTER III

FLUORESCENCE FROM $Na^+C222Na^-$ AT LOW TEMPERATURE AND LOW EXCITATION DENSITY

It was found that the florescence spectra depend on many factors, for example, the sample temperature, excitation density, excitation duration and sample preparation.

1. The steady-state absorption and fluorescence spectra of $Na^+C222Na^-$ at 10 K.

Typical absorption and fluorescence spectra from $Na^+C222Na^-$ are shown in Fig. 3.1. The absorption spectrum was from a solvent-evaporated thin film while the fluorescence spectrum was from an assembly of $Na^+C222Na^-$ single crystals.

The absorption spectrum consists of a major band and a shoulder. The major absorption band has a peak energy of 2.05 eV at 10 K. The shoulder of the absorption spectrum has a maximum at about 2.5 eV.

From Fig. 3.1 we see that the emission band, which will later be referred to as the G_V band, has the following relationship to the absorption band:

a). The whole emission band is within the absorption band.

b). The peak position of the emission band which is at 1.84 eV, is 0.16 eV below the absorption peak.

2. The shape of the G_V fluorescence band.

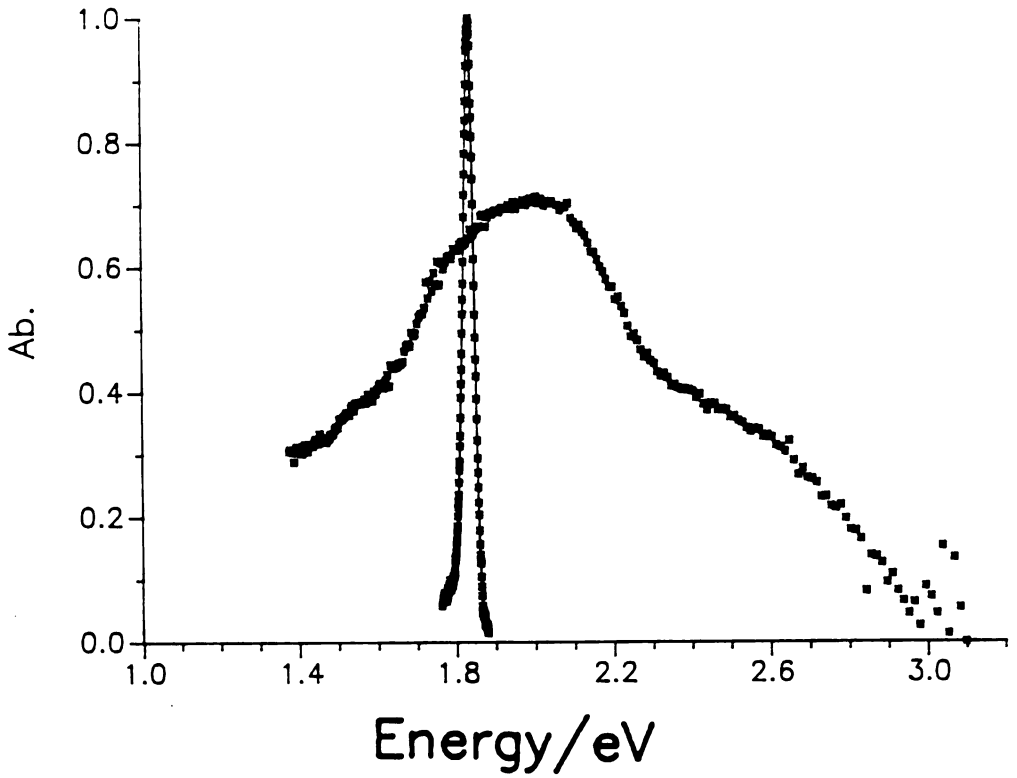

Fig. 3.1. Optical absorption (broad) and luminescence (narrow) spectra of $Na^{+}C222Na^{-}$ at 10 K.

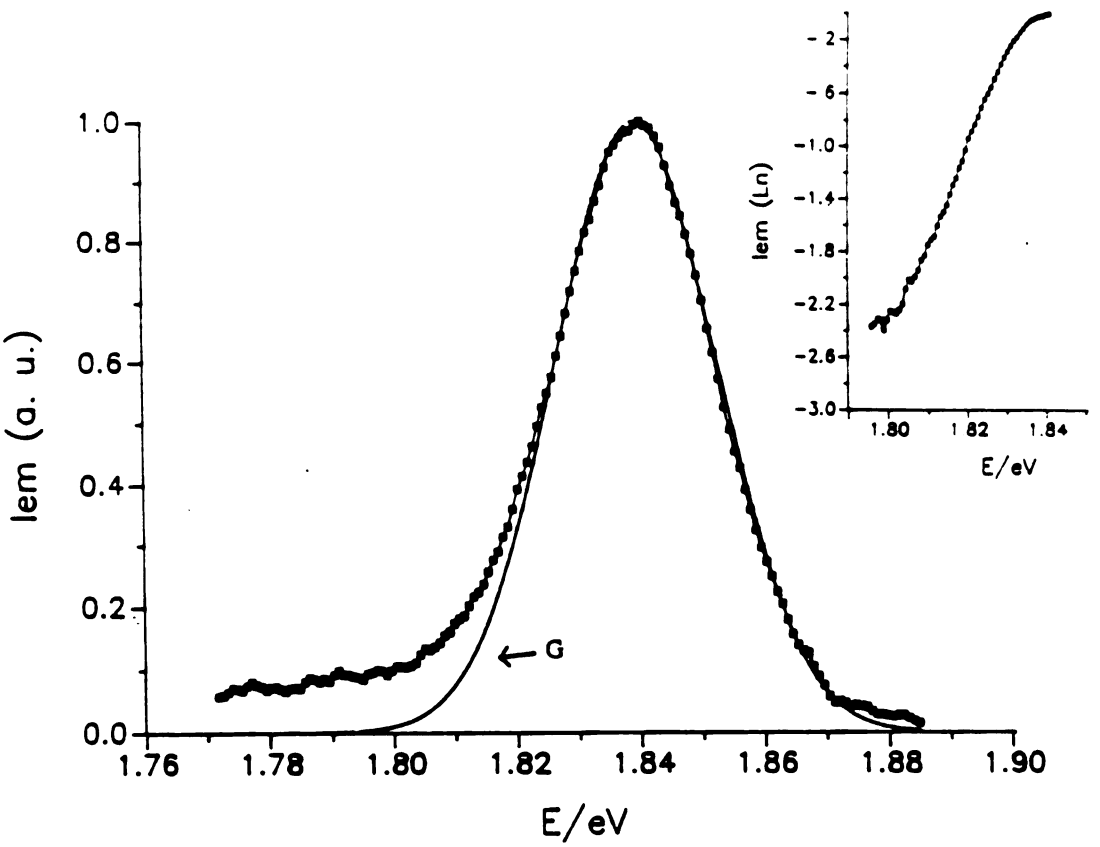

Fig. 3.2. Band shape for the fluorescence spectrum shown in Fig. 3.1. The solid line shows a Gaussian fit to the data. The inset shows the logarithmic behavior on the low-energy side, referred to as an "Urbach tail".

The shape of the emission spectrum shown in Fig. 3. is characterized as follows:

(a). The main fluorescence spectrum which includes the high energy side (v-side) and the vicinity of the spectral peak, has a Gaussian shape.

(b). The peak position of the Gaussian function is at 1.84 eV, which is the same as that of the whole G_V band.

(c). The FWHM (full width at half maximum) of the Gaussian function and the whole G_V band are 26 meV and 30 meV respectively.

(d). The low-energy-side of the spectrum is logarithmic in the energy at shown in the inset to Fig. 3.2.

3. The temperature dependence of the G_V band-shape.

The fluorescence spectra at temperatures of 10 K to 49 K are plotted in Fig. 3.3. Fig. 3.4 shows the temperature dependence of the fluorescence intensity at the peak position (as a semi-log plot). From these figures we find that:

(a). As shown in Fig. 3.3, as the temperature increases the intensity on the high energy side of the spectrum decreases more rapidly than that on the low energy side.

(b). As plotted in Fig. 3.4, the fluorescence intensity at the peak position decrease approximately linearly with temperature.

We can now analyze the shape of the fluorescence spectra on the low energy side. For clarity, each spectrum is normalized to its own maximum intensity, before making a log plot. Also only the

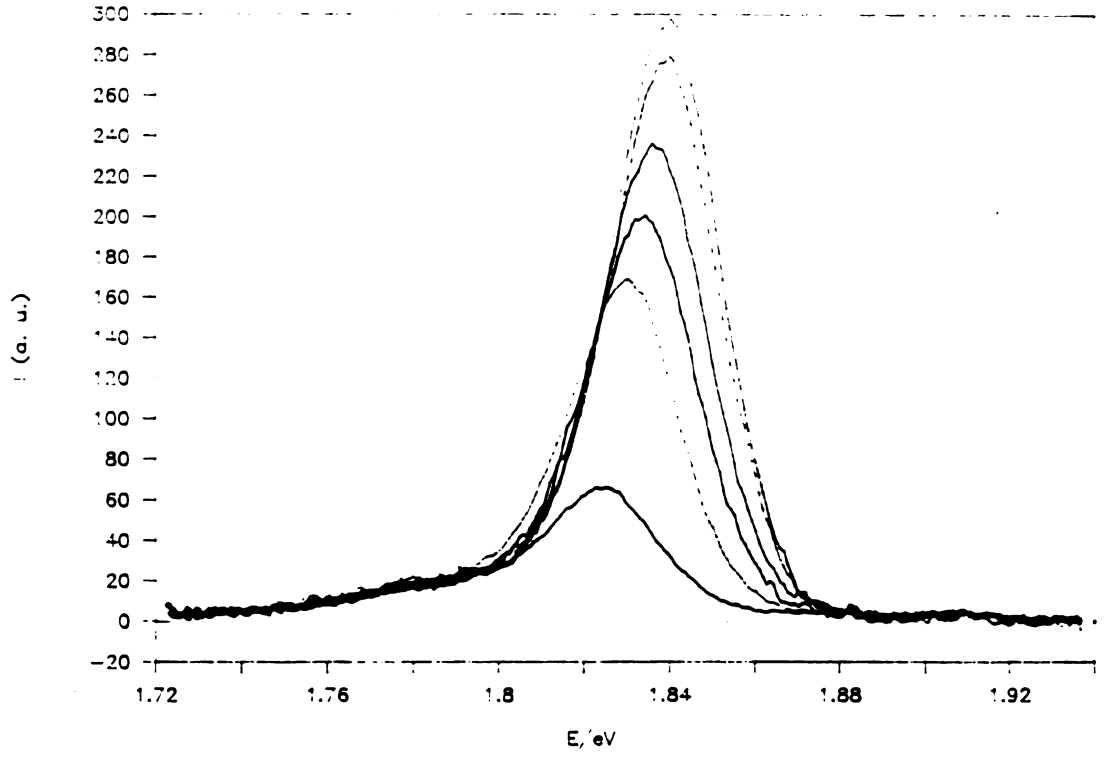

Fig.3.3. Static fluorescence spectra of $Na^{+}C222Na^{-}$ at temperatures of, from the top to the bottom, 10 K, 15 K, 22.5 K, 25 K, 30 K and 39 K.

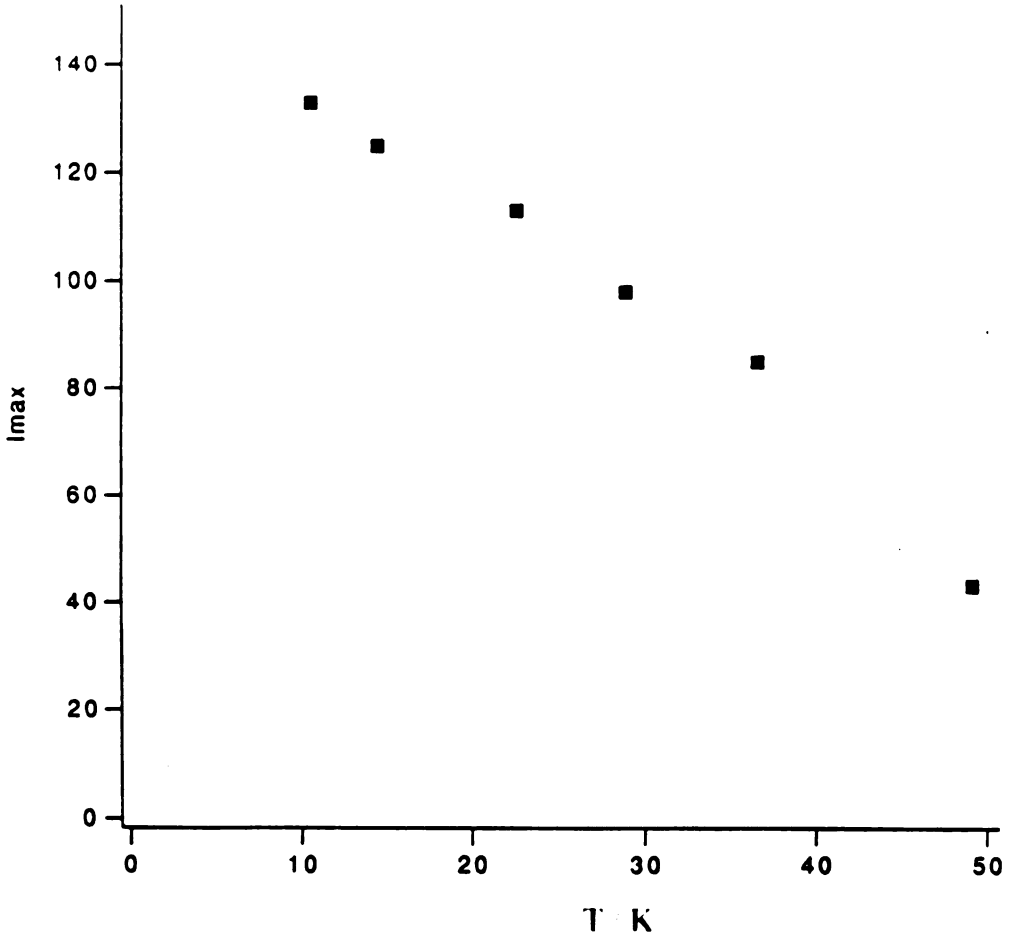

Fig. 3.4. Dependence of the fluorescence intensity at the peak energy on temperature for $Na^{+}C222Na^{-}$.

spectra on the low energy side are considered. The results are shown in Fig. 3.5. From the figure we can see that:

(a). Over the whole temperatures range studied, the log of the emission intensity is a linear function of the energy nearly up to the energy at the maximum.

(b). As temperature decreases, the slope becomes steeper.

(c). The lines approximately converge at a single energy. As discussed in the next chapter, these features are characteristic of the Urbach rule.[3.1]

4. Energy mismatch observed by time-resolved spectra.

Time-resolved fluorescence spectra and spectral differences are shown in Figs. 3.6 and 3.7 respectively. The spectrum with a small sharp peak in Fig. 3.6 was obtained at zero delay time while the subsequent spectra are separated from each other by 60 ps. The delay time is defined as the time that has elapsed after excitation. Fig. 3.6 shows that the fluorescence intensity on the high energy side decays more rapidly than that on the low energy side. In addition, the emission peak shifts to the red as it decays.

The time-resolved difference spectrum is constructed as follows:

(a). Each "instantaneous" spectrum, $s_p(t)$, was first obtained by using a commercial program[1.15] and/or programs written in BASIC (see the Appendix for this chapter). The origin of delay time t can be arbitrarily chosen for this purpose.

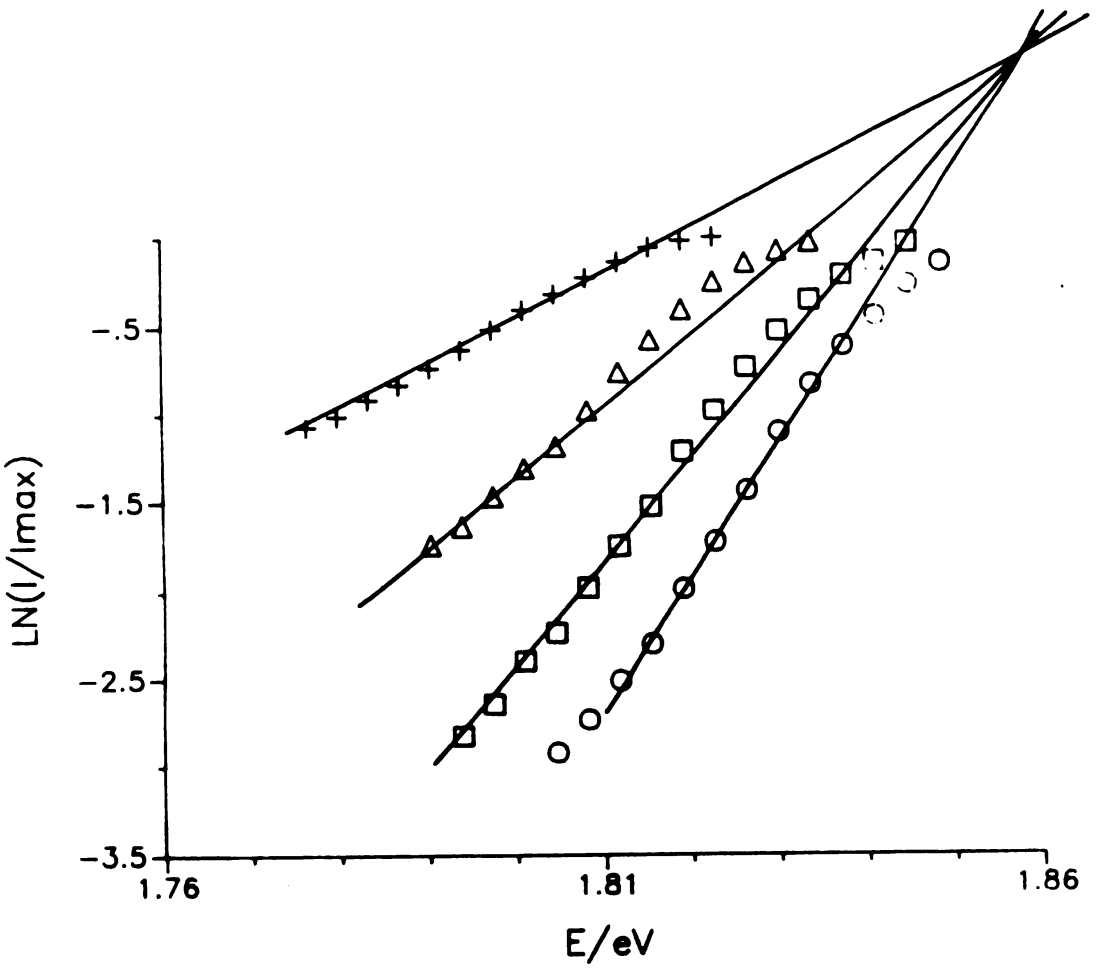

Fig. 3.5. Log plot of the fluorescence intensity for $Na^{+}C222Na^{-}$ on the low-energy side of the spectra at various temperatures after normalized. Temperatures for the data points are, from right to left, 25 K, 35 K, 50 K and 80 K.

(b). A correction for the radiative decay of the normalized spectra is made by multiplying by $\exp(t/\tau)$, an exponential factor, where τ is the radiative decay constant, 5.048 ns. In fact, this normalization does not affect our conclusion because we consider the spectral shape change only.

(c). From each spectrum obtained in step (b), the spectrum at long times (t=15 ns) was subtracted.

The difference spectra are shown in Fig. 3.7. The figure shows that:

(a). Each difference spectrum consists of two components that are separated at E^* =1.835 eV. When $E > E^*$, the difference spectra are positive, which corresponds to extra intensity at short times that is lost at later times. When $E < E^*$, the difference spectra are negative, which corresponds to relative intensity gain as time increase.

(b). As the delay time increases, the magnitudes of both components decrease, but the magnitude of the negative component decreases more slowly than that of positive component.

(c). The energy difference, ΔE, between the two peak positions of the two components, remains approximately invariant at 25 meV.

5. Energy mismatch observed from steady-state spectra at various temperatures.

The spectral differences shown in Fig. 3.8 were constructed from the steady-state spectra shown in Fig. 3.3. The procedure is as follows:

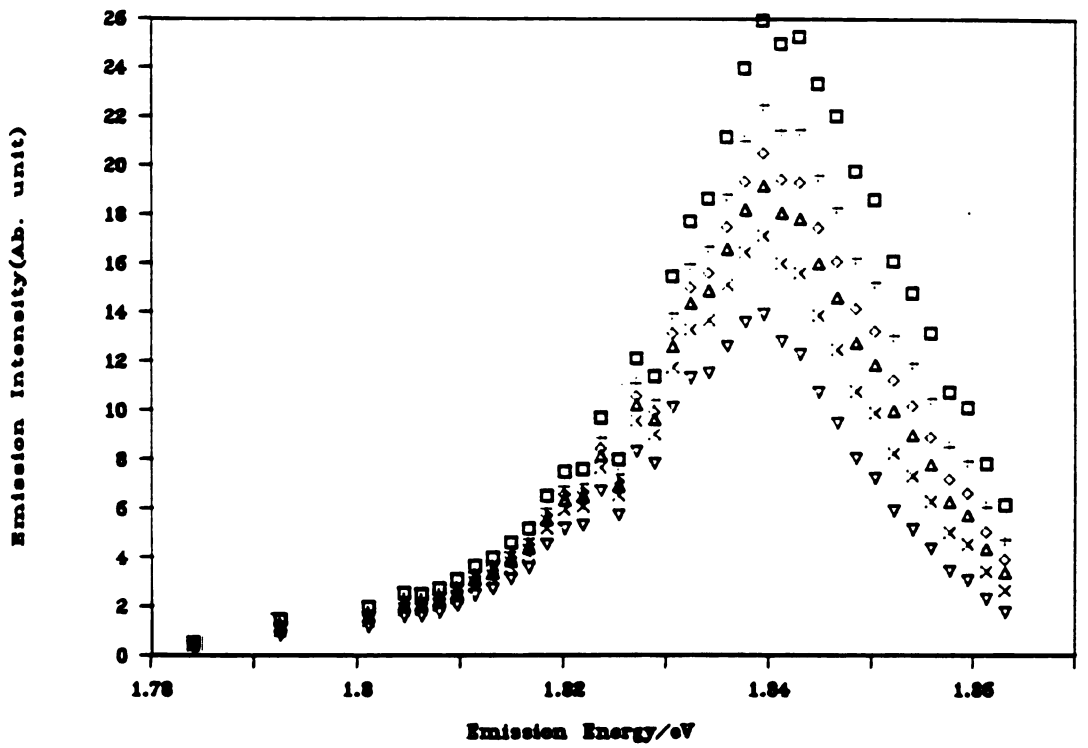

Fig. 3.6. Time-resolved fluorescence spectra for $Na^{+}C222Na^{-}$ at 26 K. There is a delay time difference of 60 ps between the successive spectra in this figure.

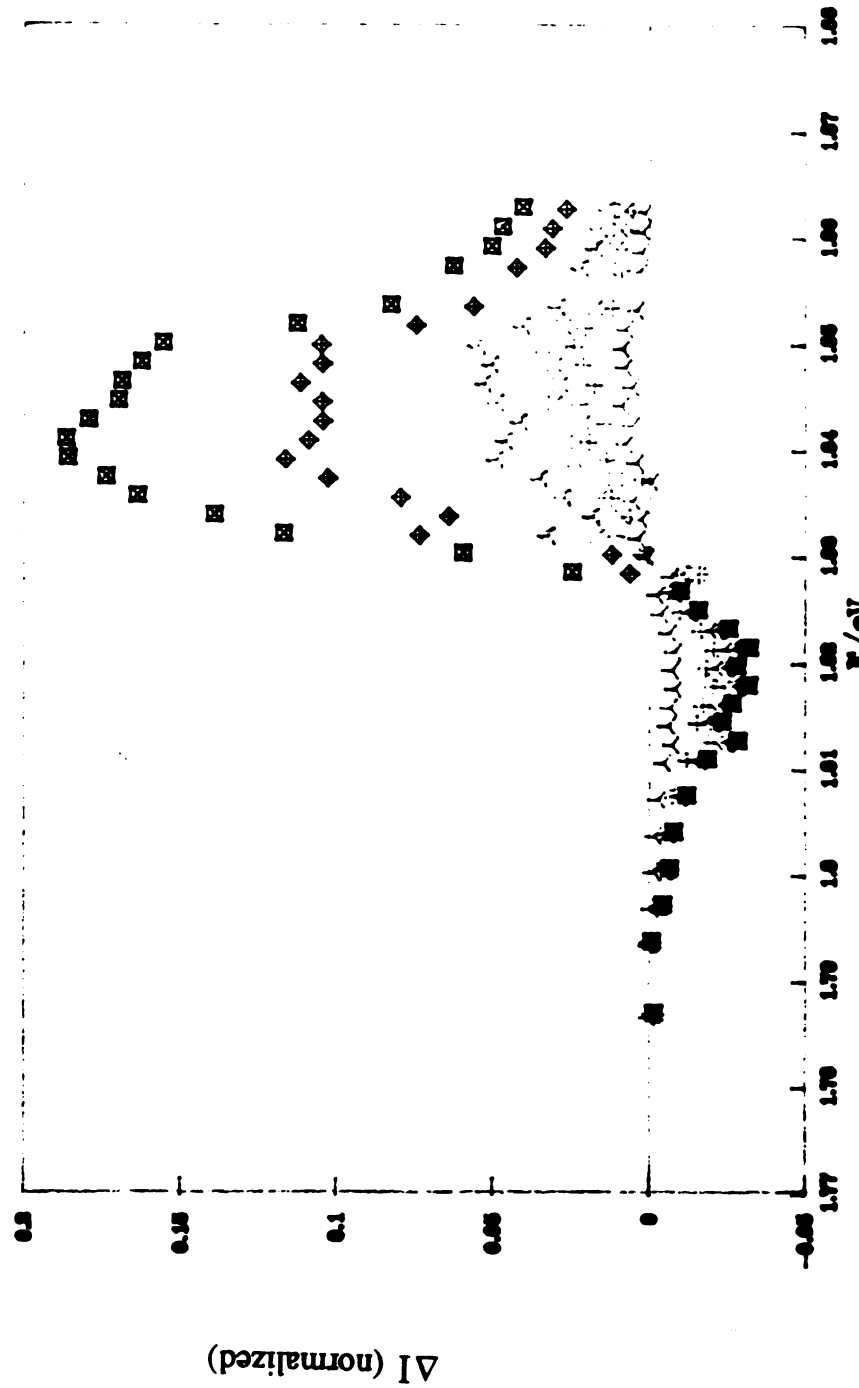

Fig. 3.7. Time-resolved fluorescence difference spectra for $Na^+C222Na^-$ at 26 K. Times from top to bottom on the right are 1, 2, 4, 6, 8, and 15 ns. See the text for details of the normalization procedure.

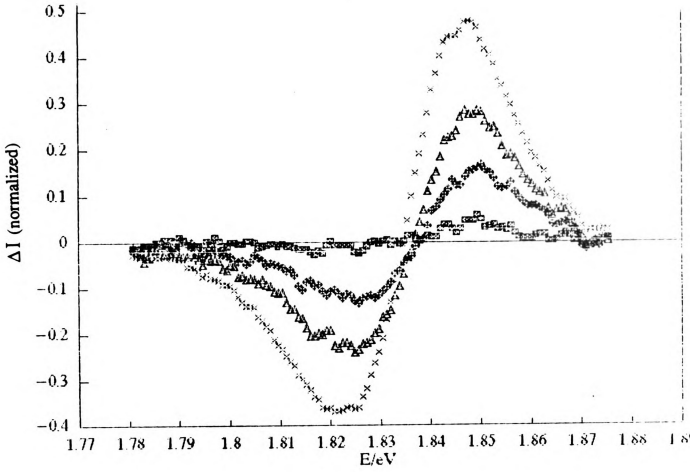

Fig. 3.8. Static fluorescence difference spectra for $Na^{+}C222Na^{-}$ at various temperatures. Temperatures from top to bottom on the right are 39, 30, 22.4 and 14.5 K. See the text for details of the normalization procedure.

(a). Normalize each spectrum in figure 3.3 to obtain the normalized spectra $s_p(T)$, in which T is the temperature.

(b). Subtract each $s_p(T)$ from $s_p(T=10\ K)$.

From the results shown in Fig. 3.8, we can see that:

(a). Each steady-state difference spectrum consists of two components, separated at E*=1.835 eV. It is positive, when E > E* and negative when E < E*.

(b). As temperature increases, the magnitude of both components in the difference spectra increases because of the way the difference spectra were constructed.

(c). The energy difference, $\Delta E \approx 25$ meV, between the peak positions of the two components, remains approximately invariant.

6. The fluorescence spectrum at 125 K.

The fluorescence spectrum of $Na^+C222Na^-$ measured at 125 K is shown in Fig. 3.9. From this figure, we see that the spectrum, which is structureless at lower temperatures, has two emission bands in the region of the G_V band in addition to a lower energy (RT) band. The major band has a peak energy at 1.822 eV and the weak band has a peak energy at 1.847 eV. These are the peak positions of the two components of the G_V band. The interpretation of the data described in this chapter will be discussed in chapter IV.

Reference

3.1. F. Urbach, Phys. Rev. 92, 1324 (1953).

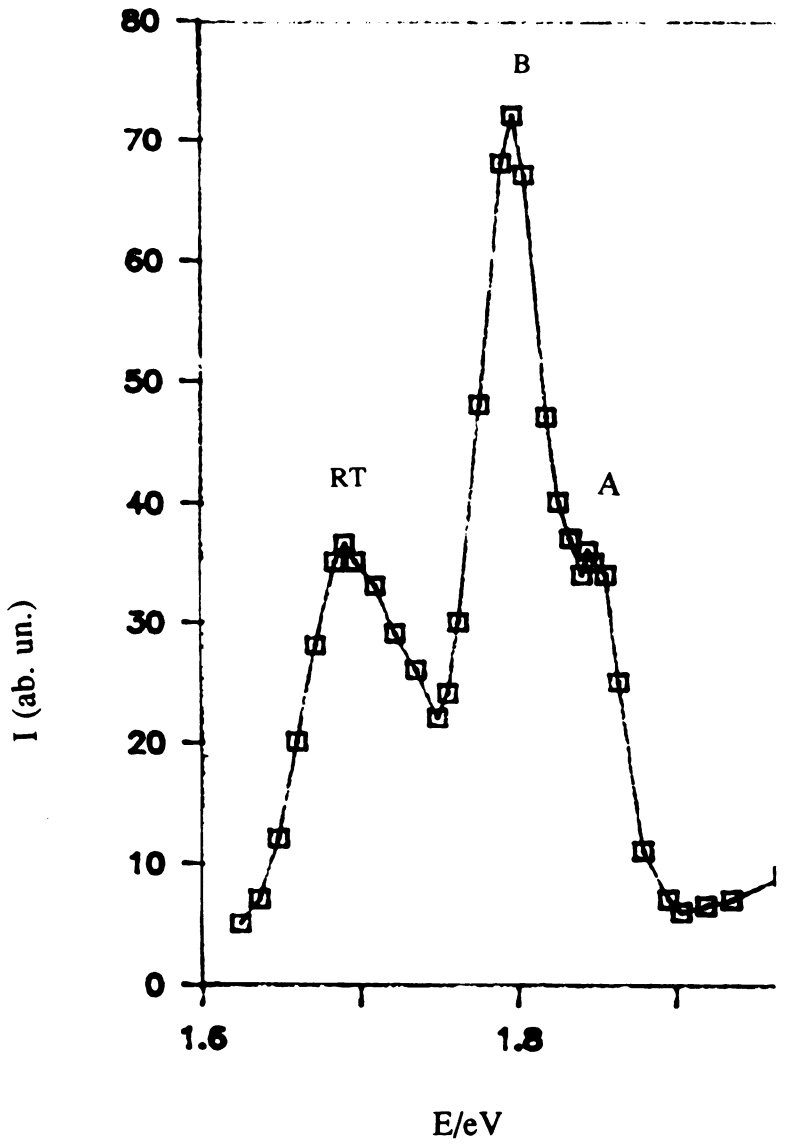

Fig. 3.9. Fluorescence spectrum of $Na^{+}C222Na^{-}$ at 125 K. The A peak appears as a shoulder on the right side of the major B band. The lower energy band with peak energy at ~1.70 eV is called the RT band (see Chapter IV for details).

Appendix-1 of chapter III

```
10      REM cutting of the data file header
15      DIM X(3000), XX(512),Y(512),YY(512)
16      for iii=1 to 100
20      INPUT "name of the source file ",FS$
30      OPEN FS$ FOR RANDOM AS #1 LEN=64
40      input "name of the image file  ",FT$
50      open FT$ for output AS #3
60         FIELD #1, 64 AS A$
70         FOR I=9 TO 40
80         GET #1, I
90         FOR J=1 TO 64
100     K=64*(1-1)+J
110        B$=MID$(A$,J,1)
120        X(K)=ASC(B$)
130        NEXT J :NEXT I
140        FOR I=1 TO 512
150        N=508+4*I
160        Y(I)=X(N+1)+256*(X(N+2)+256*X(N+3))
170     NEXT I
180        FOR I=1 TO 512
190        x1=1.0*I
191     KK=513-I
192     XX(I)=X1
193     YY(KK)=Y(I)
200     REM
210        NEXT I
211     FOR I=1 TO 512
212     PRINT #3,USING"########.#####";XX(I),YY(I)
213     NEXT I
220        CLOSE #1 : CLOSE #3
225     print xx(1),yy(1)
226     next iii
230        END
```

Appendix-2 of chapter III

```
20 REM Routine to restore binary data file from data cut collected with PCA
40 DEFINT A-Z
50 DEFSNG Y
60 DIM X(3000), YY(512)
70 CLS
90 INPUT "Data file name to be restored into binary";CDFN$
100 IF CDFN$="" THEN GOTO 320
110 NPTS = 0  '# of data points
120 RECLEN = 64 'Segment length of data file
130 BEGDATA = 9 'Segment to begin data
140 ENDDATA = 40 'Last segment of data
150 OPEN CDFN$ FOR INPUT AS #1
160 INPUT "Binary file(=target) name to carry data";ODFN$
170 OPEN ODFN$ FOR RANDOM AS #2 LEN=RECLEN
180 FIELD #2,RECLEN AS A$
190 INPUT "Binary file name created this time";CBFN$
200 OPEN CBFN$ FOR RANDOM AS #3 LEN=RECLEN
210 FIELD #3,RECLEN AS B$
220 REM RESTORE Initial segments to same as original file
230 FOR I = 1 TO (BEGDATA - 1)
240    GET #2,1
250    LSET B$ = A$
260    PUT #3,1
270 NEXT I
280 CLOSE #2
290 REM Build array of data points from corrected file
300 IF EOF(1) THEN GOTO 420
310    LINE INPUT #1,C$
320 IF VAL(C$)=0 THEN GOTO 290  'Ignore blank records
330    NPTS = NPTS + 1
340    I = 1
350    IF MID$(C$,I,1)<>" " THEN GOTO 380  'Find first #
360    I = I + 1
370    GOTO 350
380 REM End loop
390    J = INSTR(I,C$," ")     'Find end first #
400    YY(NPTS) = VAL(RIGHT$(C$,LEN(C$)-J))
410 GOTO 290
420 REM Data all in array, recreate binary data and write out file
430 PRINT "# data points read =";NPTS
440 J = 0
450 FOR I = NPTS TO 1 STEP -1
460               ' May want to multiply by a factor
470    L = INT(YY(I)+.5) 'Convert to integer
480    L1 = L MOD 256
490    LX = (L - L1) / 256
500    L2 = LX MOD 256
```

```
510     L3 = (LX - L2) / 256
520     J = J + 1
530     X(J) = L1
540     J = J + 1
550     X(J) = L2
560     J = J + 1
570     X(J) = L3
580     J = J + 1
590     X(J) = 0  'Last of four digits = 0 (Max = 64K)
600 IF I<13 THEN PRINT YY(I);L3;L2;L1
610 NEXT I
620 D$ = ""
630 K = 0
650 FOR I = 1 TO J
660     D$ = D$ + CHR$(X(I))
670     K = K + 1
680     IF K<>RECLEN THEN  GOTO 750
690        LSET B$ = D$
700        PUT #3,BEGDATA
710        BEGDATA = BEGDATA + 1
720        D$ = ""
730        K = 0
740 REM End IF
750 NEXT I
760 BEGDATA = BEGDATA - 1
770 PRINT "Last record written =";BEGDATA;"  should =";ENDDATA
780 CLOSE
790 INPUT "File name of Corrected data";CDFN$
800 IF CDFN$="" THEN GOTO 820
810 GOTO 110
820 END
```

CHAPTER IV

INTERPRETATION AND DISCUSSION OF RESULTS FROM CHAPTER III

In this chapter we summarize the results presented in the last chapter and then discuss them by using exciton models.

The major observations presented in chapter III fall into two categories:

(1). Energy transfer as indicated by conversion of the A-band to the B-band and the spectral split at 125 K.

(2). Application of the Urbach rule to the fluorescence line shape on the low energy side.

1. Model 1: Excitons.

The schematic diagram of model 1 is shown in Fig. 4.1. The system consists of two states, A and B. The energy of state A is 1.847 eV and the energy of state B is 1.822 eV. There is an interaction between A and B which causes an energy transfer between them. In the study described in chapter III, the excitation density is low enough to give complete reversibility of the spectra and the temperature is below 125 K. Under these circumstances, no back transfer is considered.

After excitation and relaxation to state A, the system is able to emit luminescence by the following paths.

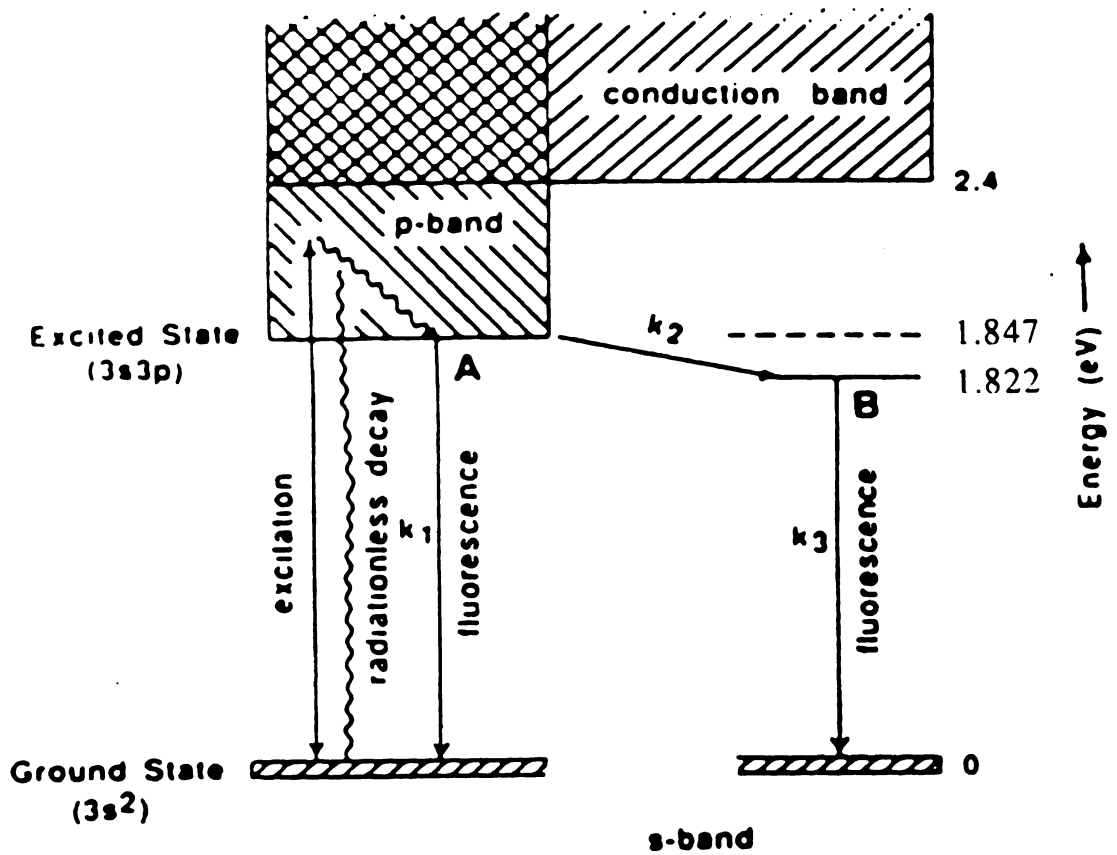

Fig. 4.1. Schematic representation of the decay scheme proposed for the fluorescence of $Na^+C222Na^-$ at low temperature. Taken from reference 1.13.

(1). Path 1. The system returns to its ground state directly from state A, accompanied by emission of photons.

(2). Path 2. State A transfers energy to state B. Then the system returns to the ground state accompanied by emission of either photons or phonons.

There are three pieces of experimental evidence that the G_V band is a superposition of the A and B bands.

The first evidence is provided by the six difference spectra shown in Fig. 3.7. They are obtained by subtracting each one from the same spectrum after normalization. The assumption made in the normalization is that the intrinsic fluorescence lifetimes are the same for states A and B. The delay times of the six spectra are: 1 ns, 2 ns, 4 ns, 6 ns, 8 ns, and 15 ns. The figure shows that the fluorescence spectrum loses intensity on the high energy side and gains intensity on the low energy side as a function of time. It is significant that the shift is not continuous but corresponds to intensity loss in one region and energy gain in another.

In general, a process in which a spectrum loses intensity in the high energy region faster than it does in the low energy region results in a red-shift of the fluorescence spectrum. A red-shift can be explained by other models than a two-band model. It may be interpreted, for example, as the result of energy loss by an exciton polariton, (EP, see Model 2 in this chapter for details). When an EP travels from the inside to the boundary of a crystal, the polariton loses energy, and a red-shift of the fluorescence spectrum occurs. A key fact in contradiction to this interpretation is that the energy

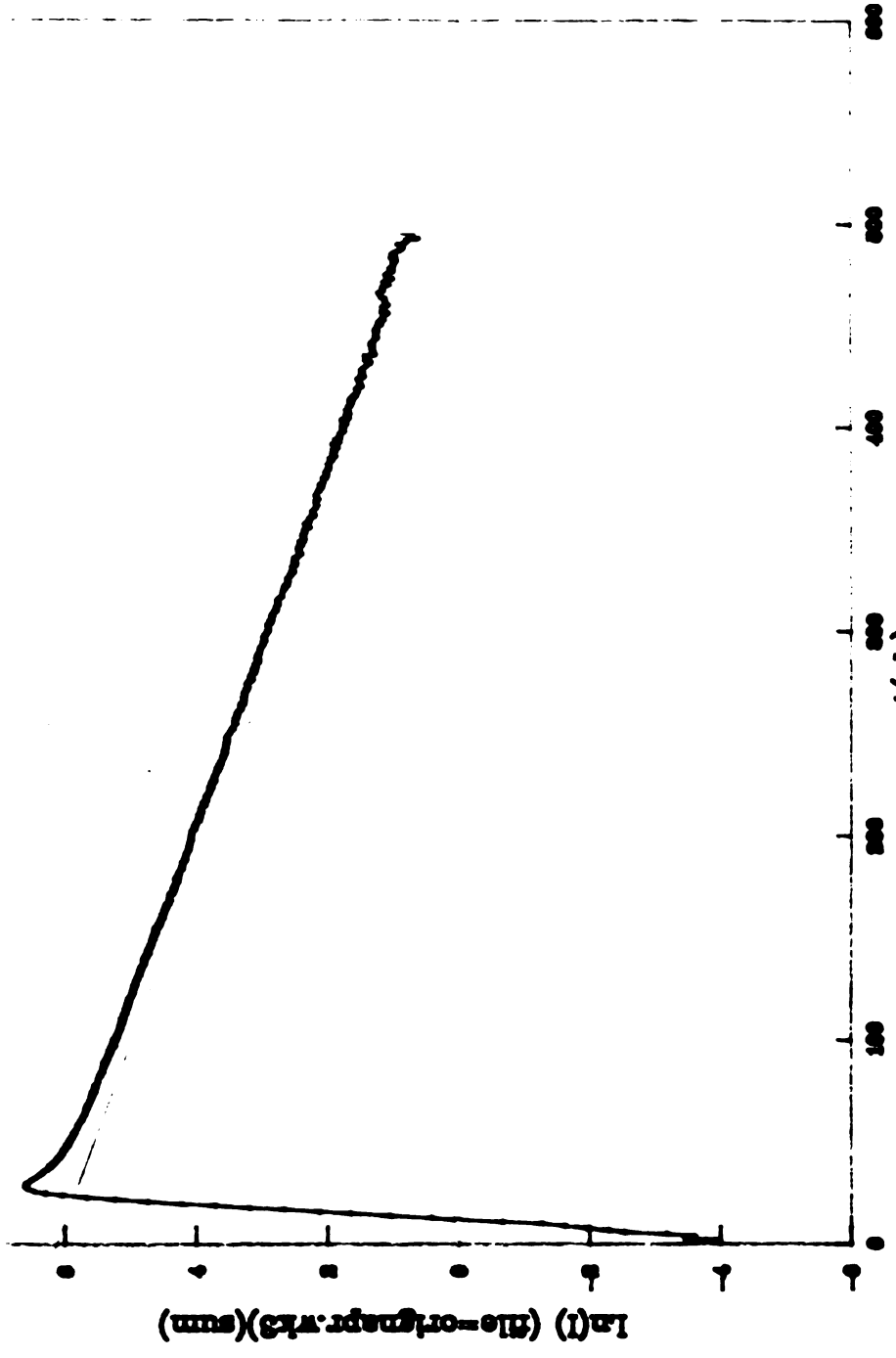

Fig. 4.2. Non-deconvoluted logarithmic decay curve of the spectrum-integrated fluorescence intensity of $Na^+C222Na^-$. The wide line was obtained experimentally at 20 K and the narrow straight line is a single exponential function with decay time constant τ = 5.048 ns. In the figure 1 ch=60 ps.

transfer occurs between two states, with their energies invariant as decay occurs. This is evident from Fig. 3.7. Specifically, we note that:

(a). The node shown in Fig. 3.7 is invariant with time. Each difference spectrum crosses zero at the same point. Such behavior is characteristics of the decay of one band and the growth of another due to energy transfer. The node corresponds to equal intensities of both spectra.

We emphasize here that the spectra are time-resolved. This means that each spectrum represents the emission at a specific time. The crossing points of all six difference spectra are at approximately the same position, E=1.83 eV. This observation is interpreted as follows: during the whole fluorescence process, in addition to energy loss by emission and radiationless decay, state A with energy $E > 1.83$ eV, transfers energy to state B at $E < 1.83$ eV.

(b). The line shapes of the two components on each side of the nodes are invariant with time. The figure shows that the six difference spectra have approximately the same shape. This strongly suggests that the fluorescence results from decay of the two distinct energy states.

According to the discussion above, we can draw the following conclusions:

(a). The G_V fluorescence band results from the superposition of two bands, whose relative intensities change with time.

(b). The two bands have peak energies at 1.847 eV and 1.822 eV.

(c). Energy transfers from the A-band to the B-band, but each band has a fixed energy position during the emission process.

The significance of the conclusion described above requires that the reliability of the time-resolved difference spectra be critically examined. Normally, in a time-resolved study that uses a (standard) single photon counting system, there is a difficult problem: that is, to deconvolute the IRF. As described in chapter I, a "real" fluorescence signal can be obtained only after deconvolution of the instrument response function. The procedures used for deconvolution have been the subject of intensive study for decades and much commercial software is now available. But one still faces the problem of spectral distortion, especially at early times, because of incomplete or incorrect deconvolution. For example, if there is a spectrum that decays faster on the high energy side than on the low energy side, the spectrum obtained by deconvolution that does not start at time zero will be distorted, because it omits more signal on the high energy side than on the low energy side. By using our difference procedure, however, this problem is avoided because it is not necessary to deconvolute the IRF. This is allowed because the IRF is energy independent.[4.1]

The spectrum at 125 K shown in Fig 3.9 provides a second piece of evidence that there are two discrete energy bands. These two bands have essentially fixed mean energy positions which are at 1.847 eV and 1.822 eV. This figure shows that at 125 K there are two peaks with energies at the positions given above; thus, the presence of the two bands is confirmed. The reason that this

spectral split is evident only at relatively high temperatures rather than at all temperatures will be discussed later.

The third result that demonstrates the presence of two bands is shown by the temperature dependence of the difference spectra in Fig. 3.8. On the high energy side, all the spectra lose fluorescence intensity while the low energy side gains intensity as the temperature is increased. Once again, the key point is that the energy transfer occurs between two states, with fixed mean values of the energy. Referring again to Fig. 3.8, it can be seen that:

(a). The crossing point is independent of temperature and is at the same energy for all spectra. The position of the node corresponds to an energy value, at which each band has the same intrinsic normalized intensity, which is located at approximately 1.83 eV, so that at $E > 1.83$ eV, the spectrum loses its intensity and at $E < 1.83$ eV, the spectrum gains intensity. The temperature dependence of the composite peak shows this separation because the long-lived component, B, dominates the static spectrum at higher temperatures, for which the energy transfer is fast. Note that this only occurs because the energy transfer rate increases more rapidly with increasing temperature than does the fluorescence rate.

(b). The four spectra shown in the figure have approximately the same shape, which means that the peak positions of the two components remain at approximately the same position as the temperature changes.

On the basis of these results, the three conclusions previously made on the basis of time dependence of the spectra are reinforced

by the temperature dependence. Thus, the time dependence, the separation into two peaks at high temperature and the temperature dependence of the band shape all favor a two-band model with energy transfer. The mean energy difference between band A and band B is 25 meV.

The model of two bands with energy transfer can be put on a quantitative basis by using the time-resolved fluorescence results.

We use $P_n(t)$ to represent the probability that at time t the system has an exciton existing at site n. The evolution of $Pn(t)$ follows a set of coupled rate equations[4.2]:

$$(d/dt)P_n(t)$$
$$=-(K + X_n + \Sigma K_{nn'})P_n(t) + \Sigma K_{n'n}P_{n'}(t) \qquad n \neq n' \qquad (4.1)$$

In this equation 1/K is the decay constant of the exciton without energy transfer, X_n is the transfer rate to a particular low lying level, $\Sigma K_{nn'}$ denotes the transfer of energy from the exciton at site n to the site n'.

For a system with $n > 2$, there are no exact solutions for equation (4.1) without a knowledge of the boundary conditions. However, there are two quantities, I_{Total} and ΔI, that can be measured with our technique. I_{Total}, is the fluorescence intensity integrated over the whole spectrum, which is given by the following equation:

$$I_{Total}=I_o(t=0)\ \exp(-kt) \qquad (4.2)$$

In the equation above, I_{Total} is given by a very simple expression that can be easily understood as follows. Being integrated over the whole spectrum, I_{Total} is the emission from the total system. Now it is assumed there are energy transfers within the system, which will affect the decay rate from an individual site or an energy level. Therefore, time resolved spectra will show a spectral transfer. However since the system as a whole has no energy transfer to other states, I_{Total} will still decay exponentially.

The experimental value of I_{Total}, is shown as a wide line and the one calculated from equation (4.2) with τ=5.048+/-0.05 ns, is the narrow line, as shown in Fig. 4.2. The single exponential decay describes the experimental behavior very well. Note that there is a small segment, with a time period of approximately 0.5 ns, during which the experimental values deviate dramatically from the single exponential function. This deviation is due to the fact that the decay curve was not deconvoluted. The IRF has a "lifetime" of 0.223 ns, (See Fig. 9.3 for the IRF) which results in this additional decay with a decay time constant of 0.2 ns. This explanation is reasonable because the process lasts for approximately 0.5 ns, the duration of the IRF.

For our two-state model, the fluorescence intensity at any energy and time is given by [1.13]

$$I(E,t)=I_A(E,t) + I_B(E,t) \qquad (4.3)$$

$$I(E,t)=a(E)P_A(t) + b(E)P_B(t) \qquad (4.4)$$

where a(E) and b(E) are characteristic shape functions of the A band and B band. The probabilities, $P_A(t)$ and $P_B(t)$, that fluorescence is emitted from the two states are assumed to be proportional to the concentrations of the emitting excitons, and can be derived from the proposed mechanism. Equation (4.1) is now simplified to a pair of equations, Equations 4.5 and 4.6 below:

$$d(P_A(t))/dt=-(k_T+k_A)*P_A(t) \qquad (4.5)$$

$$d(P_B(t))/dt= k_T P_A(t)-k_B P_B(t) \qquad (4.6)$$

which can be solved to give:

$$I_A(E,t) =a(E)P_A(0)* \exp[-(k_T+k_A)t] \qquad (4.7)$$

and

$$I_B(E,t) =P_A(0)\ b(E)k'\ \exp[-(k_A)t]*[1-\exp(-k_T t))] \qquad (4.8)$$

where k_T is the rate of energy transfer from the high energy to the low energy band and $k'=k_A/(k_A+k_T-k_B)$. Now we assume that $k_B=k_A=k=1/\tau$, and that the initial conditions are $P_A(0)=1$, $P_B(0) = 0$. We have:

$$I_A(E,t) = I_A(E,0) * \exp(-(k_T+k_A)t) \qquad (4.9)$$

We define the difference spectrum:

$$\Delta I = I(E,t)*\exp(t/\tau) - I_B(t')*\exp(t'/\tau) \qquad (4.10)$$

We have:

$$\Delta I = [a(E)\ P_A(0) - P_A(0)\ b(E)k'] *[\exp(-k_T t)-\exp(-k_T t')] \qquad (4.11)$$

If we choose time origin so that $t' = 0$, the equation above has the form:

$$\Delta I = A\ \exp(-k_T t) + B$$

where A and B do not depend on time. We define a function F as:

$$F=(\Delta I-B)/A$$

Which is:

$$F = \exp(-k_T t) \qquad (4.12)$$

Equation (4.12) can be checked with a time-resolved study.

A comparison of the calculated time course, in which $1/k_T$ = 1.755 ns with the values obtained experimentally is shown in Fig. 4.3. From the figure we see that the calculated and the experimental values fit well.

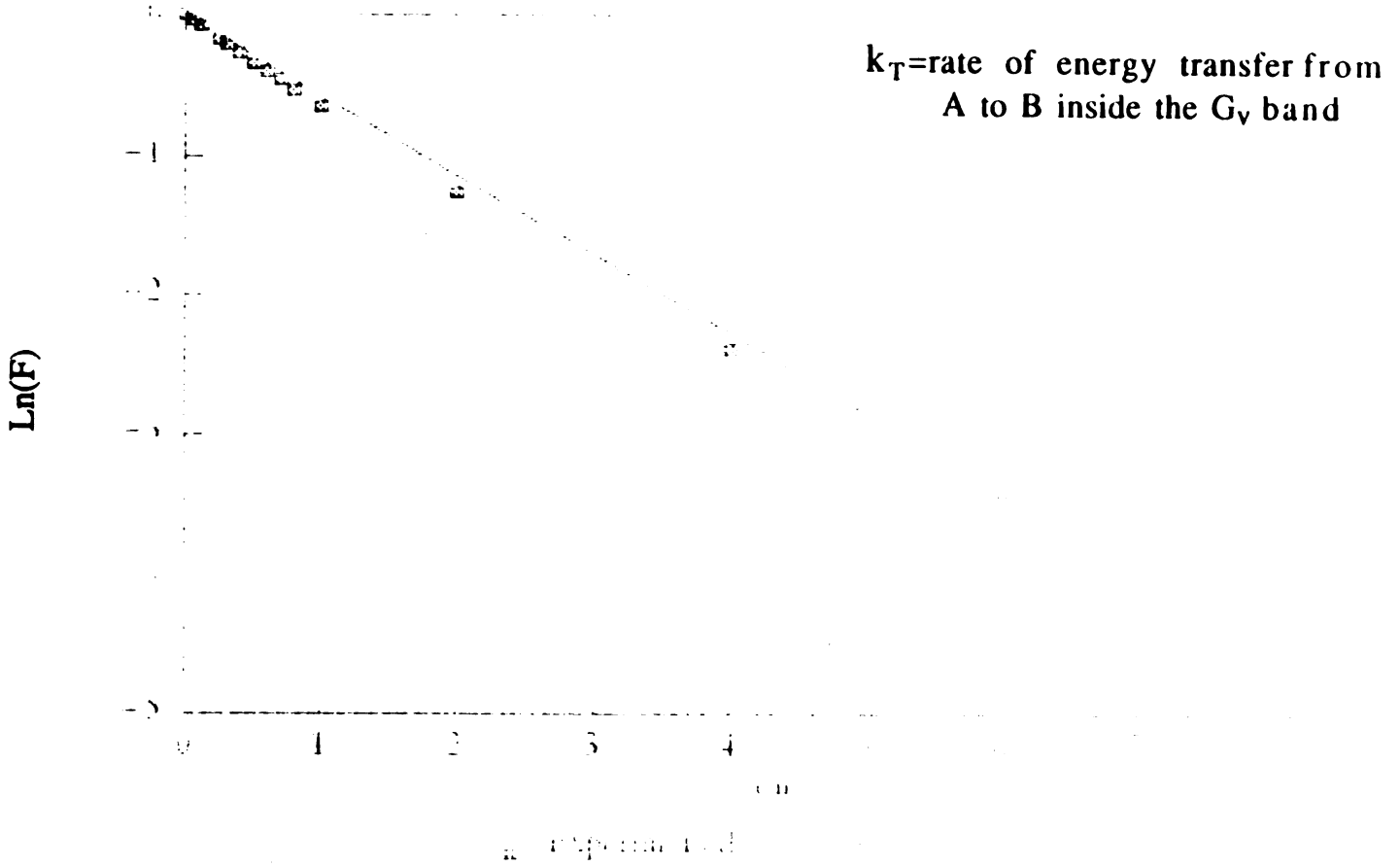

Fig. 4.3. Time course of function $F=\exp(-t\ k_T)$ for $Na^+C222Na^-$. The straight line is a Ln-plot of values calculated by Equation (4.12) with $(1/k_T)=1.755$ ns, while the squares are obtained experimentally at 20 K.

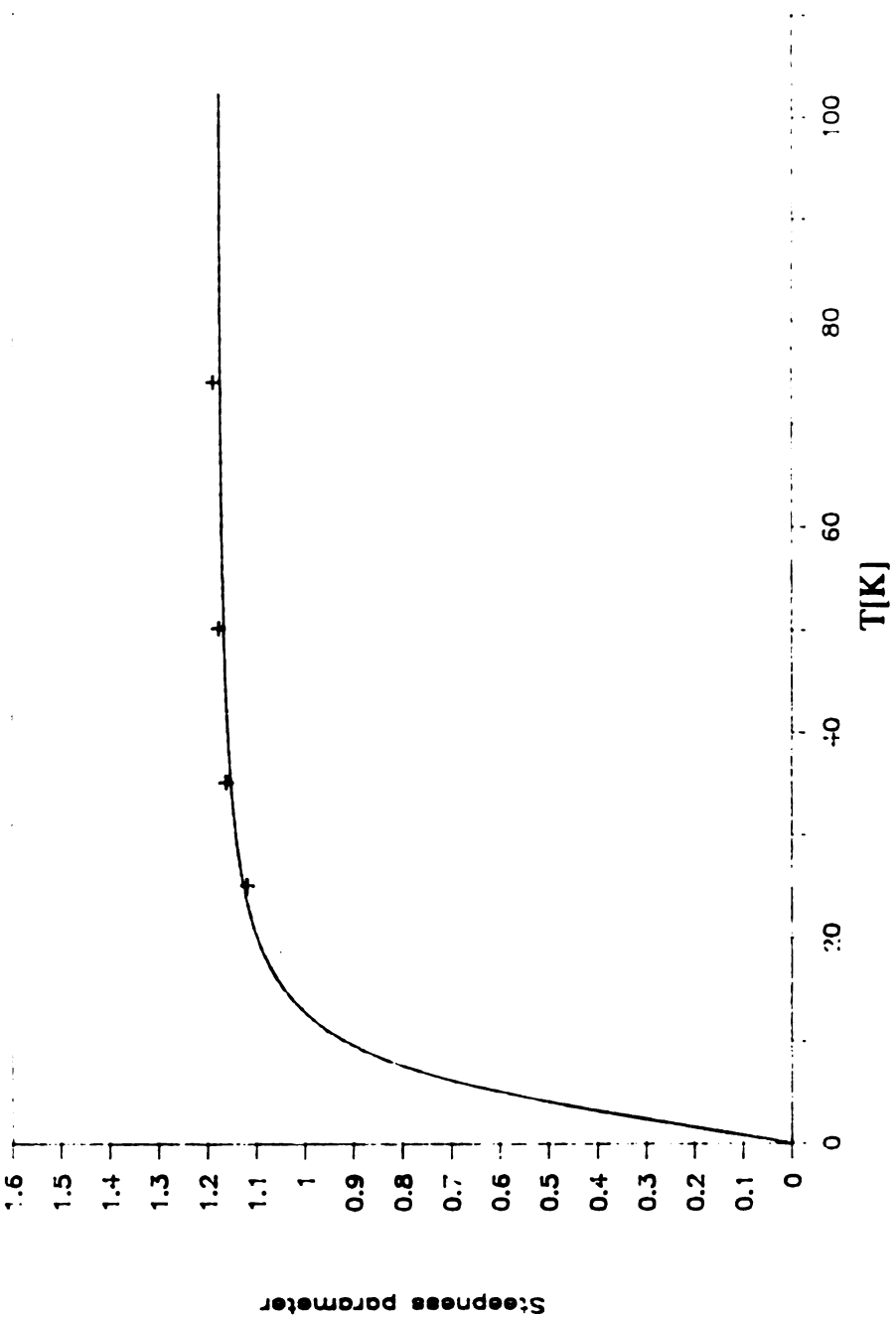

Fig. 4.4. Dependence of the steepness parameter σ on temperature for $Na^+C222Na^-$. The The crosses are experimental values while the solid curve is calculated by Equation (4.14) with σ_o=1.18 and $\nu = 4 \times 10^{11}$ Hz.

The difference spectra also show that the loss from band A is larger than the gain of band B, as indicated in Fig. 3.8. A possible reason is the existence of additional energy transfer processes from band A to some other acceptors. This question will be discussed in a later chapter where the appearance of additional low energy bands is considered.

There is another experimental fact which makes the energy transfer model favorable. The whole emission spectrum is within the absorption spectrum, (see Fig. 3.1). According to Forster, [4.3] the energy transfer rate is directly proportional to the overlap between the emission and the absorption spectra. Today, Forster's theory is commonly accepted and has been further developed.[4.4]

Explanation of the Urbach rule behavior.

The Urbach rule (U-rule) was first reported by Urbach in 1953.[3.1] The rule says that, for silver halides, alkali halides, and many other crystals (both pure and impure), the absorption coefficient α on the low energy side of the absorption peak has an exponential shape. The U-rule has been found in many types of materials and is often considered as a universal law. Martienson [4.5] Mahr [4.6], Sumi and Toyozawa [4.7] and many others have investigated the rule. They also extended the rule to the low temperature region and to emission spectra.

For luminescence, the rule says that the intensity on the low energy side of an emission peak follows the relation:

$$I(T,E) \propto e^{(\sigma-1)\cdot E/\kappa_B T} \qquad (4.13)$$

where κ_B is the Boltzmann constant and σ is called the steepness parameter. At low temperatures, σ depends on T as follows:

$$\sigma(T) = \sigma_0 \cdot (2\kappa_B T/E_p) \cdot \tanh(E_p/2\kappa_B T) \qquad (4.14)$$

where σ_0 is a constant that depends on the materials, $E_p=h\nu_p$ is the energy of a phonon mode or modes that interact sufficiently strongly with the exciton that it momentarily self-traps.

There have been many hypotheses proposed to explain the U-rule. We briefly introduce three of them here.

The first one was given by Hopfield.[4.8] According to this theory, an exciton-polariton is ionized thermally at a rate which is determined by a Boltzmann distribution, so that it is exponential in the temperature. This requires that the exciton level be very close to the conduction band.

The second one is due to Sumi and Toyozawa[4.4] who consider the U-tail as the result of a momentarily fluctuating potential caused by the phonon field. The exciton is localized for a brief period of time by this potential. This model was intended to explain both the exponential tail and the temperature dependence.

The third explanation was is given by Dow and Redfield,[4.9] who noted that random impurities result in a random electric field gradient, which affects the electronic state of a solid in a random

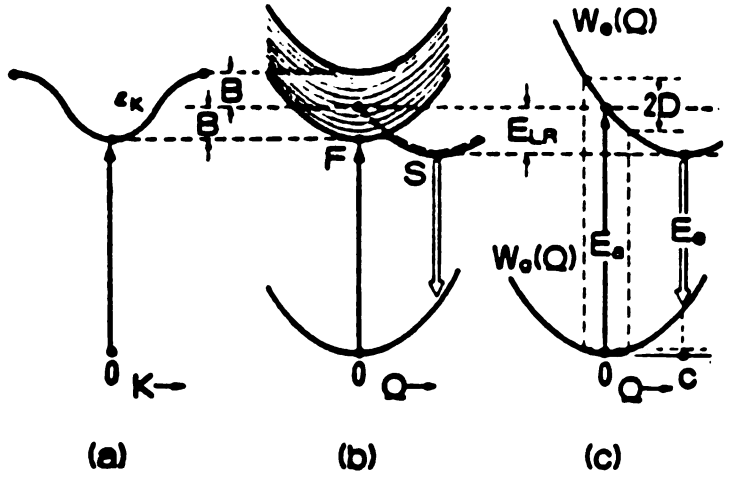

Fig. 4.5. Schematic representation and relationships among energy parameters affecting excitonic absorption and emission. (a) Dispersion of the exciton band in rigid lattice (without phonons); (b) and (c), Configuration Coordinate diagram for excitons in phonon field. Adapted from ref. 4.12.

way and results in an exponential edge for the absorption or emission, and a σ value that can be larger than unity. In a pure crystal, the interaction with phonons gives the same result as an electric field effect due to impurities. Mohler and Thomas [4.10] found that this hypothesis is consistent with their observations of the absorption edges of CuCl and TlCl in an applied field. But there are some workers, for example, Wiley and colleagues [4.11] who provided experimental evidence to reject this model.

Regardless of the correctness of the various hypotheses proposed, the phenomenological behavior of the Urbach rule is well-established. We now proceed to compare the predictions of the two state model with the observed U-rule behavior and with the spectral shape.

As reported in chapter III, we found that at low temperatures, the U-rule is obeyed by the fluorescence spectra of $Na^+C222Na^-$. Our experimental results are shown in Figs. 3.2 to 3.5, which indicate that both Equations 4.13 and 4.14 hold. From the data, we obtain $\sigma_0 = 1.18$ and $\nu_p = 4 \times 10^{11}$ Hz respectively. As shown in Fig. 3.5, there is a focus energy located at approximately 1.86 eV. (In fact, however, not every material that obeys Urbach's rule has a focus energy).

We propose that the ν_p value of the order of 10^{11} Hz, is the phonon frequency of a breathing mode of the lattice because we work in the low temperature region where this mode dominates. The values of σ, the steepness parameter, can be calculated by equations 4.13 and 4.14. As shown in Fig. 4.4. the σ value increases

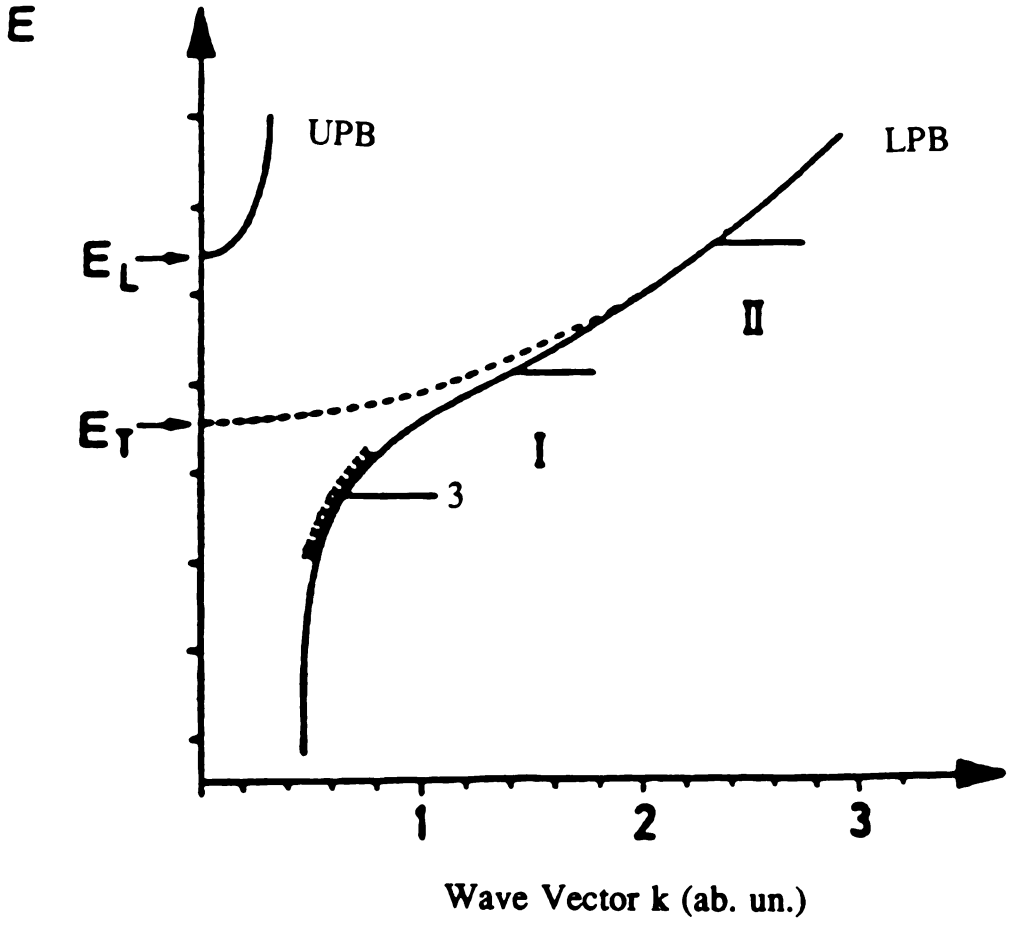

Fig. 4.6. Polariton dispersion relation. The bottleneck, which leads to the peak of fluorescence is in the cross-hatched region.

from 1.14 to 1.19 as temperature increases from 25 K to 80 K. In the figure, the crosses are experimental values and the solid curve is calculated from Equation 4.14.

The Urbach rule behavior of the fluorescence spectra of $Na^+C222Na^-$ is discussed as follows:

(a). The line shape of the fluorescence spectrum on the low energy side has an exponential dependence on the energy. The coordinate configuration diagram is shown in Fig. 4.5. In the figure band A, indicated by F is a free exciton band, while band B, represented by S in the figure, is produced by the interaction of the exciton with the phonon field. This B band is called a self-trapped exciton band. For our case it is assumed the minimum of the F band is 25 meV higher than that the S band. By this model the Urbach's tail arises from the low energy band.

We can see from the Fig. 4.5 that, there is an activation energy barrier between state A and state B. Therefore as T increases, the B state has a greater probability to be populated. At a high enough temperature we can see the split into two bands.

According to this model if the exciton is free, the line shape of the main spectrum is expected to be Lorentzian rather than the Gaussian shape that we observe. Therefore by this model we must assume the emission is mainly due to a Frenkel exciton which is strongly coupled with the phonon field. This gives an emission with a Gaussian shape[4.12], while the Urbach tail is due to a strong interaction with the phonon field.

2. Model 2: Exciton polariton.

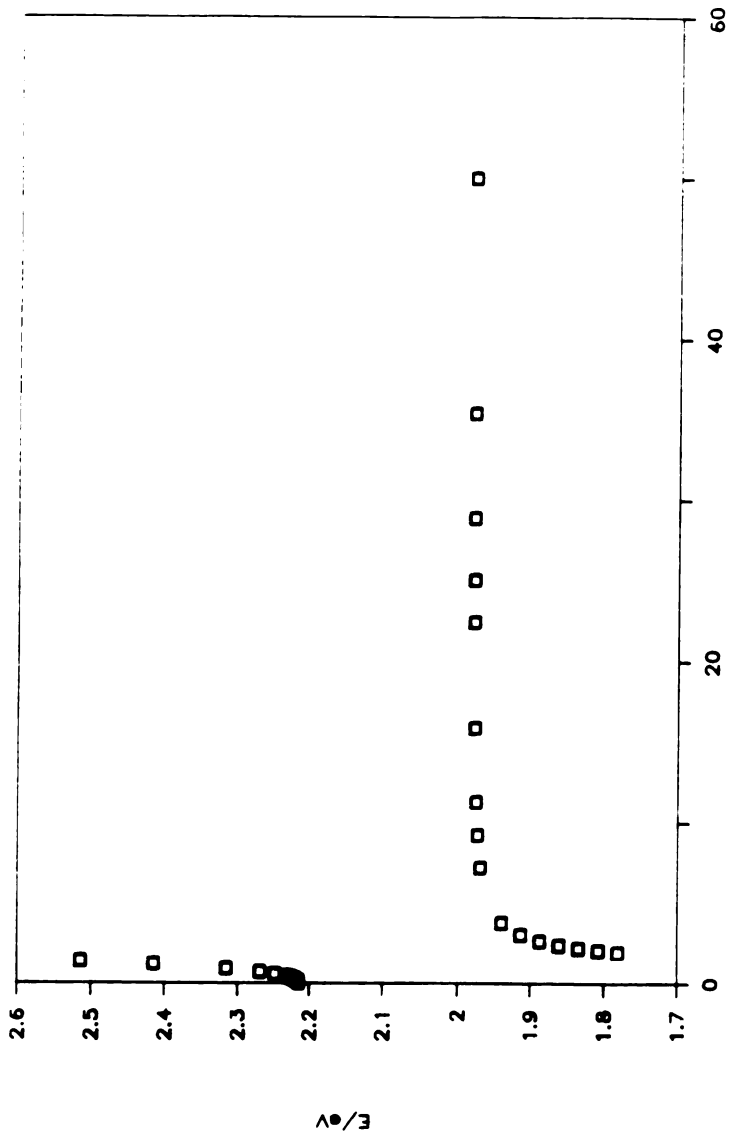

Fig. 4.7. Calculated polariton dispersion relation for $Na^{+}C222Na^{-}$ according to model 2. For the calculation the following parameters were used: effective mass of the exciton M = 0.01 m_e, where m_e is the electron mass at rest; ω_{LT} = 0.1 eV ; ε_∞ = 2.4 ; sound velocity in crystal c = 10^5 m/s; density of the material d = 1 g/cm^3; impurity density = 10^8(cm)$^{-3}$; temperature is 20 K.

The coupling of a polarized EM wave in a crystal lattice (photons) with excitons can form a new excitation mode, called an exciton polariton (EP). By using the concept of EP, it is possible to interpret the propagation of light in a crystal through the mixed mode of an electromagnetic field and crystal excitation. The EP theory was created by Kun Huang[4.13] about 40 years ago and developed by Hopfield[4.14] Paker[4.15] and many others. Detailed descriptions of EP can be found elsewhere [4.16, 4.17] Only a brief introduction is given below:

Fig. 4.6 shows the dispersion relation of energy vs. wave vector, for an exciton and EP. In the crystal there are two branches of excitons, one is called longitudinal, L-EX, the other is called transverse, or T-EX. (We only consider the low energy excitons.) The energy difference between the L and T excitons is ω_{LT}, (we set $2\pi h = 1$). There are two T-exciton polaritons formed. The one with the higher energy is called the upper branch exciton polariton, or UBP, and the one with the lower energy is called the lower branch exciton polariton, or LBP. We are only interested in the LBP, because the the UBP does not affect the analysis of fluorescence. From the figure we see, that in the region where K is close to zero, the EP behaves as a photon. At the other extreme, when K is large, the EP behaves as an exciton. Between these two regions, there is a cross over region, called the "bottleneck" region. In this bottleneck region, the EP has the smallest group velocity and corresponds to the accumulation of exciton polaritons in crystal.

According to this model, the fluorescence process is described as:

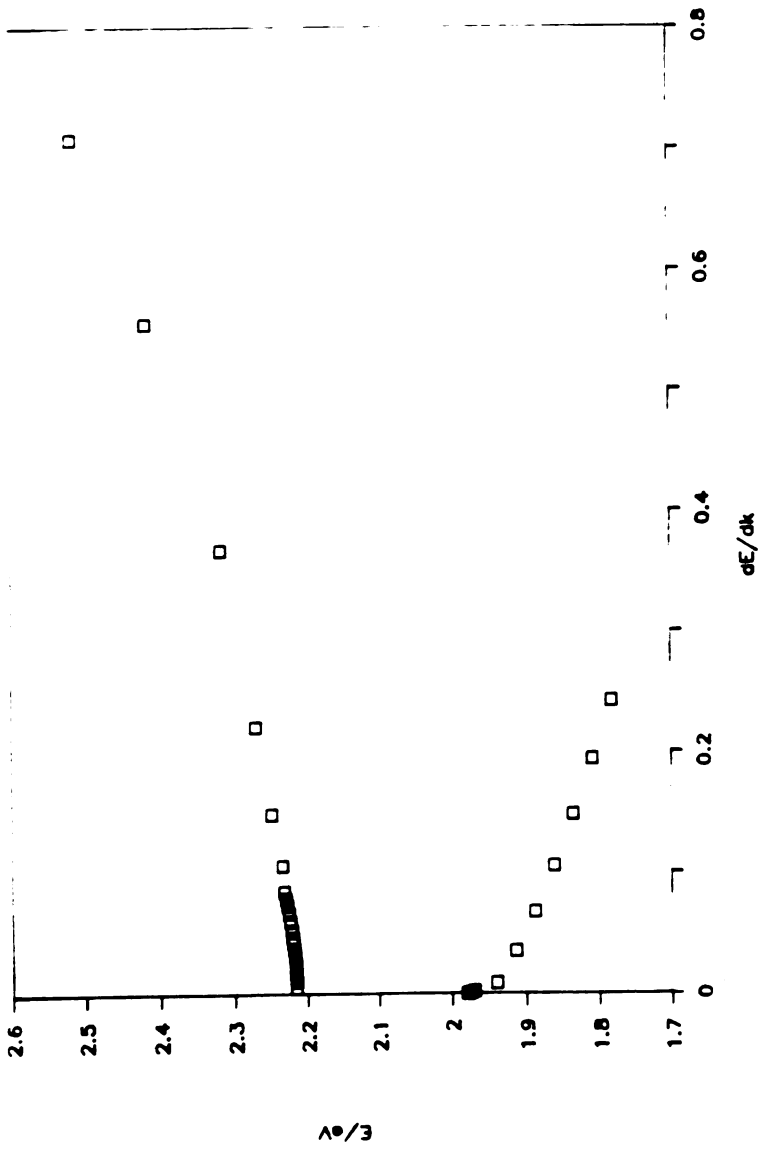

Fig. 4.8. Calculated polariton group velocity for $Na^{+}C222Na^{-}$ according to model 2.

a). The excitation is relaxed and absorbed by an EP in the UPB by resonance.

b). The EP in the UPB is elastically scattered by acoustic phonons to region II.

c). In region II of the figure the EP can be annihilated radiationally, accompanied by photon emission with frequency ω_L, or by radiationless processes. In region II, the EP can also be scattered to region I by phonons.

d). The region at about 3, the bottleneck region, corresponds to the peak position of the emission spectrum and a lifetime maximum.

e). As the EP is scattered by phonons, excitation energy migration occurs. As it reaches the boundary of the crystals, it can be detected as luminescence.

A polariton of a different type can also be formed by the coupling between photons and phonons. The typical values for an exciton polariton are $\omega_T=6 \times 10^{14}\ s^{-1}$, $k=2 \times 10^{6}\ m^{-1}$. The typical values for a phonon polariton are $\omega_T=1.5 \times 10^{13}\ s^{-1}$, $k=5 \times 10^{4} m^{-1}$.

The calculated dispersion relation and group velocity for $Na^{+}C222Na^{-}$ are shown in Fig. 4.7 and Fig. 4.8, respectively. A brief introduction to this can be found in the appendix of this chapter. The parameters used in the calculation are as follows:

Effective mass of the exciton, $M=0.01\ m_e$, where m_e is the electron mass at rest: ω_{LT} = 0.1 eV ; ε_∞ =2.4 ; sound velocity in the crystal $c = 10^{5}$ m/s; density of the material d= 1 g/cm^3; impurity density = $10^{8}(cm)^{-3}$; temperature is 20 K. By proper choice of the distribution function and the density of excited states with this EP model, the following observations can be explained:

(a). the band shape at a single temperature,

(b). the red-shift of the fluorescence peak position with time,

(c). the migration of excitation energy on the sample surface.

For details, the reader is refered to ref. 4.1.

The weaknesses of the EP model as a complete explanation of the observed phenomena are as follows:

(a). Failure to explain the Urbach rule behavior. According to the concept of EP, the fluorescence intensity relates to the temperature by Boltzmann formula:

$$I(T,E) \propto e^{-(E-E_i)/\kappa_B T}$$

Where E_i is the ionization energy of the EP. As a result, for any material, the steepness parameter of the spectra on the low energy side, which corresponds to the ionization of the EP, should be unity. However, the experimental values of σ for all material vary from 1 to 2.5.[4.12]

(b). The EP model fails to explain the sample-dependence of fluorescence spectra. According to the EP model an increased doping level of impurities should shift the spectrum to the blue.[4.1] However, we observed that at low temperatures, impurity level differences of up to 2 orders of magnitude do not affect the fluorescence line shape.

(c). The EP model also fails to explain the mismatch energy, 25 meV, observed by time-resolved and cw spectra. According to the EP model, when the EP is moving along the dispersion curve, its energy will continuously decrease. Therefore the observed energy

transfer, which results in the appearance of a node and two peaks at higher temperatures, as shown in Fig. 3.7 and 3.8, is not in accord with the EP model, which predicts that the fluorescence energy changes continuously with time.

References

4.1. T. Park, Ph. D. Dissertation, Michigan State University, (1991).

4.2. Huber, D. L., Dynamics of incoherent transfer, In "Laser Spectroscopy of Solids", Springer-Verlag, Berlin, Heidelberg New York (1981).

4.3. T. Forster, Ann. Phys. (Paris) 2, 55 1948

4.4. D. L. Dexter,J. Chem. Phys. 21, 836 (1953), T. Holstein et al, 1981, D. L. Huber, 1981)

4.5. W. Martienssen, J. Phys. Chem. Solids 2, 257 (1957).

4.6. H. Mahr, Phys. Rev. 125, 1510 (1962).

4.7. H. Sumi and Y. Toyozawa, J. Phys. Soc. Japan., 31, 342 (1971).

4.8. J.J. Hopfield, J. Phys. Chem. Solids, 22, 63 (1961).

4.9. J. D. Dow and D. Redfield Phys. Rev. B5, 594 (1972).

4.10. E. Mohler and B. Thomas, Phys. Rev. Lett. 44, 543, 1980.

4.11. J. D. Wiley, E. Schonheer, and A. Breitschwerdt, Solid State Comm. 34, 891 (1980); J. D. Wiley, E. Schonheer, and A. Breitschwerdt, J. Phys. Chem. Solids 41, 801(1980).

4.12. Y. Toyozawa, Excitonic Processes in Solids, Eds. M. Ueta et al, Springer-Verlag, Berlin, Heidelberg New York (1985).

4.13. K. Huang, Proc. Roy. Soc. (London) A 208 352 (1951).

4.14. J. J. Hopfield, Phys. Rev. 112, 1555 (1958).

4.15. S. I. Paker, Sov. Phys. -J. E. T. P. 6, 785 (1958); 11 1286 (9160).

4.16. Polariton, Ed. E. Burstein and F.D. Martini, 1972.

4.17. J. Aaviksoo, J. Luminescence, 48 & 49 (1991) 57-66.

CHAPTER V

BLEACHING AND RECOVERY OF THE FLUORESCENCE FROM $Na^+C222Na^-$

In this chapter, the observations and discussion of bleaching and recovery of fluorescence from $Na^+C222Na^-$, which occur when the excitation densities are relatively high, are presented. The experiments described in this chapter, if not specified otherwise, were carried under the following conditions: The source of the excitation at a wavelength of 532 nm was the Nd:YAG laser, the temperature of samples, $Na^+C222Na^-$ crystals, was 20 K and emission was detected at energy E=1.84 eV. In fact, bleaching and recovery of this compound have also been found in absorption and photo-emission studies.[5.1, 5.2] However, we refer only to bleaching and recovery of the fluorescence of $Na^+C222Na^-$.

RESULTS

1. The dependence of I_{em} on I_{exc}.

A log-log plot of I_{em}, the intensity of fluorescence versus I_{exc}, the excitation intensity, is shown in Fig. 5.1. The samples were single crystals with high quality and the time taken to obtain I_{em} was about 0.1 s. From the figure we find:

(a). When $I_{exc} < 10$ mW/cm^2, I_{em} increases linearly with I_{exc} with a slope of 0.97+/- 0.05.

(b). When $I_{exc} > 10$ mW/cm^2, the slope decreases.

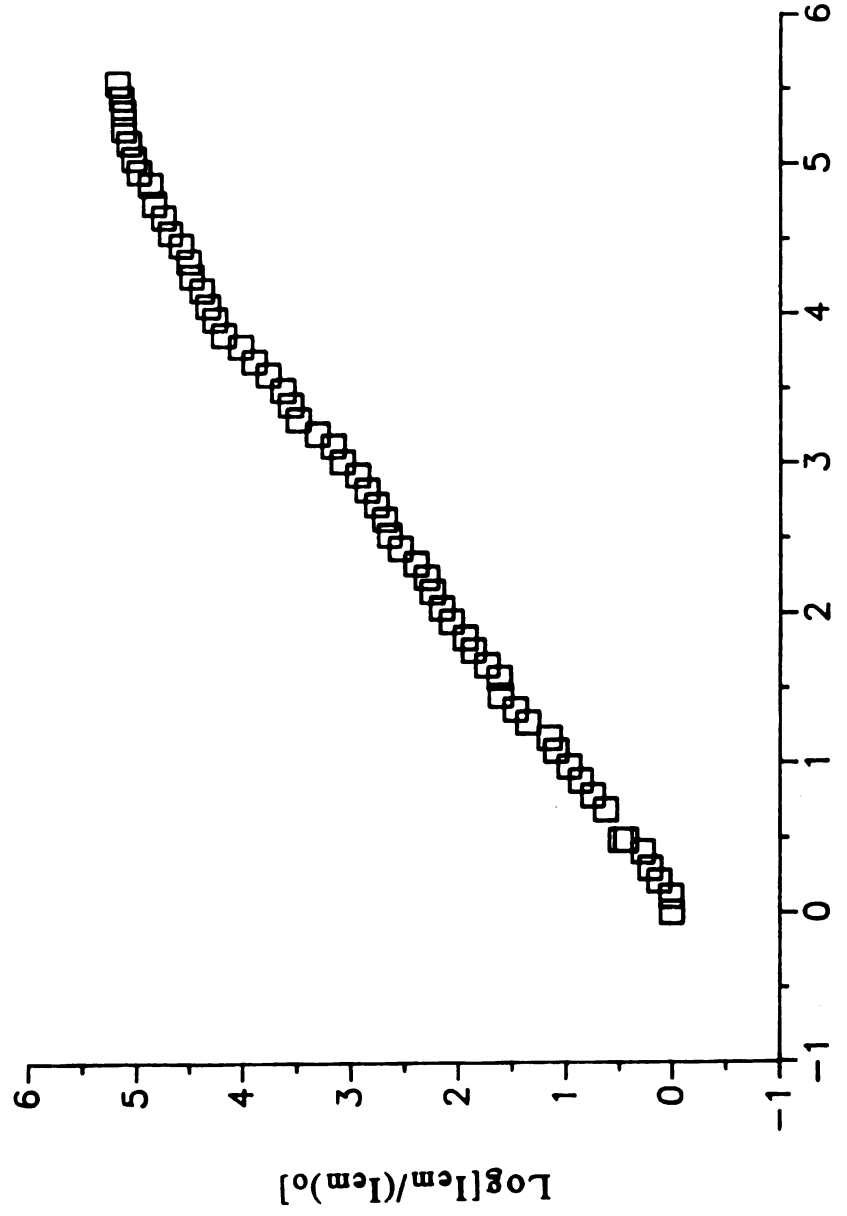

Fig. 5.1. Log-log plot of fluorescence intensity as a function of excitation intensity. In the figure $(I_{exc})_o = 6.3 \times 10^{-7}$ (W cm^{-2}) and $(I_{em})_o = 250$ counts.

(c). When $I_{exc} > 50$ mW/cm^2, the slope becomes smaller and becomes nearly zero when $I_{exc} = 1$ W/cm^2.

2. Fluorescence bleaching.

The dependence of I_{em}, the fluorescence intensity at 1.85 eV, on radiation duration, t_r, at various excitation intensities, I_{exc}, is shown in Fig. 5.2. The values of I_{exc} applied, from the top to the bottom, are: 10^{-7}W cm^{-2}, 0.001 mW cm^{-2}, 1 mW cm^{-2}, 50 mW cm^{-2} and 1W cm^{-2}. From the figure we can see that:

(a). When I_{exc} is very small, 10^{-7}W cm^{-2} for the top trace in the figure, I_{em} does not decrease with the duration time t_r.

(b). When I_{exc} is not very small, as shown by the other lower curves in the figure, I_{em} decreases with t_r.

(c). The higher the I_{exc}, the more rapidly I_{em} decreases and the longer the t_r, the more I_{em} loss occurs.

3. Fluorescence recovery.

After being bleached, the fluorescence can recover as seen in Fig. 5.3. In the figure, the horizontal axis represents time duration, while the vertical axis represents I_{em} on the same scale [except during the time before the end of t_{r2} for (a)]. The value of I_{exc}, the excitation density, for both (a) and (b) was 1.25 W/cm^2. The samples under study are assemblies of polycrystals that are nearly defect-free in (a) and defect-doped in (b). The EPR results for the two samples are shown in Fig. 5.4. In Fig. 5.3, t_{ri} represents the value of t_r at the i_{th} experiment, t_{ps} represents the time during

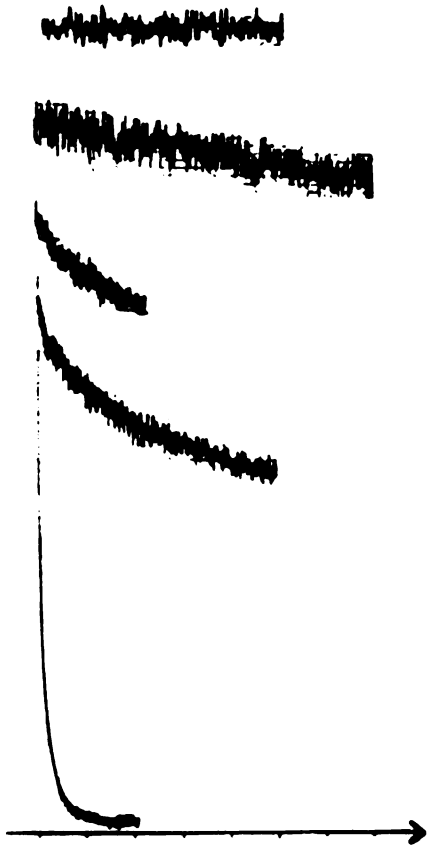

Fig. 5.2. Bleaching of the fluorescence intensity at 1.85 eV and 26 K. The excitation densities applied, from the top to the bottom, are: 10^{-7} W cm^{-2}, 0.001 mW cm^{-2}, 1 mW cm^{-2}, 50 mW cm^{-2} and 1W cm^{-2}.

which the radiation was turned off. The data in Fig. 5.3 correspond to the experiments carried out in the following way: the sample was excited for t_{r1} seconds by the YAG laser followed by no excitation for t_{ps} seconds and then the process was repeated. The fluorescence intensities, on the other hand, were being recorded continuously.

The recovery of the fluorescence for a "doped" sample is shown in (b) of Fig. 5.3. During t_{r1}, the first period of excitation, I_{d1}, the fluorescence intensity, declines (or is bleached). During t_{r2}, the second period of excitation, I_{d2}, the fluorescence intensity is bleached again. However, we notice that I_{d2} starts at an intensity higher than it was at the end of I_{d1}. This indicates that the fluorescence that bleached during t_{r1} had partially recovered. We can also see from Fig. 5.3 that the longer the elapsed time t_{ps}, the more pronounced the recovery is.

EPR spectra at 154 K of $Na^+C222Na^-$ from three different preparations are shown in Fig. 5.4. The sample with the highest EPR intensity is an assembly of defect-doped polycrystals, while the sample with the lowest EPR intensity is an assembly of nearly defect-free polycrystals. The other sample consists of crystals that were recrystalized from defect-doped polycrystals.

Fluorescence bleaching and recovery at different energies from a sample with the highest EPR intensity are shown in Fig. 5.5. The emission energies are, from the top to the bottom, 1.87 eV, 1.85 eV, 1.80 eV and 1.68 eV. The experiments were carried out at 36 K and at excitation density of 0.1 W cm^{-2}. The partial recovering that occurs upon standing is clearly evident at all emission energies. However, note that an initial bleaching occurs that is not reversible.

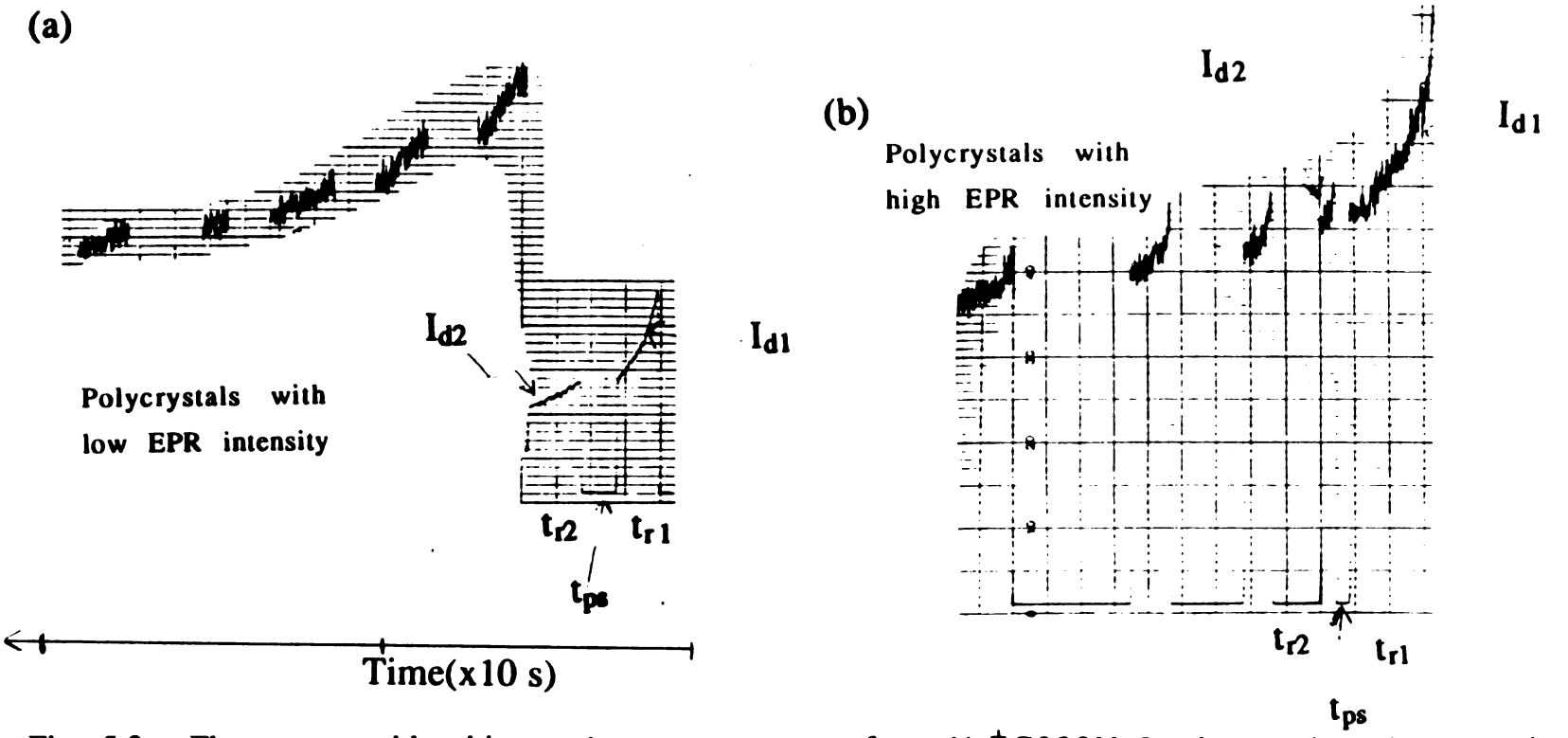

Fig. 5.3. Fluorescence bleaching and partial recovery from $Na^+C222Na^-$ polycrystals. The sample in (a) has low EPR intensity, while in (b) has high EPR intensity. The horizontal axis represents time. The vertical axis is the fluorescence intensity at 110 K and 1.824 eV. During the radiation times, t_{ri}, i=1,2, the fluorescence intensity decreases. After the non-radiation times, t_{ps}, in (b), however, the fluorescence starts at a level higher than at the end of the previous irradiation period, while that in (a) is unchanged. The excitation density was 1.25 W cm^{-2} and the scales of the fluorescence intensity are indicated.

DISCUSSION

Fig. 5.1 shows the dependence of the fluorescence intensity on excitation density. When the excitation density is low, the slope of the log of the fluorescence intensity against the log of the excitation intensity is 0.97 +/- 0.05. This relation extends over an excitation energy range of 4 orders of magnitudes. At high excitation densities, the response becomes non-linear. This is assumed to result from photobleaching of the sample. This bleaching is examined and discussed in detail below.

From Fig. 5.2 we see that the extent of the bleaching depends on both excitation density and t_r, the radiation duration. For the same radiation time t_r, the higher the excitation intensity, the more pronounced the bleaching. On the other hand if, I_{exc} is the same, the larger the t_r, the more pronounced is the observed bleaching.

From Fig. 5.3 we see that the recovery depends on the nature of the sample. Sample (a) of Fig 5.3 is undoped, and the fluorescence recovery is nearly absent. By contract, the fluorescence recovery from the defect-doped sample, (b) in the figure, is pronounced but not complete.

There is a correlation between the results of EPR experiments and fluorescence. The EPR results at 150 K for the defect-doped and undoped samples are shown in Fig. 5.4. In the figure, the sample having the highest EPR signal is refered to as "defect-doped" and the one with the lowest EPR signal is called "undoped". Therefore we see that the fluorescence from the sample with high EPR intensity is

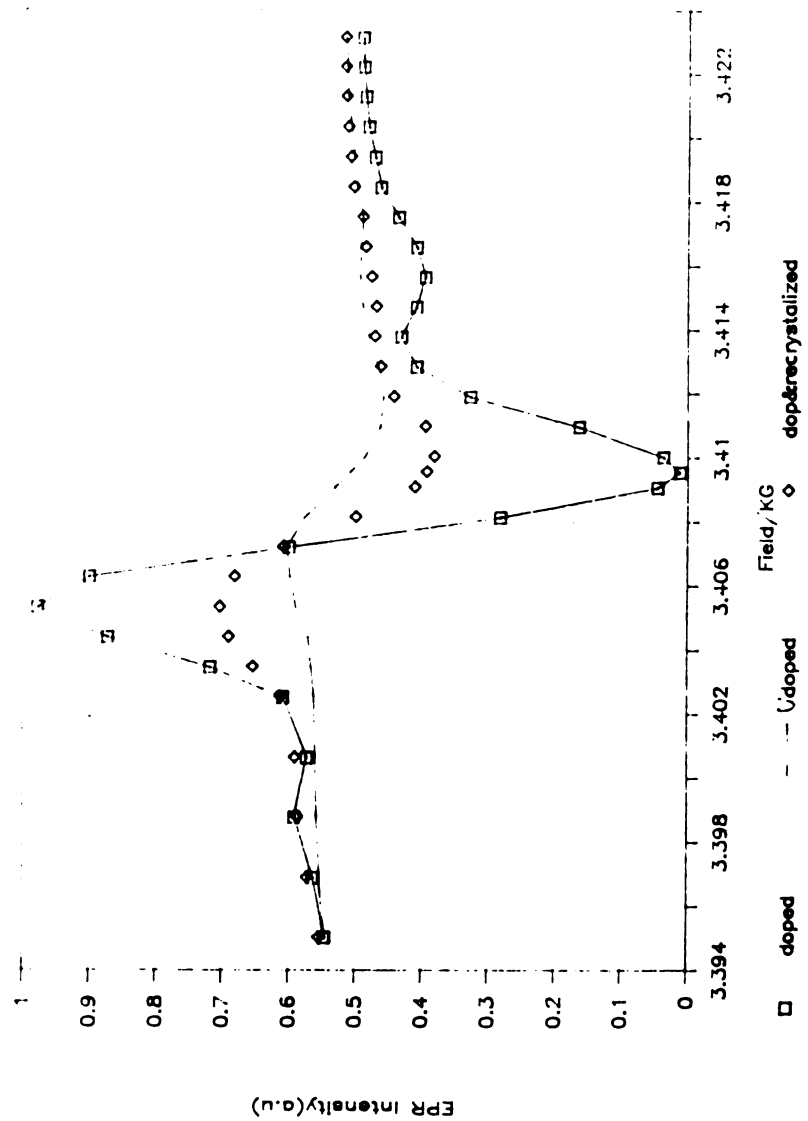

Fig. 5.4. EPR spectra at 154 K from of $Na^{+}C222Na^{-}$ for three different preparations. The sample with the highest EPR intensity is an assembly of defect-doped polycrystals; The sample with lowest EPR intensity is an assembly of nearly defect-free polycrystals; The other sample consists single crystals that were recrystalized from defect-doped polycrystals.

found to be more easily bleached and recovered than the sample with low EPR intensity.

According to one possible explanation, the bleaching and recovery process is considered due to the temperature rise at the point of illumination by the laser light. First let us see how temperature is detected with our apparatus:

(1). The crystals are at the bottom of a quartz tube. In the tube, there is a conducting gas, helium, filled at a pressure of approximately 10^{-3} torr.

(2). The tubing is held by a copper metal holder.

(3). A thermal sensor attached to the copper holder reports the temperature.

From the arrangement described above, we consider that:

(a). At zero or nearly zero excitation, the temperature detected by the sensor is the temperature of the sample.

(b). Under intense excitation, the temperature at the point where the absorption and emission takes place will be higher than that detected.[1.15]

As we have found, see chapter III for the detail, the fluorescence intensity is sensitive to temperature. Therefore, we assume that the continuous excitation result in a temperature rise by which the fluorescence intensity decreases. Then it is not bleaching. The major character of the decrease in fluorescence intensity is that when radiation duration, t_r, is close to zero, I_{em} depends on I_{exc} linearly. The larger the t_r, the more pronounced deviation of $I_{em}(t)$ from linearity.

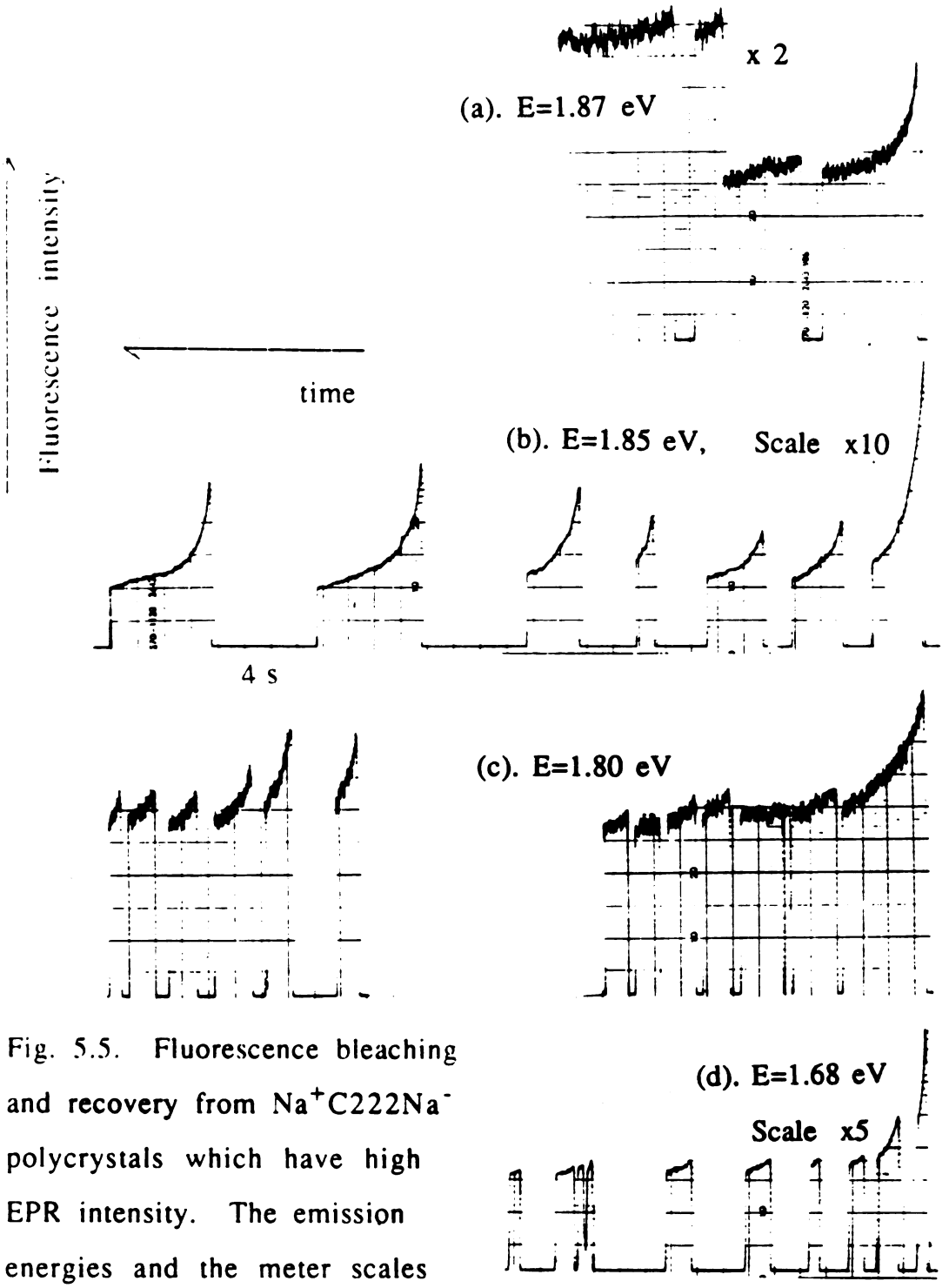

Fig. 5.5. Fluorescence bleaching and recovery from $Na^{+}C222Na^{-}$ polycrystals which have high EPR intensity. The emission energies and the meter scales of the fluorescence intensity measurements are indicated. The experiments were carried out at 36 K and excitation density of 0.1 W cm^{-2}.

The local temperature caused by continuous excitation by laser light is estimated as follows: It has been observed that the fluorescence intensity is related to temperature as shown in Fig. 3.4. To a first approximation, we consider I_{em} to decrease linearly with T with a rate of 2% per Kelvin. For the bleaching which is 100 % recoverable as shown by the second curve in Fig. 5.2, the bleaching rate is about 2 to 10 percent per second. In this case we consider the local temperature at the point under study is 1 to 5 Kelvin higher than that detected. For the decay of I_{d1} in Fig. 5.3 in which only a partial recovery was observed, the local temperature is estimated to be raised by the rate of 30 K/s for undoped sample and 35 K/s for doped sample. To obtain this estimate, the largest slope was obtained along the I_{d1} curve and extended up to one second. By a similar consideration, we assume when we stop the excitation, the heat will be removed and the local temperature T will be lowered as time elapses. As a result, we see the fluorescence recovery. A 100 % recovery occurs only when the excitation density is low. This fact was considered due to a slow minor temperature raise. The local temperature estimate for the most rapid bleaching process is shown by the line in Fig. 5.2 as follows. The fluorescence intensity bleached is 90 % which yields a 200 K/s raise in the sample. It is still not high enough to decompose the compound, which would make the bleaching process irreversible.

However, by this local temperature model, we cannot understand why recovery is not 100 % in most cases. Local temperature calculated by this model, as demonstrated above, is too low to cause decomposition or decomplexation of the sample. It is

possible that the 2% reduction of Iem on T which was obtained at T< 30 K is too small. Another problem for this model is that it is unable to explain why the phenomenon of recovery is much more remarkable for the sample with high EPR intensity than for the sample with low EPR intensity.

A second possible explanation has been proposed by J. L. Dye.[5.3] According to his model, the "bleaching" is the result of quenching of fluorescence by light-produced defect electrons that can be deposited in deep traps (irreversible) or shallow traps (reversible). The detailed nature of these traps has not been determined.

References

5.1. M. G. De Backer, F. X. Sauvage and J. L. Dye, Chem. Phys. Let. Vol. 173, No. 4, 291, 1990.

5.2. Bleaching and recovery of photo-emission for $Na^{+}C222Na^{-}$ observed by C. Kuo, W. Pratt and J. Dye.

5.3. J. L. Dye, Personal communication.

CHAPTER VI

LOW ENERGY FLUORESCENCE BANDS FROM CRYSTALLINE $Na^+C222Na^-$

According to the results in chapter III, fluorescence from crystalline $Na^+C222Na^-$ exhibits a single G_V band at 20 K under the condition of very weak excitation. The peak energy of this G_V band, which contains sub-bands A and B is 1.84 eV. In this chapter we examine three additional fluorescence bands, which are observed under experimental conditions that are different from those discussed previously.

Experimental Results

1. CW Spectra at room temperature.

Three CW fluorescence spectra obtained at room temperature are shown in Figs. 6.1 (a), (b) and (c). The samples in (a), (b) and (c) are single crystals, polycrystals (undoped), and solvent-evaporated films respectively. The figure shows that the fluorescence spectra in (a), (b) and (c) are all single bands. The peak positions are at 1.68, 1.69 and 1.70 eV respectively. The shapes of all three emission spectra are similar and all have a FWHM of approximately 50 meV.

2. Spectra at 130 K

Fig. 6.2 (a), (b) and (c) show three fluorescence spectra obtained at 130 K from different samples. The samples used for the

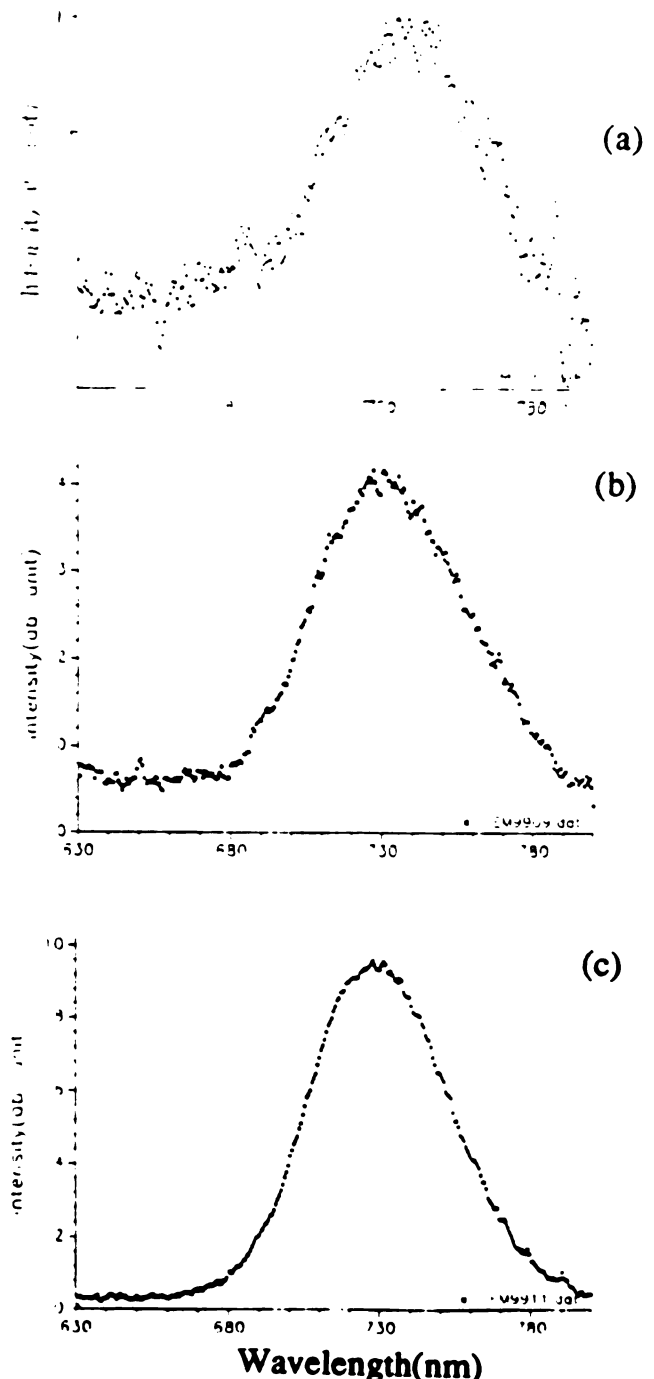

Fig. 6.1. Fluorescence spectra of $Na^{+}C222Na^{-}$ at room temperature. Samples studied are assemblies of: (a), single crystals of approximately 1mm x 1mm x 2mm; (b), polycrystals and (c), thin films. The excitation wavelength was 435 nm from a 150 W Xe lamp and a correction has been made for non-linearity of the PMT (R1104).

spectrum in (a) are doped polycrystals, for (b) are undoped polycrystals and for (c) are single crystals crystallized from the sample preparation used to produce spectrum (a). These samples are from the same preparations used to study the fluorescence bleaching phenomena described in Chapter V. Their EPR spectra are shown in Fig. 5.4.

3. Temperature dependence of the fluorescence intensity.

The temperature dependence of the fluorescence intensity at 1.7 eV (the RT band) was studied relative to that of G_V band. The intensity ratio R=I(E=1.7 eV)/I(E=1.84 eV) varies with temperature as shown in Fig. 6.3. Below 150 K R increases linearly with a rate of approximately 0.5 percent per Kelvin. Above 150 K R increases much more rapidly with a rate of approximately 7.5 percent per Kelvin.

4. Time-resolved fluorescence spectra from radiation damaged crystals.

Time-resolved spectra from a group of radiation damaged crystals (about 1 mm in diameter) are shown in Fig. 6.4. The crystals had been irradiated by a pulsed dye laser for 4 hours with an average power of 200 mW/cm^2 at 20 K. The delay times for the three spectra in Fig. 6.4, from the top to the bottom, are 0 ns, 1 ns and 2 ns. The control, the spectrum taken without irradiation by the laser, is shown in Fig. 3.2.

Discussion.

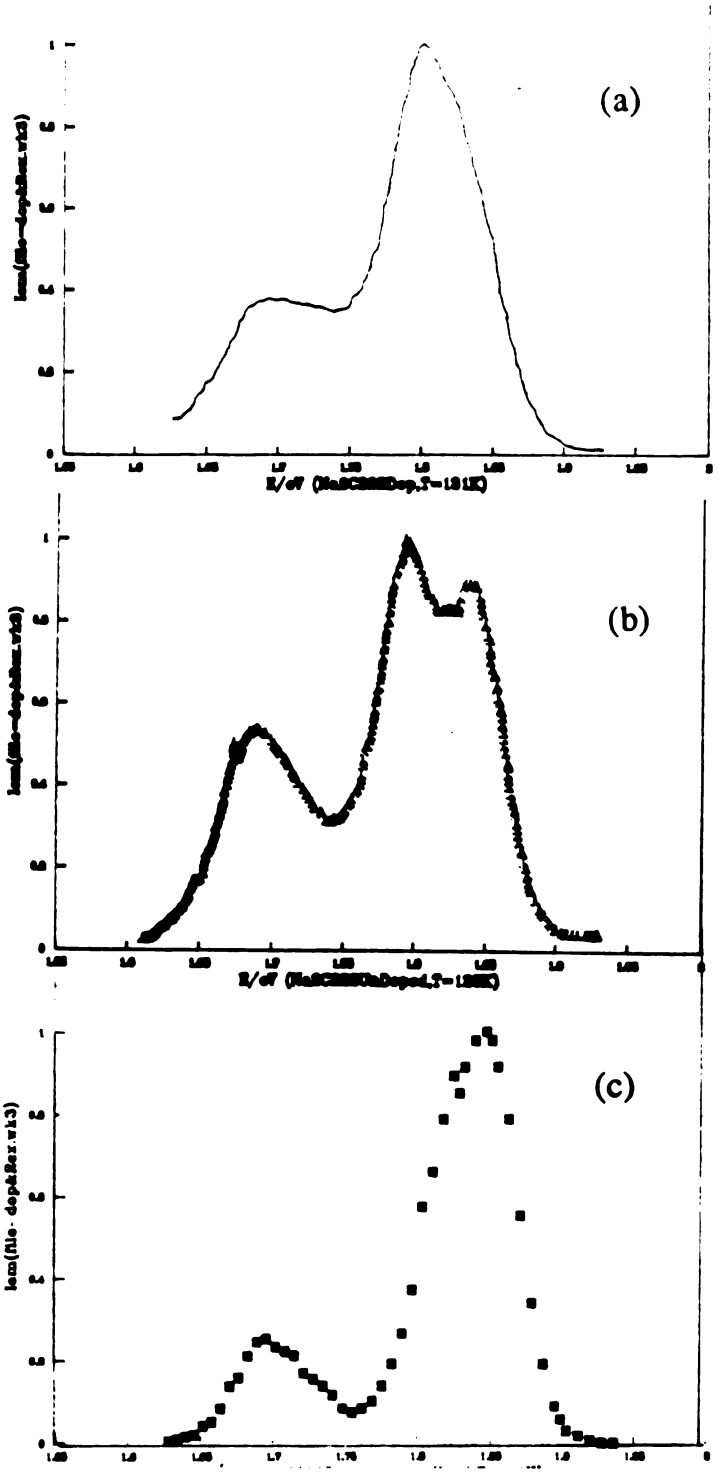

Fig. 6.2. Fluorescence spectra of $Na^{+}C222Na^{-}$ at 130 K from three different preparations. Samples are assemblies of: (a), polycrystals with high EPR intensity; (b), polycrystals with low EPR intensity; and (c) single crystals.

The spectra shown in Fig 6.1 indicate that only one emission band can be seen at room temperature. This band is structureless, with roughly the same shape and peak position for three different samples. Note that, although all three spectra refer to the same compound, they are from different samples: single crystals, polycrystals and micropolycrystals (films) respectively. Therefore this RT band appears to be an intrinsic emission band rather than the result of defects.

Any comparison of absolute fluorescence intensities of the spectra shown in Fig. 6.1 is difficult. For example, the reflectivities of the samples are different, so that the absorption differs from one sample to another. The effective penetration depth and the magnitude of light scattering are also different. However, for what it is worth, the emission intensities (at the peak positions) are, from top to bottom, 1, 4, and 10. This suggests that the RT emission intensity from single crystals is weaker than from polycrystals. A major difference between single crystals and polycrystals is that there are many grain boundaries in polycrystals. We anticipate that films will have the smallest crystals. Therefore, we tentatively assign the RT band to the emission related to grain boundaries. Of course, polycrystals and films might also have more defects by virtue of their method of preparation, so that the intensity effect could result from defects.

We can see from Fig. 6.2, that there are two bands in (a) and (c) and three bands in (b). Note that these are from three different samples: defect-doped polycrystals in (a), undoped polycrystals in (b), and an assembly of single crystals in (c). Consider the emission

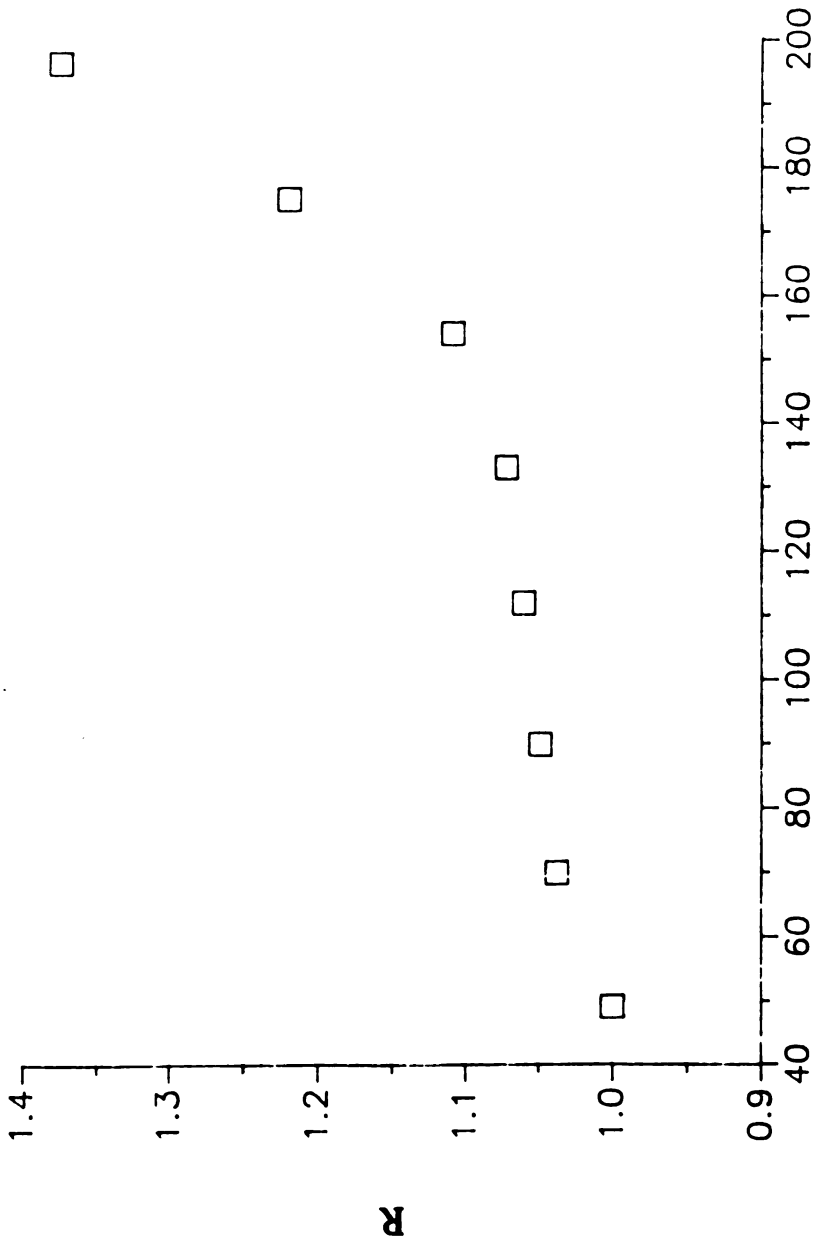

Fig. 6.3. Dependence of the ratio R on temperature, in which R=I(E=1.7 eV)/I(E=1.84 eV).

band with peak energy at 1.7 eV. We see that this band in (c) is well resolved, and in (b) partially resolved. This band is considered to be the RT band as shown in Fig. 6.1 and to have about the same peak position and shape at 130 K as at 300 K. The reasons for the assignment are as follows:

(a). As shown in (c) of Fig. 6.2, this band has the same peak position as that in Fig. 6.1.

(b). From (c) and (b) of Fig. 6.2, we see that the band has roughly the same shape as that shown in Fig. 6.1.

Besides the RT band, there is another band in (c) Fig. 6.2, which has an emission peak at 1.84 eV. We recognize this as the G_V band, because of its characteristics, including the band position and the shape on the high energy side. The band width of the G_V band is approximately 40 meV, which is only 13 meV wider than it is at 20 K.

In (b) of Fig. 6.2, the spectrum consists of three emission bands with peak positions of 1.7 eV, 1.8 eV and 1.84 eV. We assign the three bands as follows:

(a). The low energy band with a peak energy at 1.7 eV is believed to be the RT band.

(b). The high energy band with a peak position of 1.84 eV, is the G_V band.

(c). The middle band which has a peak position at 1.8 eV overlaps with the G_V band in spectrum (b). We will call this middle band the epr band hereafter, and assign it to doping-related emission. This assignment can be seen by correlating Fig 6.2 and the

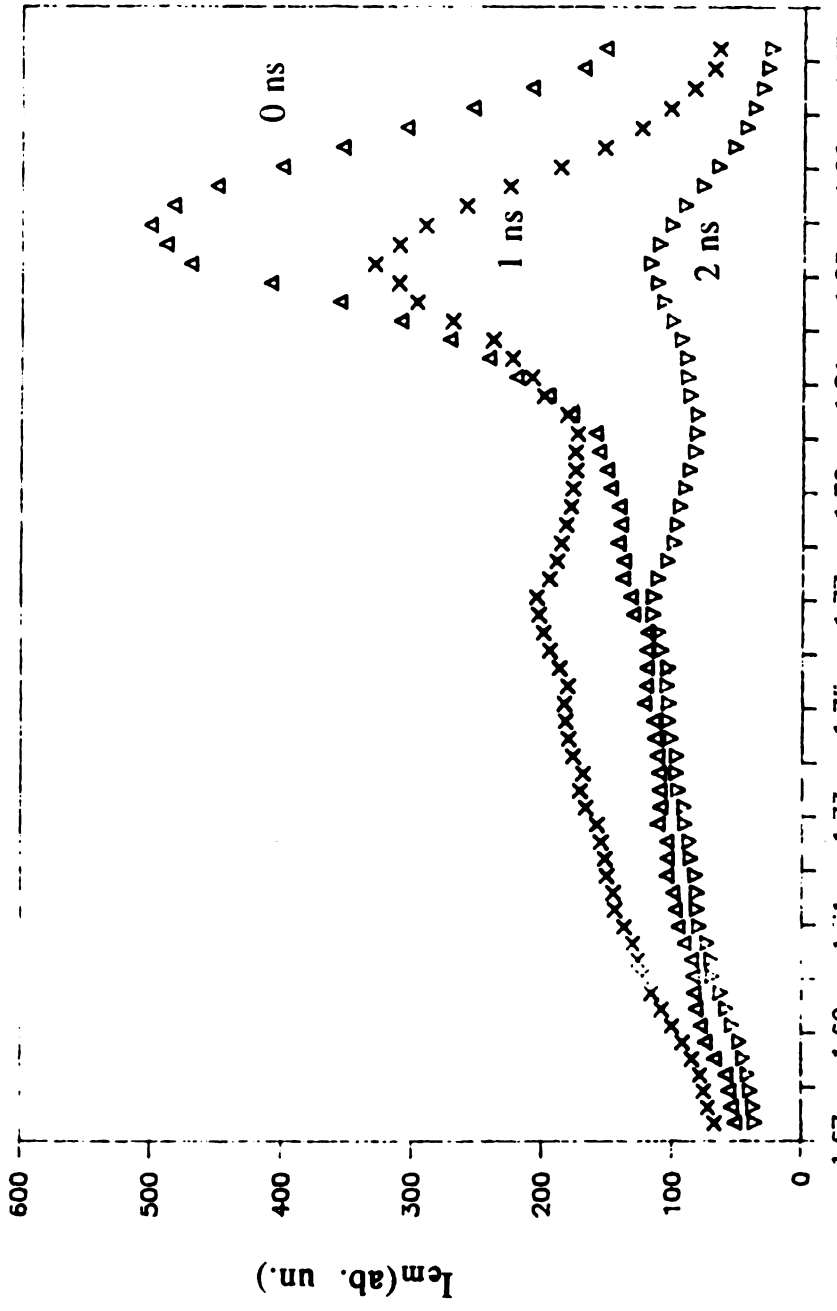

Fig. 6.4. Time-resolved fluorescence spectra at 20 K from a laser-irradiated sample of $Na^+C222Na^-$. Note the growth of the absolute intensity at low energies during the first nanosecond.

EPR result shown in Fig. 5.4. As indicated previously, the samples for the two studies were from the same preparations.

From spectrum (a) of Fig. 6.2, we see that there are two emission bands, the RT band and the epr band. From Fig. 5.4, we see that the EPR intensity from sample (a) is much larger than that from (b). On the other hand the ratio of the epr band to the G_V band in (a) and (b) of Fig. 6.2 are different. In (b) the epr fluorescence band has an intensity nearly equal to that of the G_V band. In (a) of the same figure we assume that the epr band is so overwhelming that it makes the G_V band barely visible. There is a remaining problem with making a strong correlation between the EPR result and the fluorescence spectrum. The intensity of the EPR signal for the sample of Fig. 6.2 (c) is between that of (a) and (b). However, almost no epr band component can be seen from the fluorescence spectrum of Fig. 6.2 (c). Thus, we must also consider the other fact: that is, samples in (c) are single crystals, while in (a) and (b) they are polycrystals. So we ascribe the "epr emission" as being related to the EPR intensities from polycrystals. The origin of these differences needs further investigation.

The dependence of the emission intensity of the RT band on temperature, which is the ratio of peak intensities of the RT to that of the G_V band, is shown in Fig. 6.3. The sample under study was an assembly of single crystals. From the figure, we see that R increases much faster when T is above 150 K than when $T < 150$ K. Thus, the RT band is the only emission band that survives at room temperature long enough to contribute to the cw fluorescence spectrum.

By comparing with the spectrum of the non-irradiated sample shown in Fig. 3.2, we see that the emission band with peak energy at 1.76 eV shown in Fig. 6.4 is induced by the intense prolonged radiation of the laser. Therefore, we ascribe this emission band to the emission related to damage of the sample. We assume that the damage is located on the surface of the sample. This should not be confused with what we mean by a doped sample. In the latter cases, the doping is both in the interior and on the surface.

From Fig. 6.4, we see that at 20 K for a radiation-damaged crystal at delay time t=0 ns, the spectrum consists mainly of the G_V band. The spectral shape of the second spectrum, at t=1 ns, however, is totally different from the earlier one. The 1.76 eV component at t=1 ns has an intensity that is approximately two thirds that of the G_V band. We also notice that:

(a). The 1.76 eV band at t=1 ns has an intensity that is actually larger than at t=0 ns.

(b). In comparison to that at t = 0 ns, the peak position of the G_V band has red shifted by approximately 3 meV during the first nanosecond. However, a deconvolution and comparison with the A-> B energy transfer would be necessary to see whether this shift is significant.

From the observations described above, we must conclude that there are energy transfers both from Gv band to the 1.76 eV band and also within the G_V band. The process of intraband energy transfer within the G_V band was discussed in detail in chapter IV and will not be repeated here. Note that the spectra shown in Fig. 6.4 are neither normalized nor deconvoluted. Therefore, we can

imagine that the extent of real energy transfer is either very dramatic or else the 1.76 eV band has much less non-radiative decay. This observation of more than one energy transfer process can help us to understand the fact mentioned in chapter IV (see Fig. 3.7), that the energy loss from the A band is larger than that gained by the B band. Now we can see that the energy transfer from A is not only to B within the G_V band, but also to other lower energy states as well.

Summary

1. Besides the G_V band, three more fluorescence bands are observed. These new bands are the RT band, the "epr band" and the 1.76 eV broad band.

2. The RT band which has an approximately Gaussian shape, a peak energy at 1.7 eV and FWHM of 50 meV is tentatively assigned to excitonic emission related to the grain boundaries of the crystals.

3. The 1.76 eV emission band has a width of about 0.1 eV. This band results from prolonged laser irradiation and forms by energy transfer from the G_V band.

4. The epr band has a peak position at 1.8 eV at 130 K. This band is ascribed to doping in polycrystals. The doping is also responsible for the EPR signals. This epr fluorescence band is assigned to defect-related excitonic emission. However, this assignment is not in agreement with the results for doped single crystals.

CHAPTER VII

OPTICAL ABSORPTION SPECTRA OF $Na^+C222Na^-$ THIN FILMS AT VAROUS TEMPERATURES

Optical absorption studies of $Na^+C222Na^-$ were carried out on thin films. The preparation of the thin films was described in detail in chapter II. The thin films are polycrystalline with an average size of the order of nanometers.[7.1] When the films are properly made, they are transparent to visible light and the optical absorption can be investigated. However, it should be noted that there is no control over the thickness or homogeneity of the films. It has been noted that the absorption spectra from films with variable thicknesses can have different shapes.[7.2] Therefore, in the study of the temperature dependence, in every individual experiment (either fluorescence or absorption studies) the illumination spot was unchanged. This is the first time the absorption spectra have been studied over a wide temperature range.

Results

Two absorption spectra are shown in Fig. 7.1. The experimental temperatures are, from the top to the bottom, 12 and 225 Kelvin.

Data analysis and discussion

1). Dependence of the absorption peak position on temperature. From Fig. 7.1 we see that the absorption peak shifts with

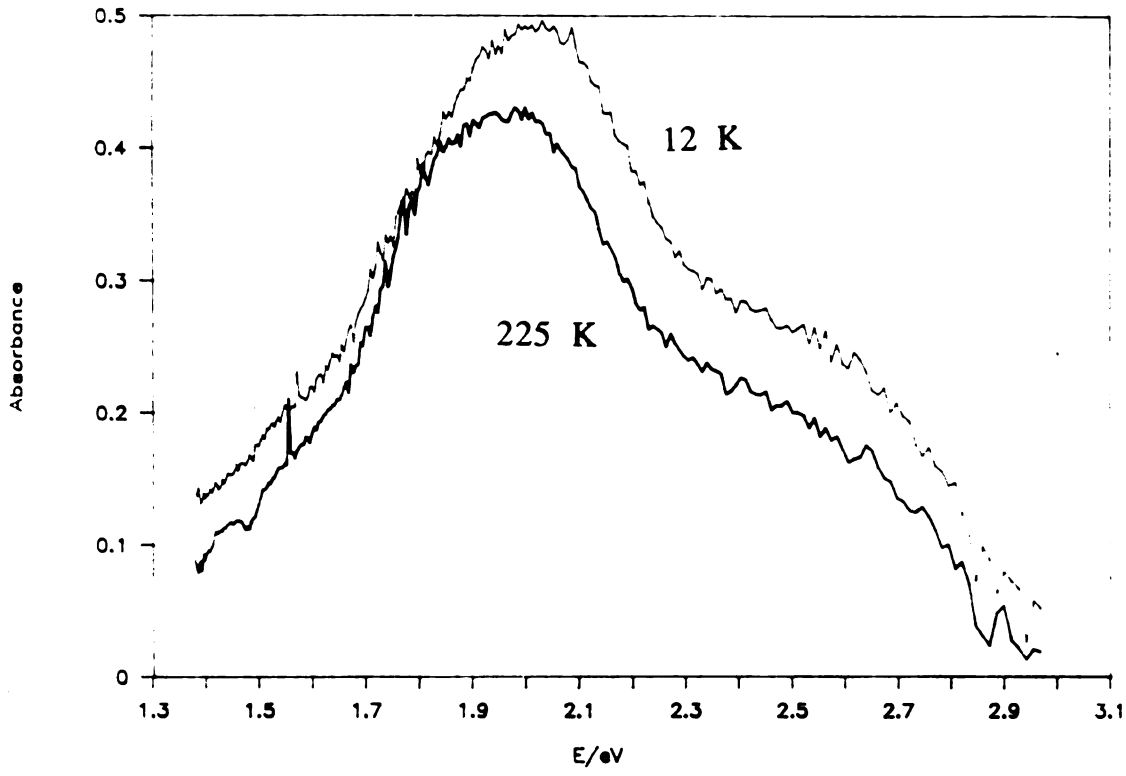

Fig. 7.1. Optical absorption spectra at 12 K and 225 K from solvent (dimethyl ether) evaporated thin films of $Na^{+}C222Na^{-}$.

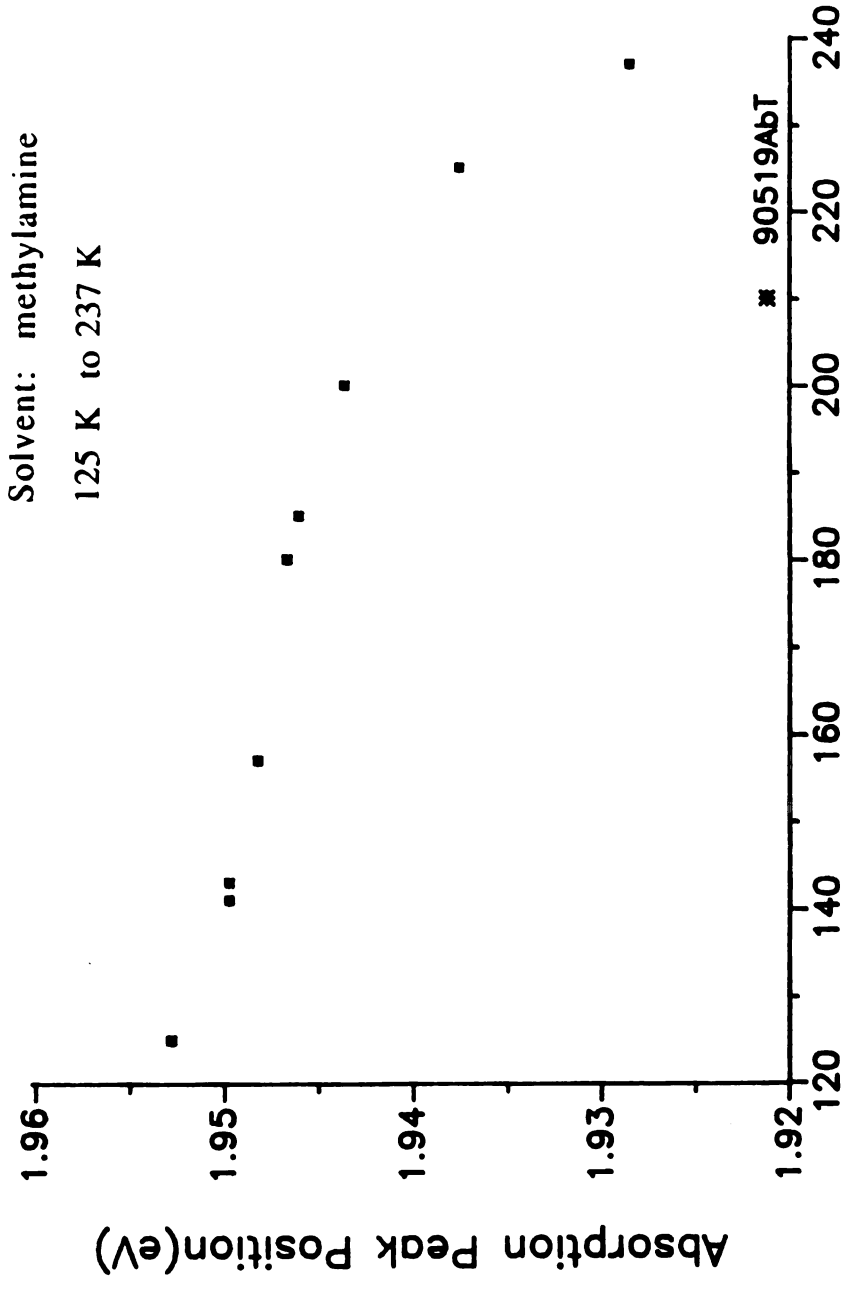

Fig. 7.2. Temperature dependence of the absorption peak position of the spectra from thin films of $Na^{+}C222Na^{-}$.

temperature. This shift, starting at 125 K, is plotted in Fig. 7.2. The peak is at 1.953 eV at 125 K. Below 200 K, as T increases, the peak position shifts with a rate of -0.12 meV/K. When T is above 200 K, however, the peak position shifts to the red with a rate that approaches -0.7 meV/K.

2). Dependence of the absorption band shape on temperature

When the temperature changes, the absorption peak position changes. This can be seen clearly from Fig. 7.1 and Fig. 7.3. The difference spectrum in Fig. 7.4 was obtained from Fig. 7.3 by subtracting the spectrum at T = 270 K from the one at T = 154 K. Fig. 7.5 was obtained similarly to Fig. 7.4. Note that, the absorption spectra of Fig. 7.5 were from the same spot.

3). From Fig. 7.5 we see that, at the energy region of about 1.85 eV, the magnitude of A(237 K) - A(125K) is much larger than that of A(180 K) - A(125K), where A(237K) represents the absorbance at 237 K.

Discussion

a). The spectra at all temperatures are found to consist of a main band on the low energy side and a shoulder on the high energy side.

(b). From Fig. 7.3 and Fig. 7.4 we see that the absorbances in different energy regions respond to temperature changes differently. When T is increased, the absorbance increases in energy region I, centered at 1.85 eV, but decreases in energy region II, centered at 2.0 eV. Region I in Fig. 7.4, has approximately the same energy as that of the emission band at low temperatures, while the energy range of region II is the same as that of an higher energy

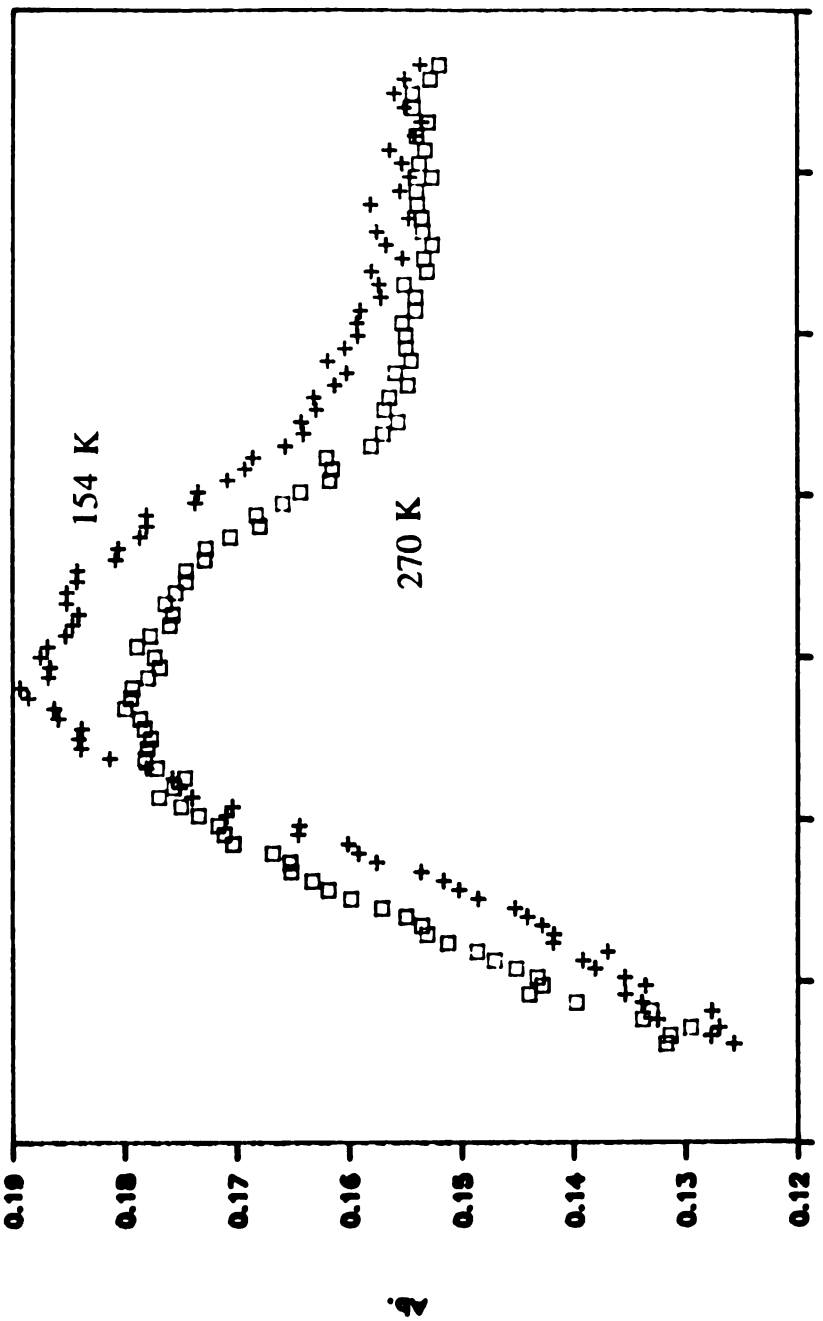

Fig. 7.3. Optical absorption spectra at 154 K and 270 K from solvent (methylamine) evaporated thin films of $Na^{+}C222Na^{-}$.

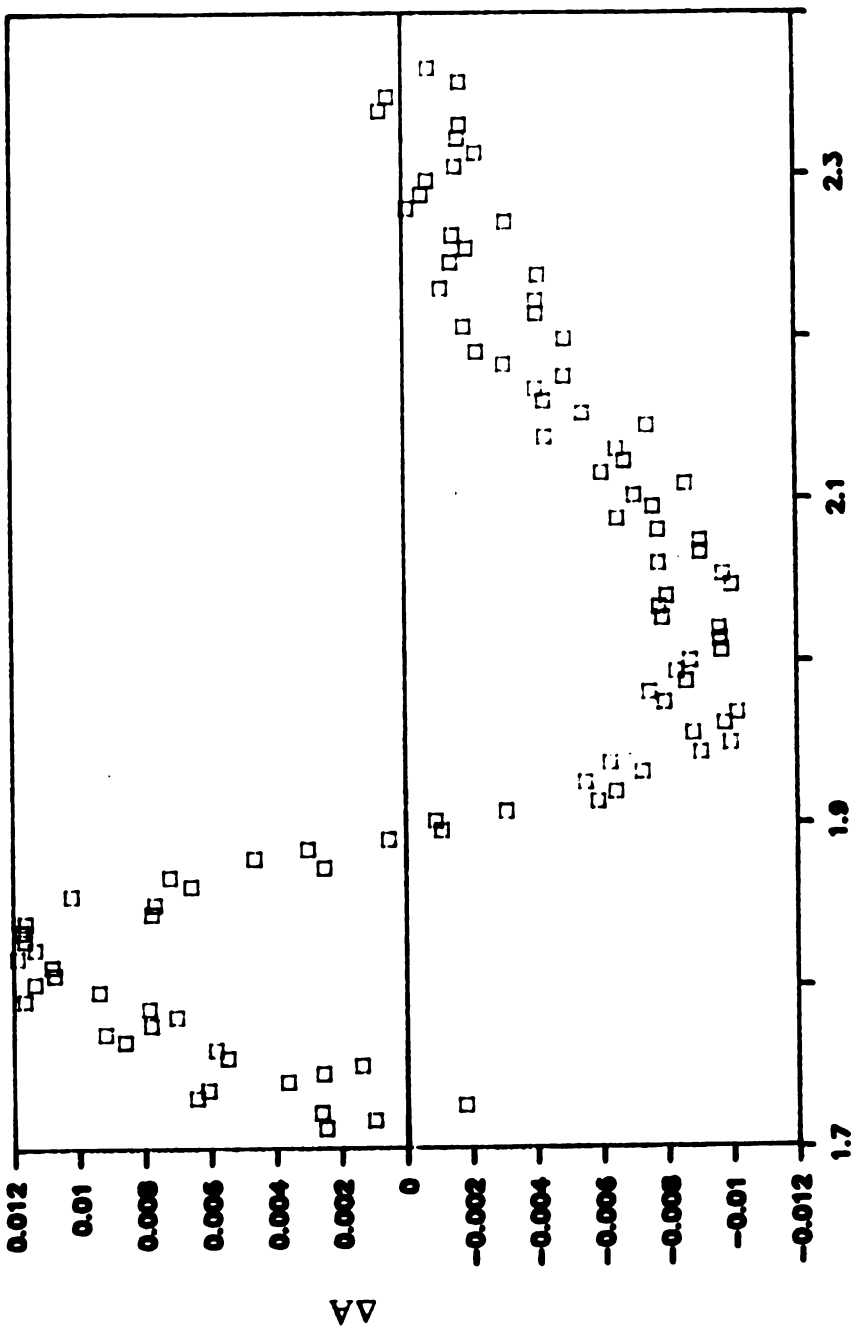

Fig. 7.4. Difference absorption spectrum, $\Delta A = A(270\ K) - A(154\ K)$, obtained by subtracting the one of T=154 K from that T=270 K shown in Fig. 7.3.

emission peak seen in the fluorescence spectra.[7.3] Therefore, we consider that region I in Fig. 7.4 is the state that is in resonance with the fluorescence (the Gv band) because they are in the same energy region. As we have seen before, in the energy region between 1.7 and 1.9 eV, there are two energy bands, A and B which are centered at 1.85 and 1.82 eV. We presume that these two states form an indirect valley. This means that, in k space, they are not vertically above the k = 0 maximum of the valence band. Conservation of energy and momentum requires photon absorption as well as phonon absorption. In our case the required momentum can only be supplied by phonons (the vibration of lattice). As we calculated in chapter IV, the phonon energy that assists energy transfer within the G_V band is 25 meV which is equal to the thermal energy at approximately 270 K. We expect, therefore, as T approaches 270 K the absorption of the indirect band will be more pronounced than that at low temperatures which will result in the red-shift of the whole absorption spectrum. Therefore, the observations from absorption studies are in accord with Model 1 described in chapter IV.

The decrease of absorbance with an increase of T in region II should be further studied. It is probable that it is due to phonon assisted energy transfer. Because the Gv emission band overlaps with the absorption band, phonon assisted energy transfer can take place. Therefore, region II may represent an energy region where energy transfer to lower energy states is pronounced.

References

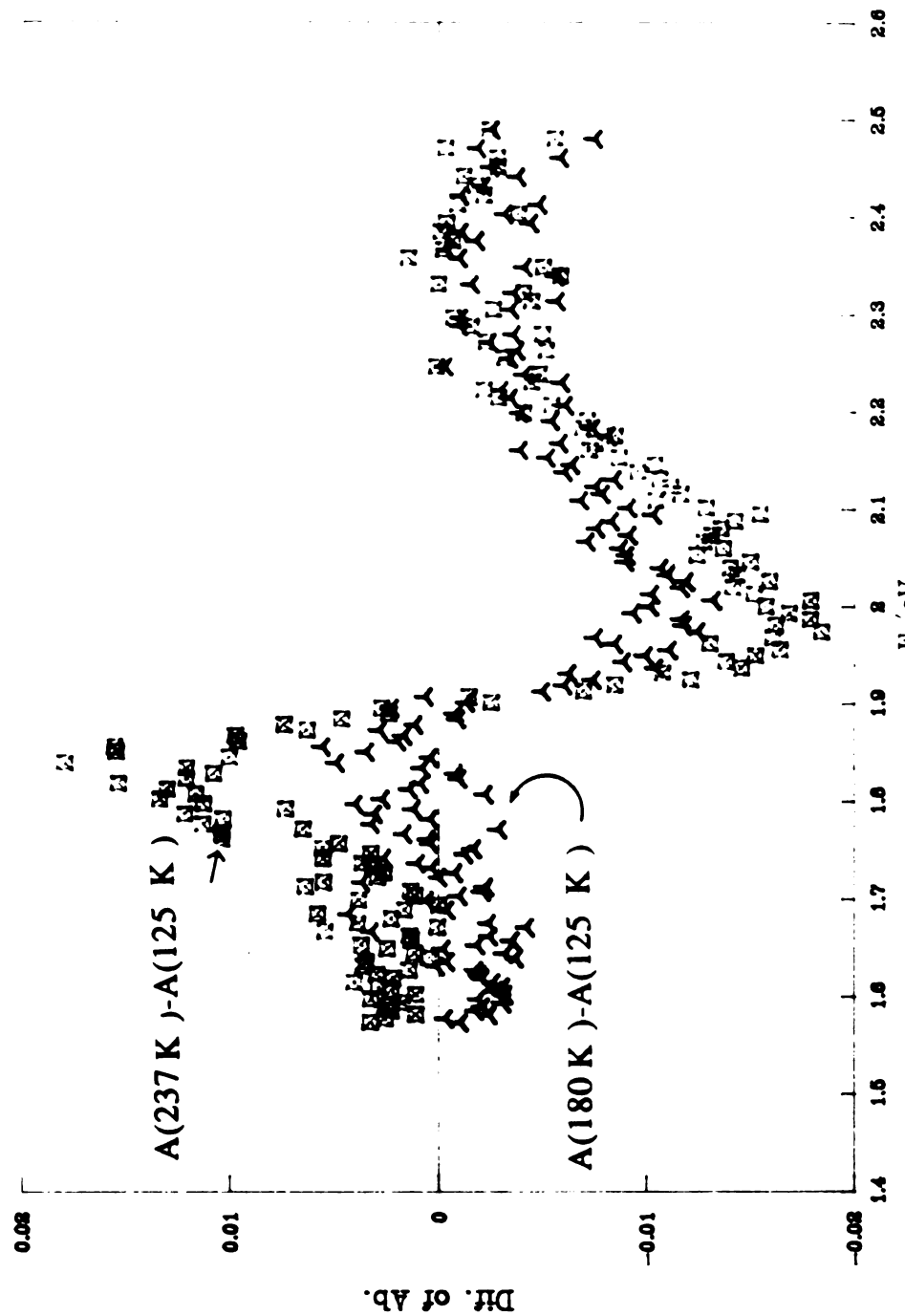

Fig. 7.5. Difference spectra obtained by subtracting the absorption spectra from solvent (methylamine) evaporated thin films of $Na^{+}C222Na^{-}$.

7.1. Electron microscope observation in this Lab. by J. Kim, R. Bannwart and J. Dye.

7.2. John Steven Landers, Ph. D. Dissertation, Michigan State University, 1981.

7.3. G. Xu, Ta.-R. Park, R. S. Bannwart, A. Sieradzan, M. G. DeBacker, S. A. Solin and J. L. Dye, Figure 3, Journal De Physique IV Colloque C5 Supplement au Journal de Physique I, Vol. 1, December 1991.

CHAPTER VIII

OPTICAL ABSORPTION AND FLUORESCENCE FROM $Rb^+(15C5)_2Na^-$

Results of optical absorption studies

Optical absorption spectra obtained at 121 K and 263 K are shown in Fig. 8.1 and the temperature dependence of the peak position is shown in Fig. 8.2. From these figures we see that :

(a). Each spectrum has a main absorption peak and a shoulder on the high energy side of the peak. For the spectrum at 121 K, the peak position is at approximately 1.82 eV and the shoulder is at 2.38 eV. Comparison with the spectrum at 263 K shows that the peak position is shifted in the direction of longer wavelength at higher temperature, but that the position of the shoulder is basically unchanged.

(b). The dependence of peak energy on T shows that for $T < 210$ K, the absorption peak shifts to lower energies at a rate of 0.16 meV/K. When $T > 240$ K, the rate increases to 0.5 meV/K.

(c). As T increases, the absorbance decreases.

(d). There are low energy tails in each curve of Fig. 8.1, but it is difficult to evaluate the extent of absorption in this region because of the poor baseline.

Results of luminescence studies

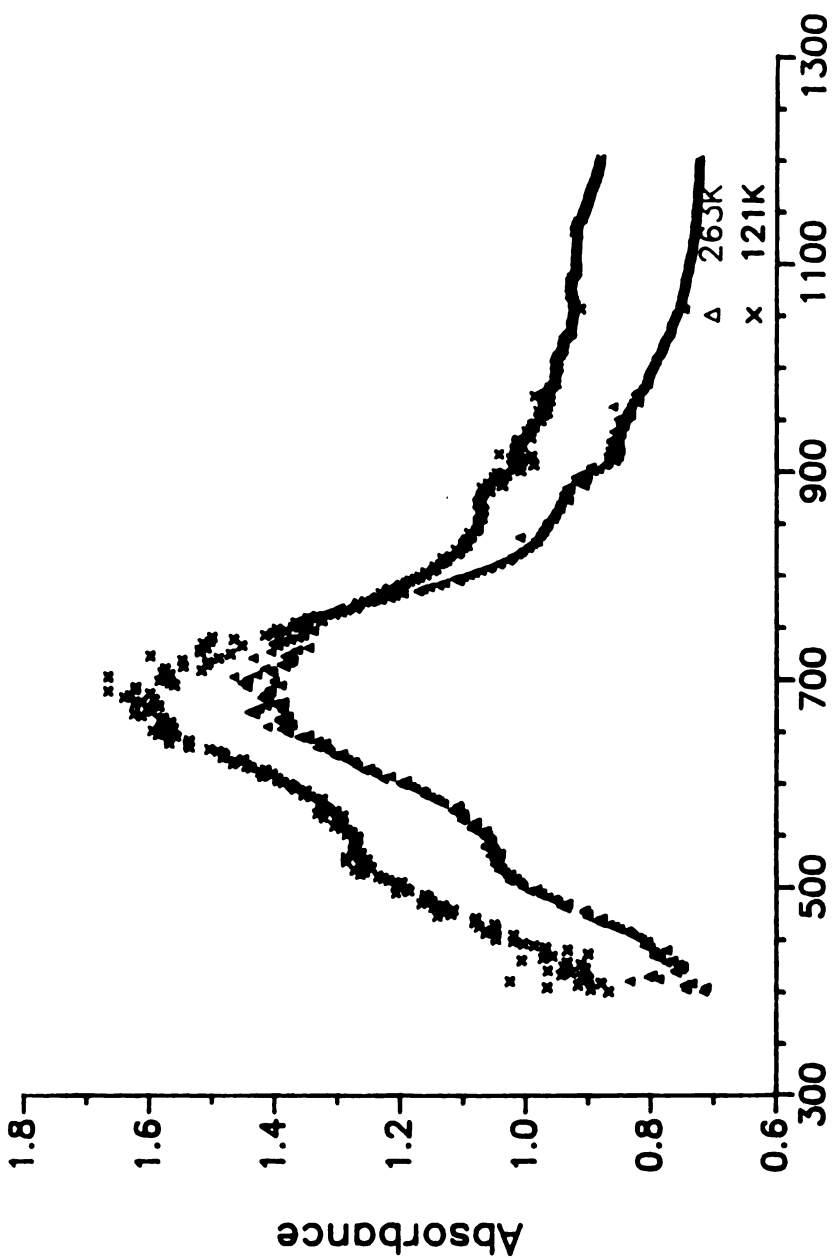

Fig. 8.1. Optical absorption spectra of a thin film of $Rb^{+}(15C5)2Na^{-}$. Temperatures are, from the top to the bottom, 121 K and 263 K. The apparent background absorbance is high, probably due to the scattered light from the polycrystalline film.

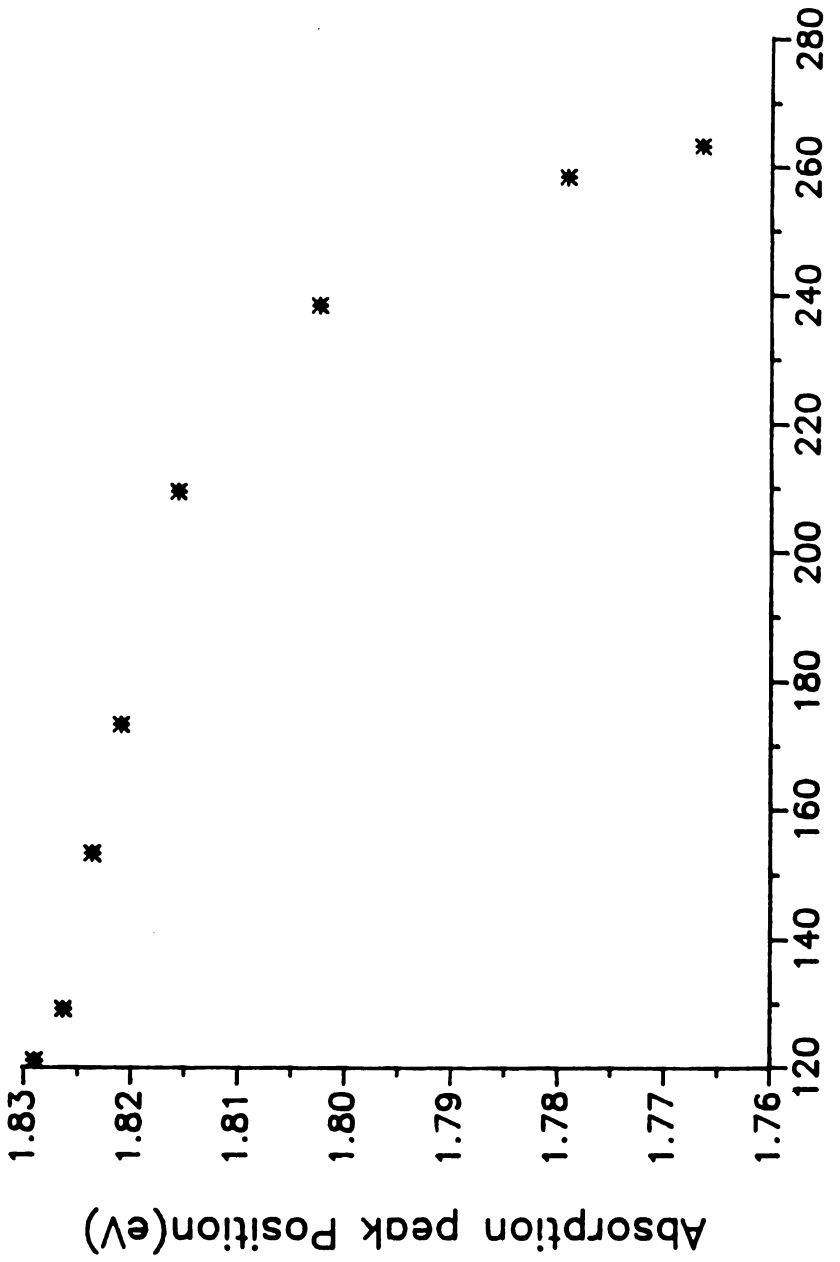

Fig. 8.2. Temperature dependence of the absorption peak position for $Rb^{+}(15C5)2Na^{-}$.

(a) The luminescence spectrum at 25 K is shown in Fig. 8.3 along with the absorption spectra at 121 K. The emission spectrum has no structure and has a peak position of 1.68 eV.

b). The band shape of the luminescence spectrum shown in Fig. 8.3 is shown in Fig. 8.4 on a different scale. The squares are experimental values, while the continuous curve is a Gaussian function with peak energy at 1.68 eV and FWHM = 50 meV. The inset in the figure shows a log plot of the luminescence intensity against energy on the low energy side of the peak.

(c). The dependence of the emission intensity, I_{em}, at the peak position on temperature is shown in Fig. 8.5. The intensity decreases as T increases approximately as a pair of straight lines. When $T < 50$ K the intensity decreases at a rate of 2.5 percent/K. When $T > 50$ K the intensity decreases at a rate of 0.3 percent/K.

(d). The dependence of I_{em} on the excitation intensity I_{exc}, (on a log-log plot), is shown in Fig. 8.6, which shows that I_{em} is a linear function of I_{exc} because the slope of the log-log plot is 1.0 ± 0.05.

(d). A fluorescence decay curve at 1.7 eV is shown in Fig. 8.7. The IRF curve is very close to the decay curve, which means the emission lifetime is very short.

(e). The variation of the decay constant with energy is shown in Fig. 8.8. The τ values are obtained by fitting the deconvoluted decay curve to a single exponential. Note that the decay is faster on the high energy side than on the low energy side. The decay time is nearly constant from 1.57 to 1.65 eV

Discussion

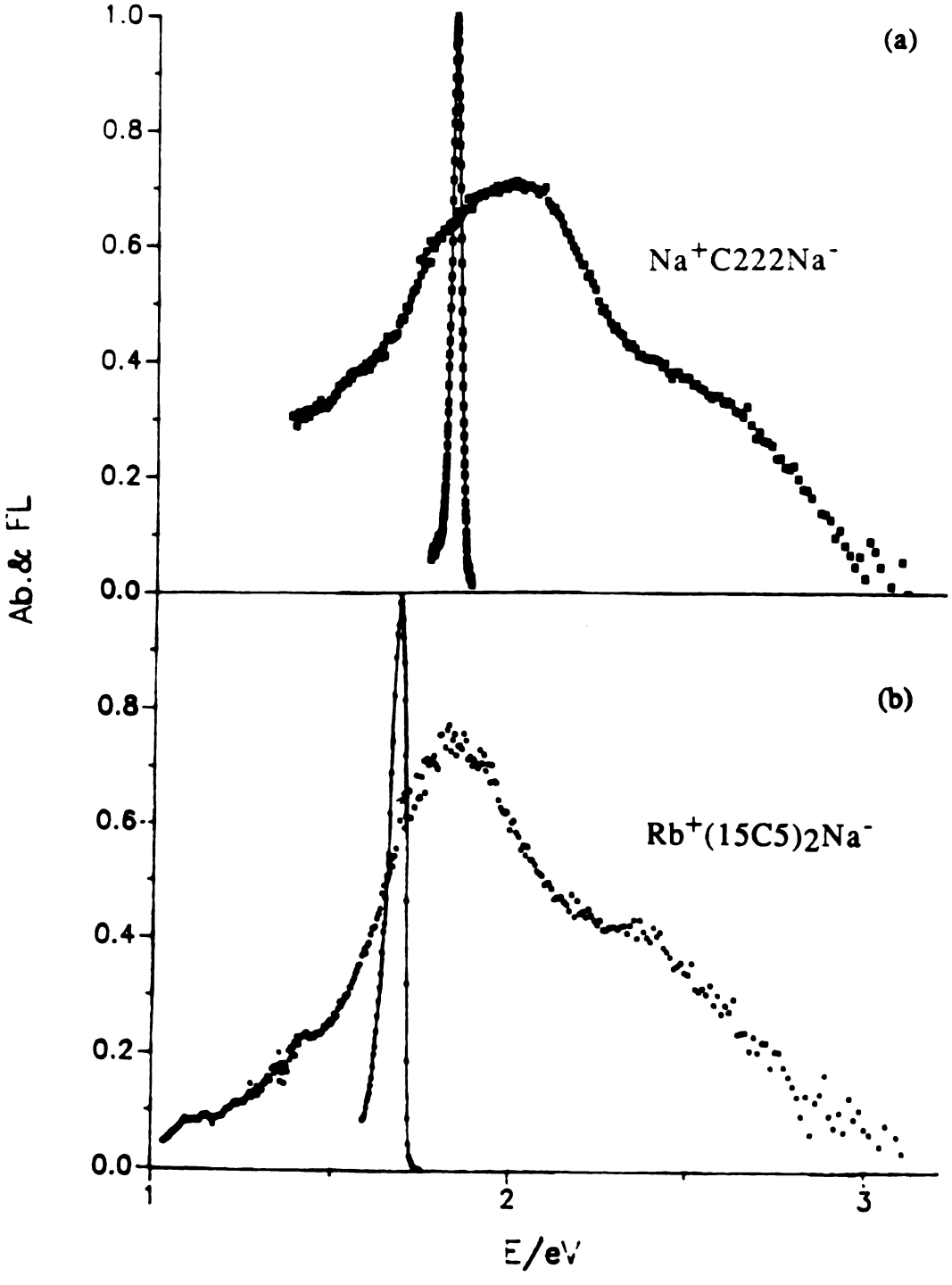

Fig. 8.3. Absorption (broad) and luminescence (narrow) spectra of $Na^+C222Na^-$ (a), and $Rb^+(15C5)_2Na^-$ (b). See text for the experimental conditions.

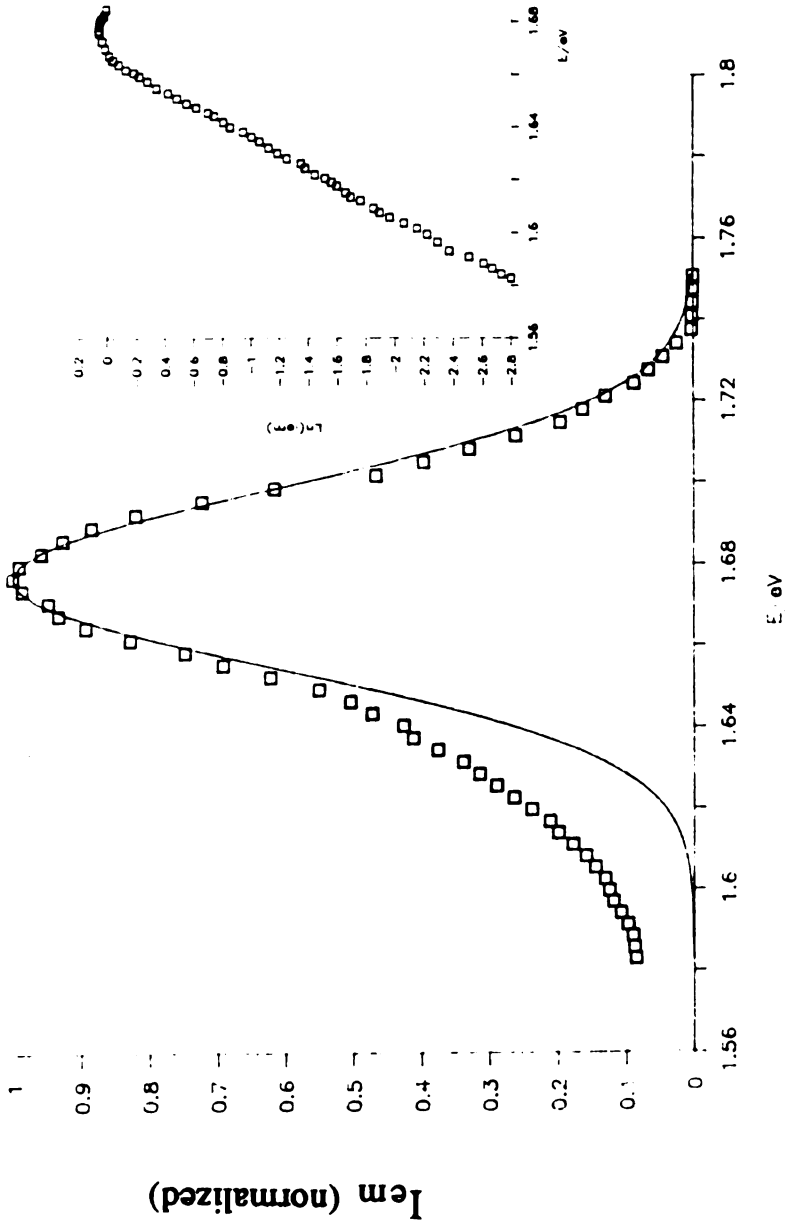

Fig. 8.4. Band shape for the fluorescence spectrum shown in Fig. 8.3. The solid line shows a Gaussian fit to the data on the high-energy side. The inset shows the logarithmic behavior on the low-energy side.

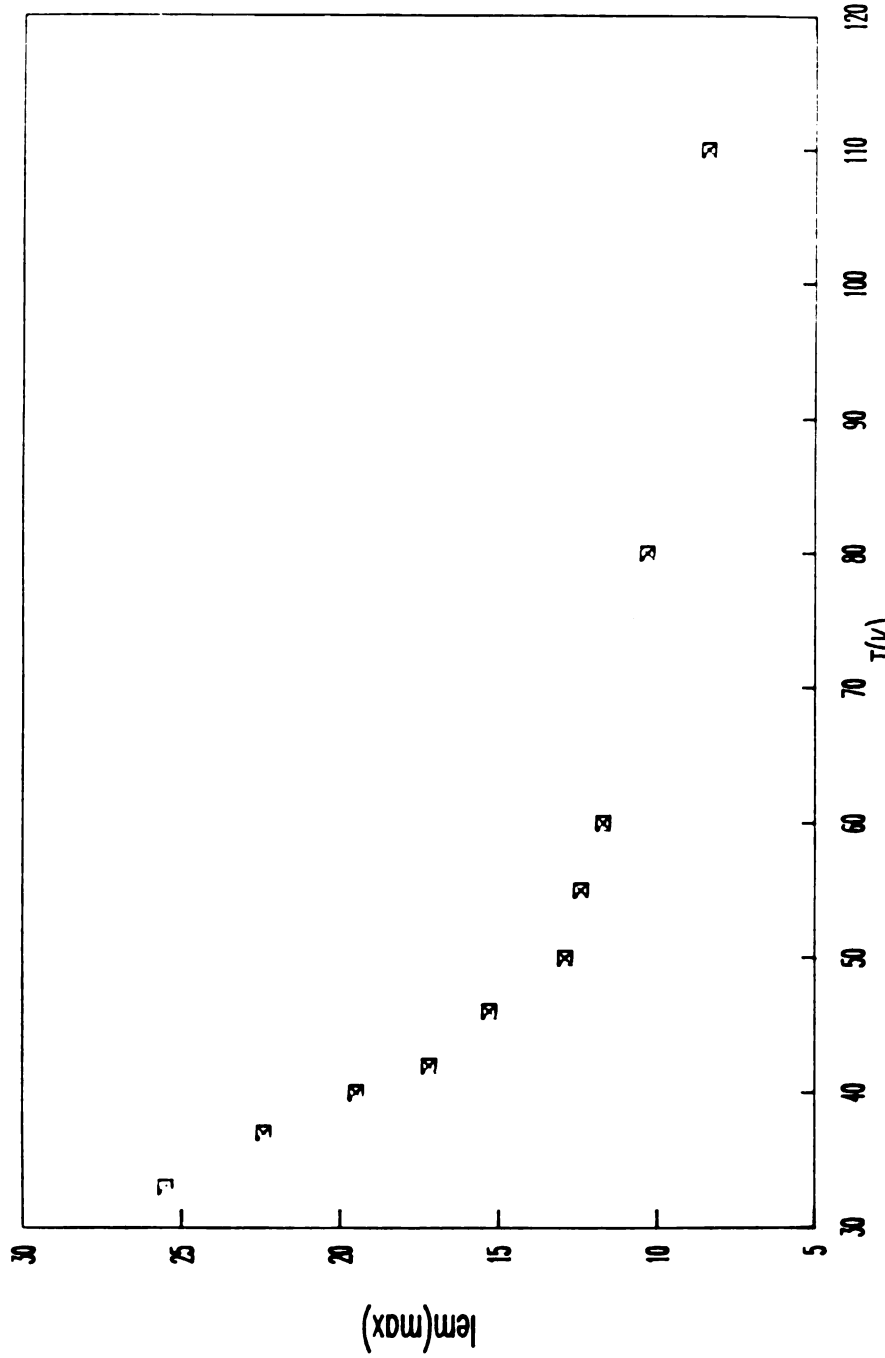

Fig. 8.5. Dependence of the photoluminescence intensity on temperature at the peak position for $Rb^{+}(15C5)_2Na^{-}$.

In many respects the absorption and emission spectra of $Rb^+(15C5)_2Na^-$ are similar to those observed with $Na^+C222Na^-$. This is not surprising since both are sodides and Na^- is the species involved in both absorption and fluorescence. The similarities are:

A). Absorption spectra:

(a). The band shapes are similar; each has a main peak and a high energy shoulder.,

(b). The peak position shifts to the red with an increase in temperature in both cases.

B). . Emission spectra:

(a). The band shapes are similar. In particular, both show an Urbach tail on the low energy side and Gaussian behavior on the high energy side.

(b). Variation of τ with energy. For comparison, the average τ values at different temperatures for $Na^+C222Na^-$ are also shown in Fig. 9.12.

C). The absorption and emission spectra of the two sodides have the following differences:

(a). The emission intensity from $Rb^+(15C5)_2Na^-$ is three orders of magnitude weaker than that from $Na^+C222Na^-$.

(b). The average τ values for $Rb^+(15C5)_2Na^-$ is about 5 times smaller than that of $Na^+C222Na^-$.

(c). The low energy tail in the absorption spectrum of $Rb^+(15C5)_2Na^-$ is more pronounced than that of $Na^+C222Na^-$.

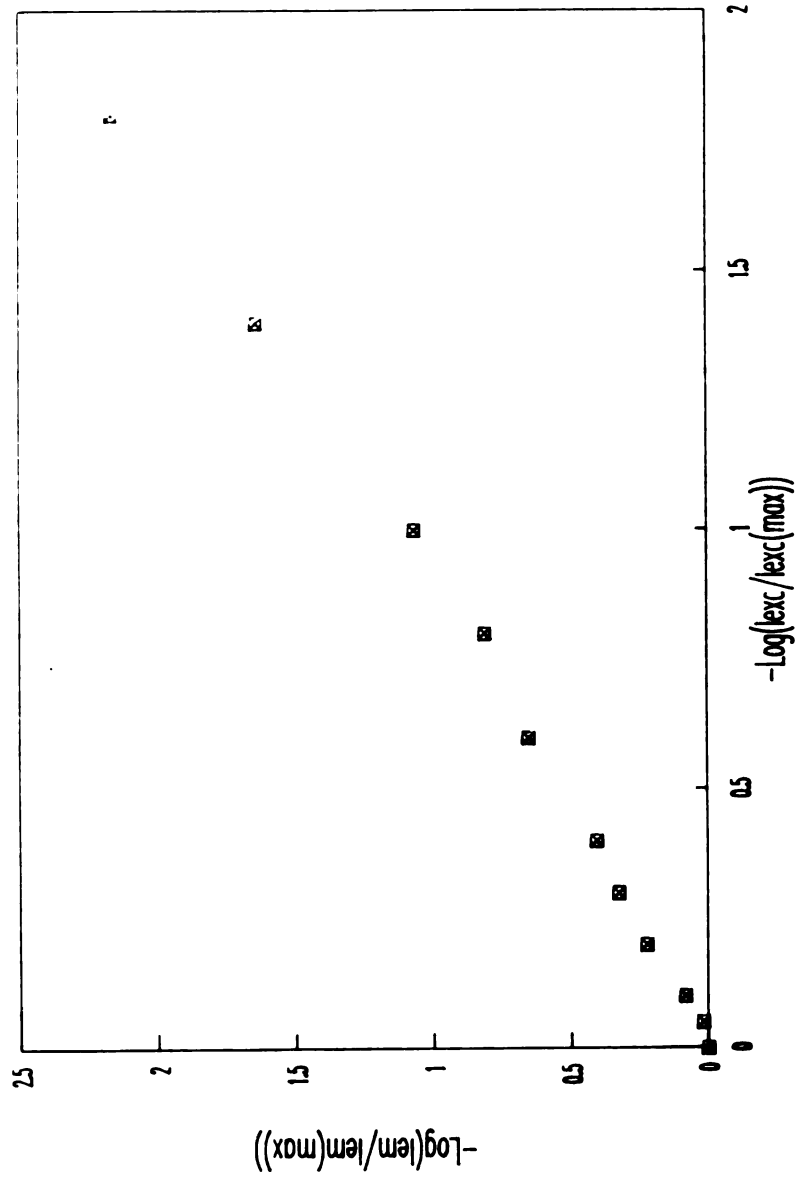

Fig. 8.6. Dependence of the photoluminescence intensity on the excitation intensity for $^{+}$(15C5)2Na^{-} at 26 K.

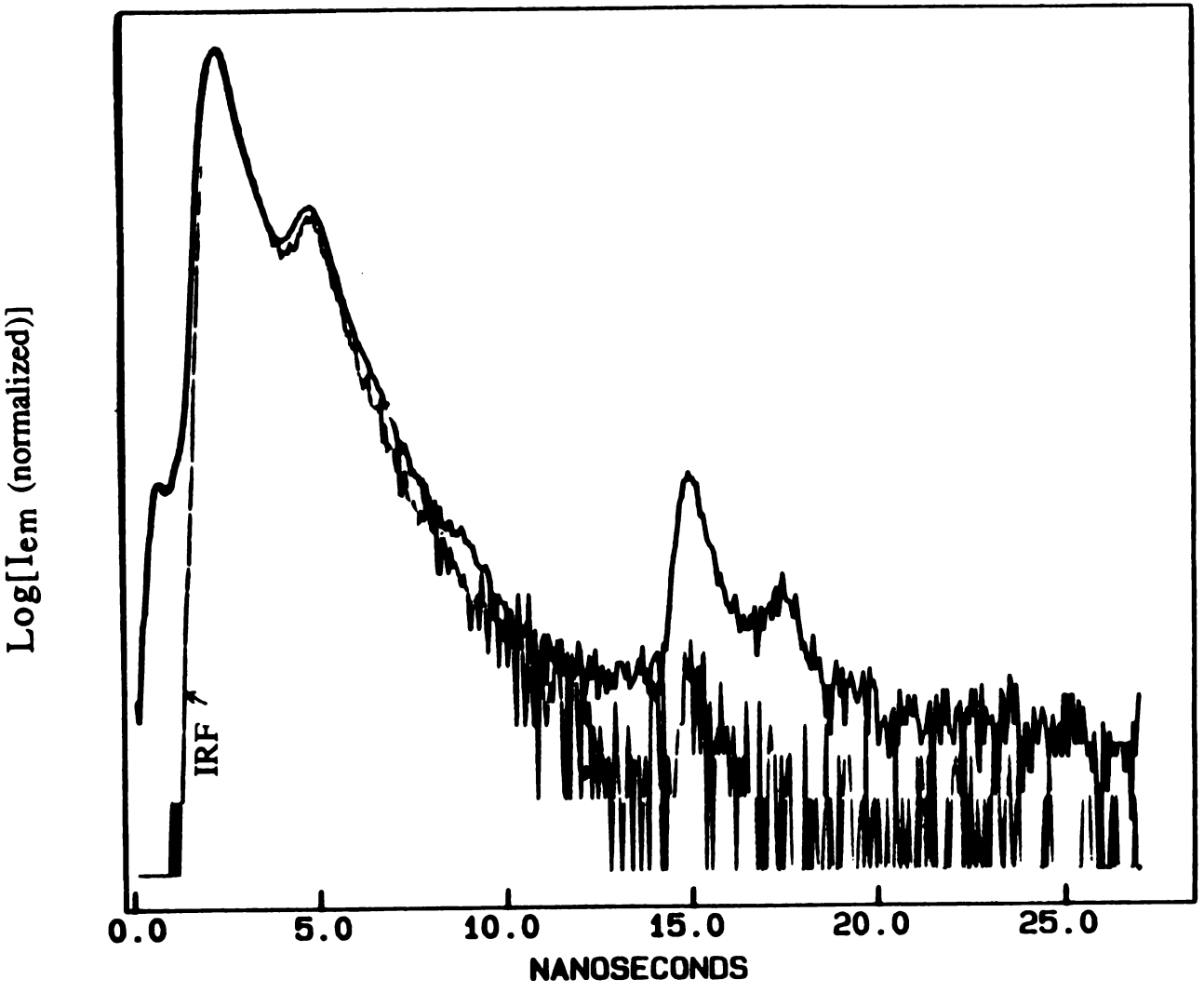

Fig. 8.7. Log plot of IRF (bottom) and the non-deconvoluted decay curves (top) for $Rb^{+}(15C5)_2Na^{-}$ at E=1.7 eV, T=25 K.

The large absorption tail probably originates from trapped electrons. Trapped electrons (and probably other defects) serve as efficient quenchers of luminescence. If the concentration of trapped electrons or other the defects is high, the fluorescence in the compound is quenched and the lifetime will be shortened. This agrees with the general observation that the concentration of trapped electrons in $Rb^{+}(15C5)_2Na^{-}$ and in most other sodides, is much greater than that in $Na^{+}C222Na^{-}$, as observed by EPR and susceptibility experiments.[1,5]

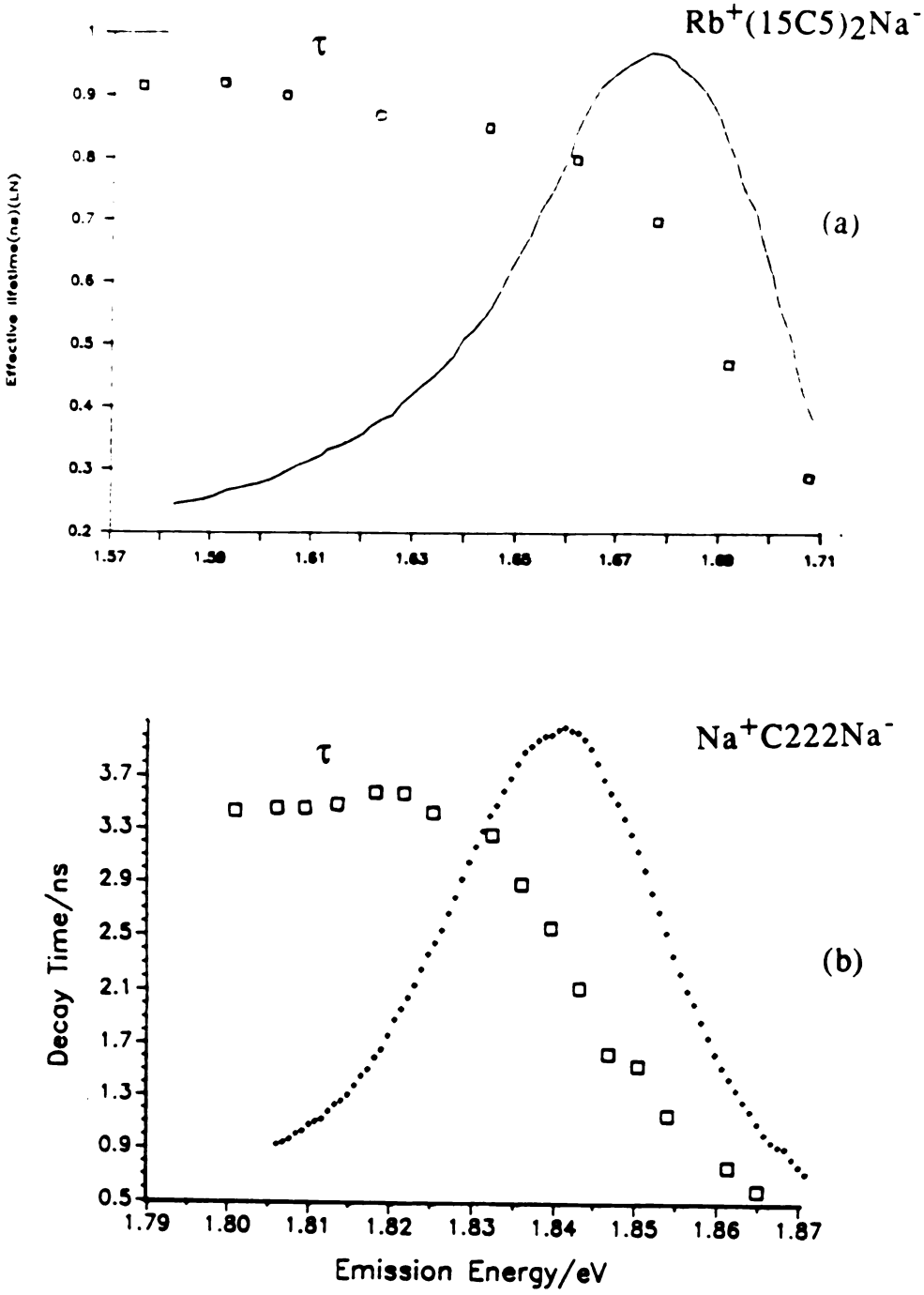

Fig. 8.8. The squares are average fluorescence decay time constants from two crystalline sodides. (a) is from $Rb^+(15C5)_2Na^-$ at 77 K, and (b) is from $Na^+C222Na^-$ at T=25 K. The corresponding spectra are also shown for comparison.

CHAPTER IX

FLUORESCENCE FROM OTHER SODIDE CRYSTALS

Fluorescence spectra from $K^+HMHCYNa^-$, $Rb^+HMHCYNa^-$, $Na^+C221Na^-$, and $Cs^+HMHCYNa^-$ have been studied and the results are reported and discussed here. In this chapter, if not specified otherwise, the excitation source for the cw spectra is a YAG pulsed laser (532 nm) at a low excitation density, while for decay curves, the emissions were obtained at the peak energies of the spectra under study.

Results

1). Absorption and fluorescence from $K^+HMHCYNa^-$.

Absorption and fluorescence spectra on the same energy scale for $K^+HMHCYNa^-$ are shown in Fig. 9.1. The expanded fluorescence spectrum is shown in Fig. 9.2. The absorption spectrum in Fig. 9.1 was measured with solvent-evaporated films at 150 K. [9.1] The emission was from a collection of single crystals at 27 K.

From the two figures we can see that:

(a). The entire emission spectrum is within the absorption band.

(b). The fluorescence peak position is approximately 0.2 eV below the absorption peak.

(c). The emission spectrum is structureless with a band width of about 1 eV.

(d). The shape of the luminescence spectrum on the low energy side is exponential.

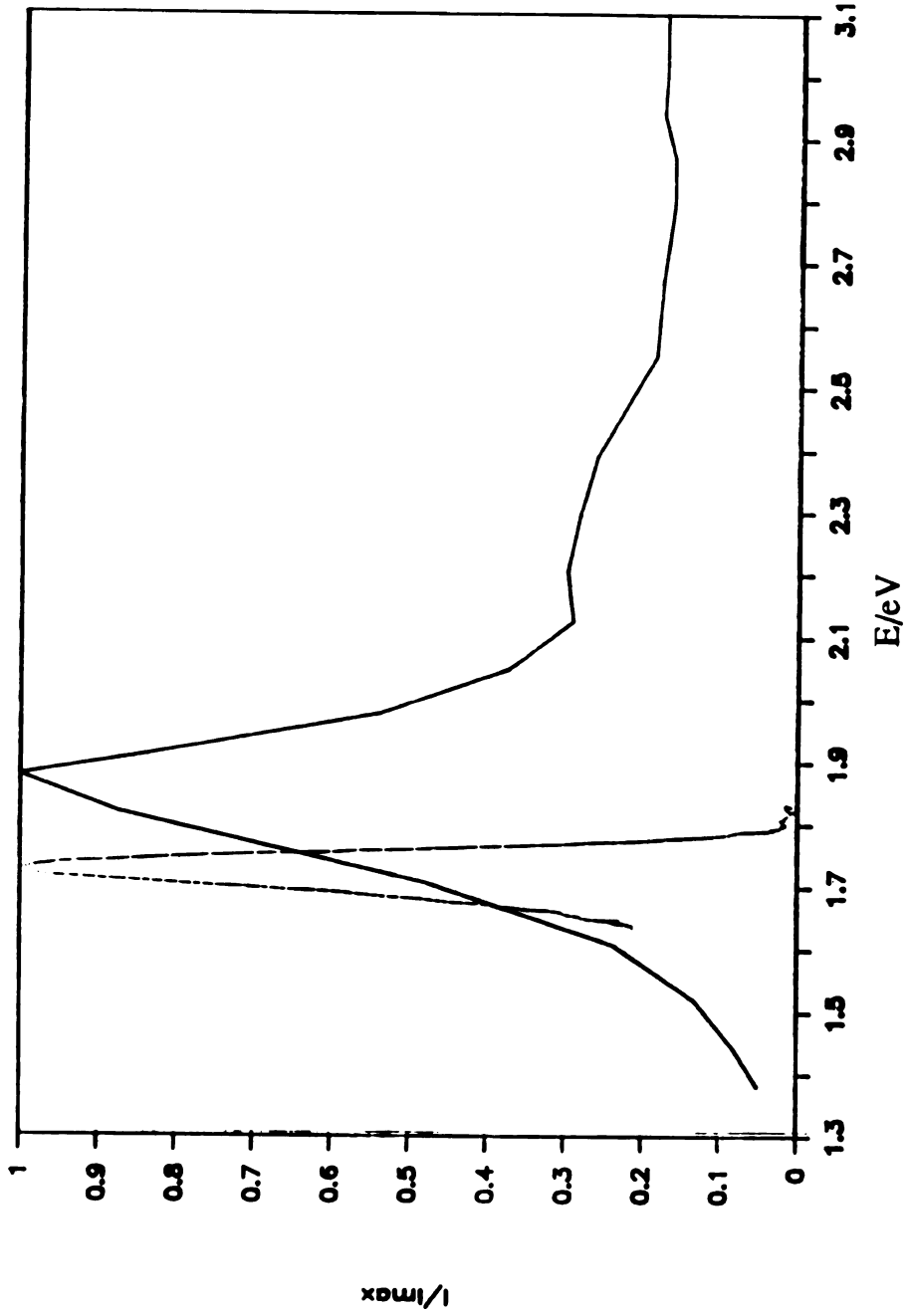

Fig. 9.1. The optical absorption spectrum at 150 K (broad) and the luminescence spectrum at 27 K (narrow) for $K^+HMHCYNa^-$.

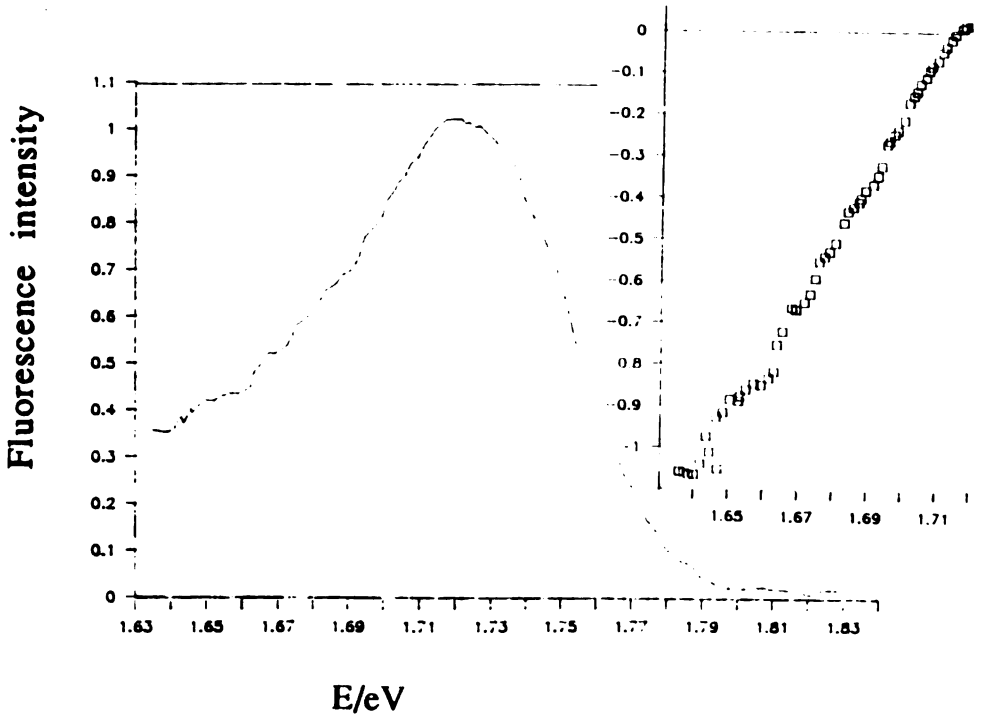

Fig. 9.2. An expansion of the fluorescence spectrum shown in Fig. 9.1. The plot in the inset is the logarithmic behavior on the low-energy side of the spectrum.

The fluorescence decay curves for $K^+HMHCYNa^-$ at 26 K, 57 K, 120 K and the IRF decay curve, are shown in Figs. 9.3 and 9.4. The curves in Fig. 9.3 are the original data while those in Fig. 9.4 are horizontally shifted so that the rising portion of each curve coincides. Analysis of these curves shows that:

(a). The IRF has a decay time constant of 0.22 ns.

(b). The decay behavior of the three decay curves is close to that of the IRF curve, which means that the fluorescence lifetimes at all these temperatures are very short.

(c). The decay times follow: $\tau(26\ K) > \tau(57\ K) > \tau(120\ K)$.

Statement (c) was made without a quantitative description. Normally, the τ values are calculated by deconvolution. However, because of the very short decay times of the curves and the low signal-to-noise ratio, meaningful τ values could not be obtained in this way for $K^+HMHCYNa^-$.

2). $Rb^+HMHCYNa^-$, $Na^+C221Na^-$ and $Cs^+HMHCYNa^-$

The emission spectra and decay curves of $Rb^+HMHCYNa^-$, $Na^+C221Na^-$ and $Cs^+HMHCYNa^-$ are shown in Figs. 9.5 though 9.11. The details are given in the legends of each figure.

Discussion

1). The fluorescence data for $K^+HMHCYNa^-$, $Rb^+HMHCYNa^-$, $Na^+C221Na^-$, $Cs^+HMHCYNa^-$ are similar. In particular:

(a). The fluorescences intensities of all the sodides are approximately three orders weaker than that of $Na^+C222Na^-$.

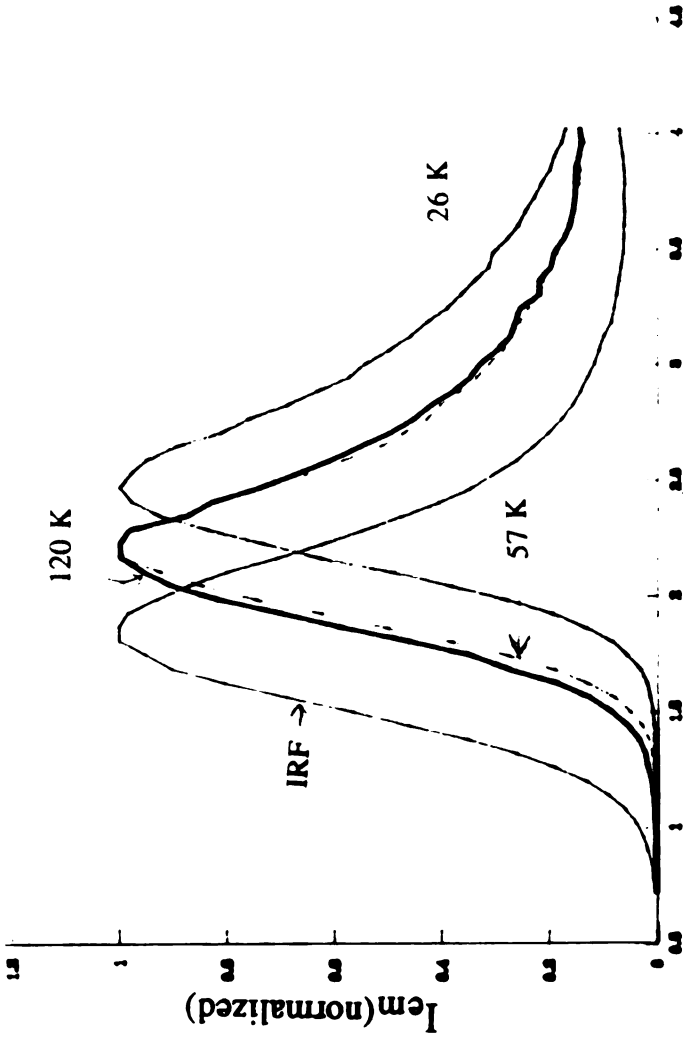

Fig. 9.3. Normalized growth and decay curves of fluorescence for $K^+HMHCYNa^-$ at 26 K, 57 K and 120 K. Horizontal displacement represents variations in the zero of time. The emission energy is at 1.73 eV and the left-most curve is the IRF.

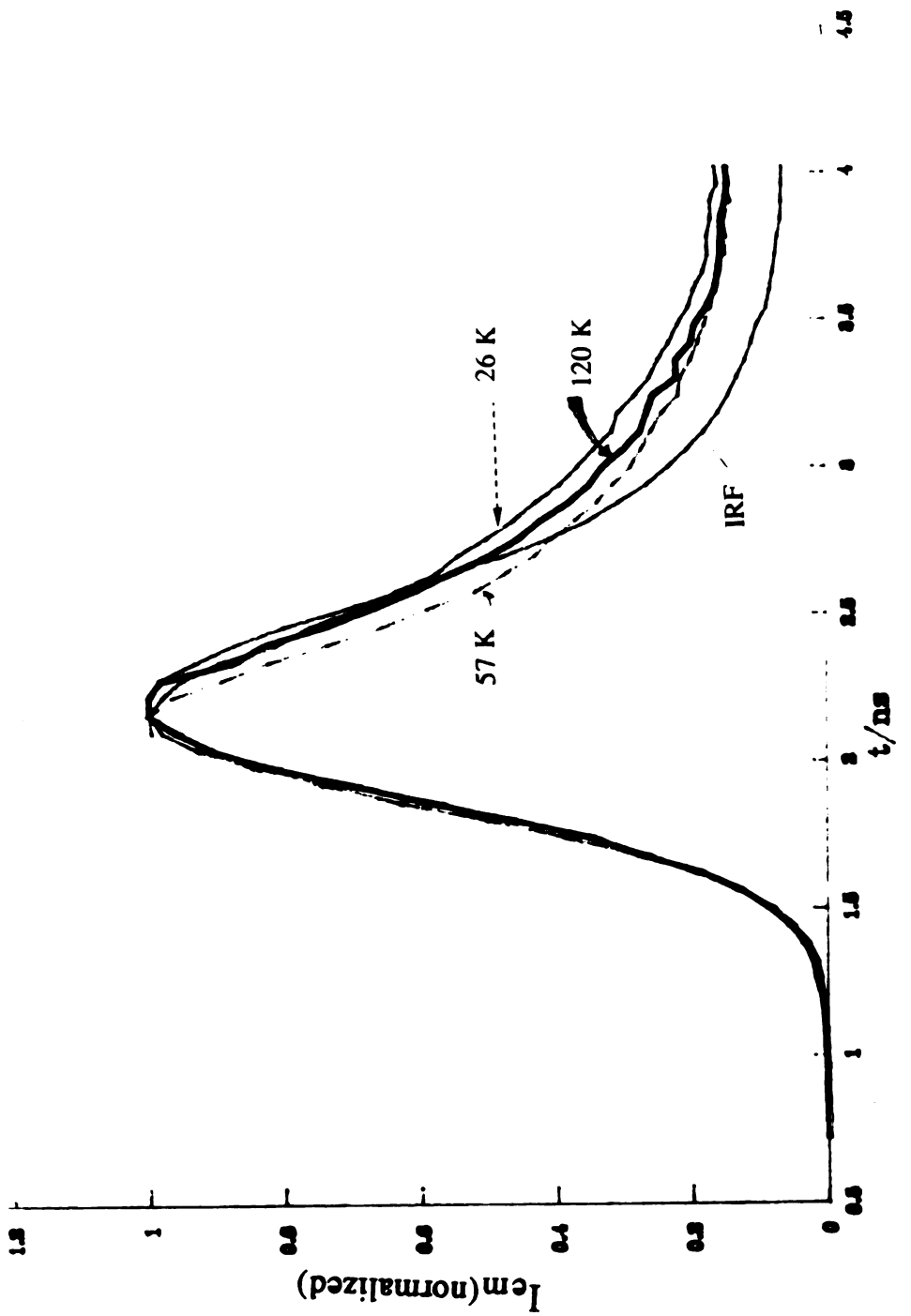

Fig. 9.4. Normalized growth and decay curves of fluorescence for $K^+HMHCYNa^-$ at 26 K, 57 K and 120 K. These are the same data as shown in Fig. 9.3 but have been horizontally shifted to yield a common zero of time.

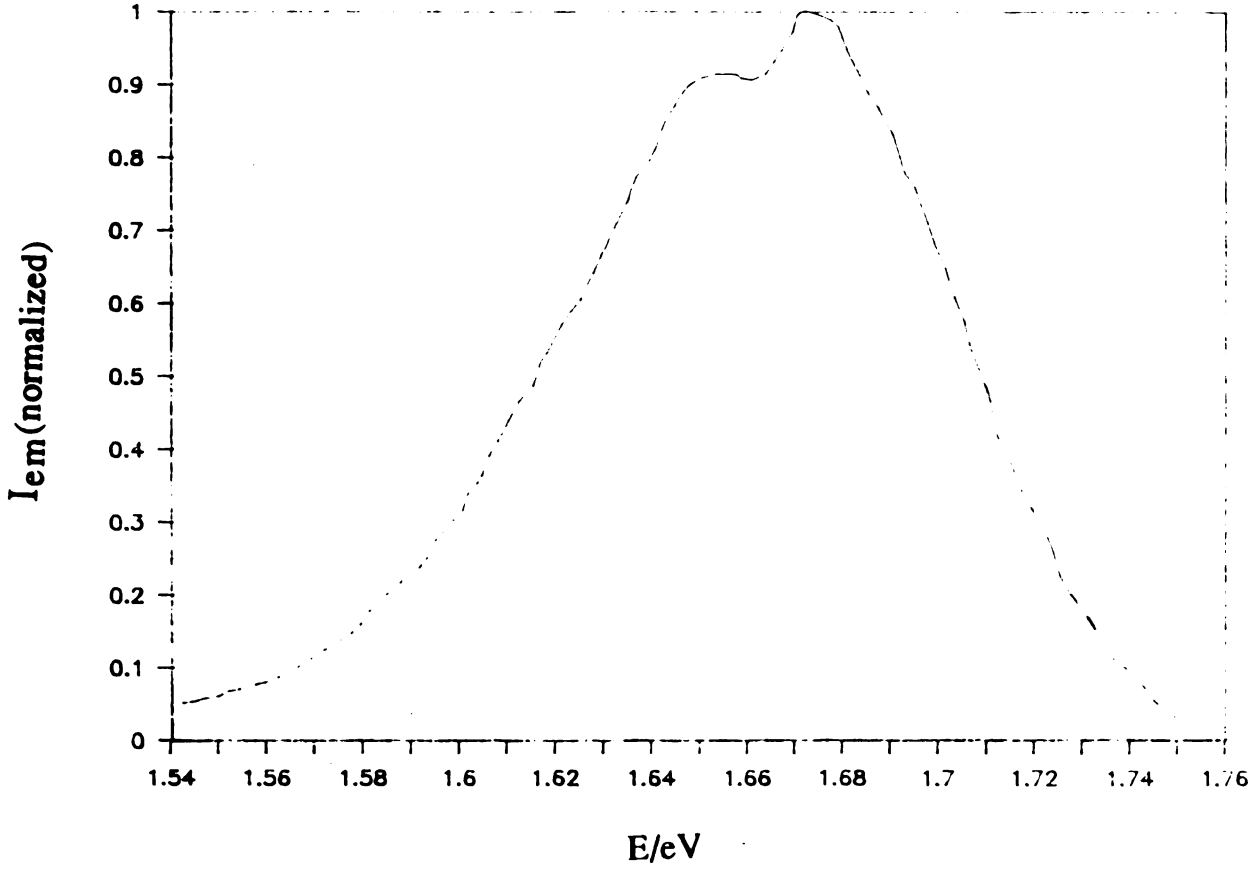

Fig. 9.5. Normalized fluorescence spectrum of $Rb^{+}HMHCYNa^{-}$ at 33 K. Note the split in the band with peaks at 1.65 and 1.67 eV.

(b). The decay constants are much shorter than that for $Na^+C222Na^-$, which is nearly 5 ns.

Observations (a) and ((b) above can be explained by the presence of fluorescence quenchers. We assume that trapped electrons cause reduction of the emission intensity and the decay time constant. The number of trapped electrons should be observable by EPR methods. Indeed, general observations in this laboratory show that $Na^+C222Na^-$ has the lowest concentration of unpaired electrons.

2). The decay time constant τ decreases as T increases.

As seen from Fig. 9.4, the decay time constant of $K^+HMHCYNa^-$ decreases as T increases. This phenomenon, as shown in Fig. 9.12, is also observed with $Na^+C222Na^-$. The τ reduction with an increase in T can be explained as follows:

The lifetime τ, is related to the line width Δh of an intrinsic transition by the uncertainty principle $\tau \sim 1/\Delta h$. As T increases, as we have explained in chapter IV, the number of phonons increases. This increases the interaction between the fluorescence centers, excitons in our case, and the phonons and results in the broadening of the spectrum. Therefore the decay time constant τ decreases as T increases. This statement will be true for any single band of a set of complex bands.

3). The splitting of the $Rb^+HMHCYNa^-$ fluorescence spectrum

Fig. 9.5 shows that spectral shape of $Rb^+HMHCYNa^-$ is different from the other sodides in that it shows a splitting of the spectrum

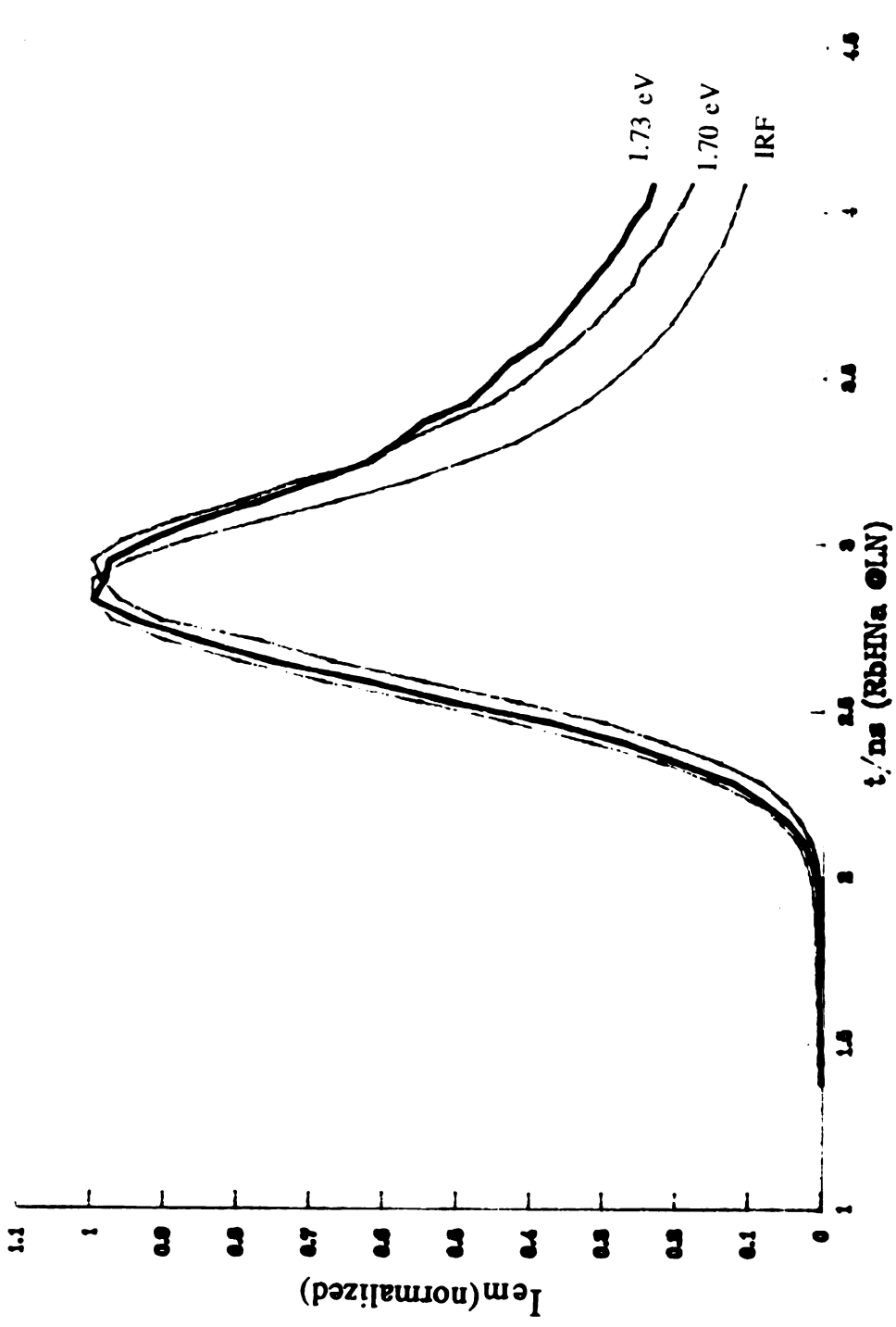

Fig. 9.6. Growth and decay curves of fluorescence from $Rb^+HMHCYNa^-$ at 77 K. The emission energies are, from right to left: 1.73 eV and 1.7 eV. The left-most curve is the IRF.

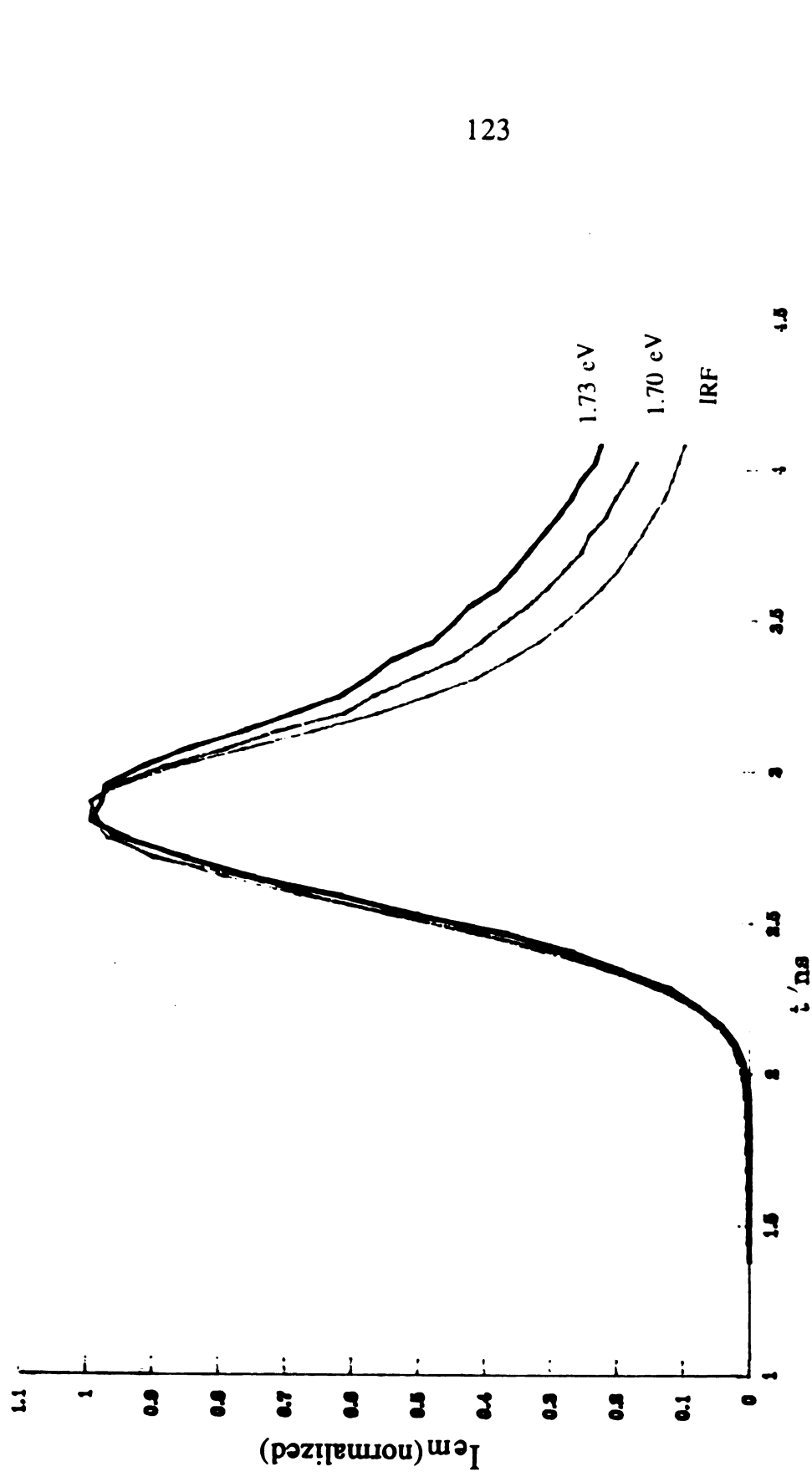

Fig. 9.7. Growth and decay curves of fluorescence from $Rb^{+}HMHCYNa^{-}$ at 1.73 eV (right) and 1.70 eV (middle). These are the same data as shown in Fig. 9.6 but have been horizontally shifted to yield a common zero of time.

with peaks at 1.65 and 1.67 eV. As T increases, the split becomes less pronounced and at approximately 40 K it disappears. This is explained as follows:

The emission band from $Rb^+HMHCYNa^-$ is also assumed to be the superposition of an A band and a B band, as for $Na^+C222Na^-$ discussed in chapter III. But the relative intensities of the A and B bands of $Rb^+HMHCYNa^-$ are different. As a result we see the splitting of the two bands at very low T, so that two peaks become apparent at 27 K. With an increases in temperature, band broadening and, perhaps, an early shift from A and B leaves only one apparent peak.

Reference

9.1. Mark. E. Kuchenmeister, Ph. D. Thesis, Michigan State University,1989.

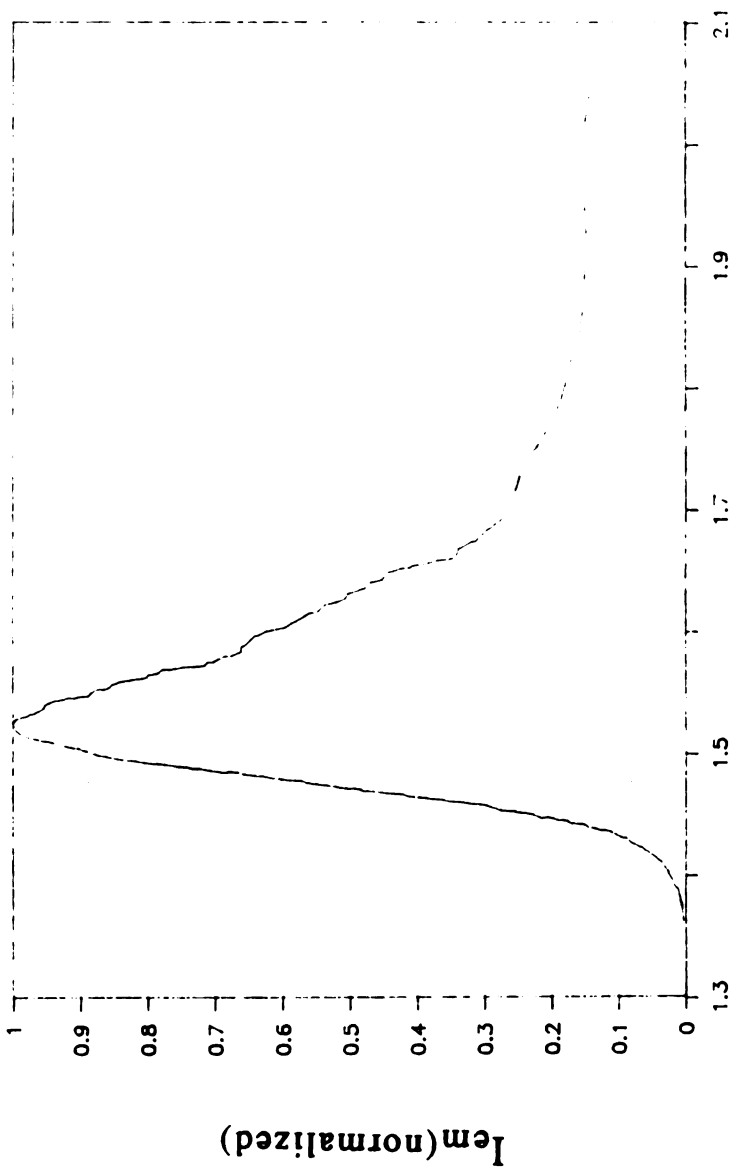

Fig. 9.8. The fluorescence spectrum of $Na^{+}C221Na^{-}$ at 77 K.

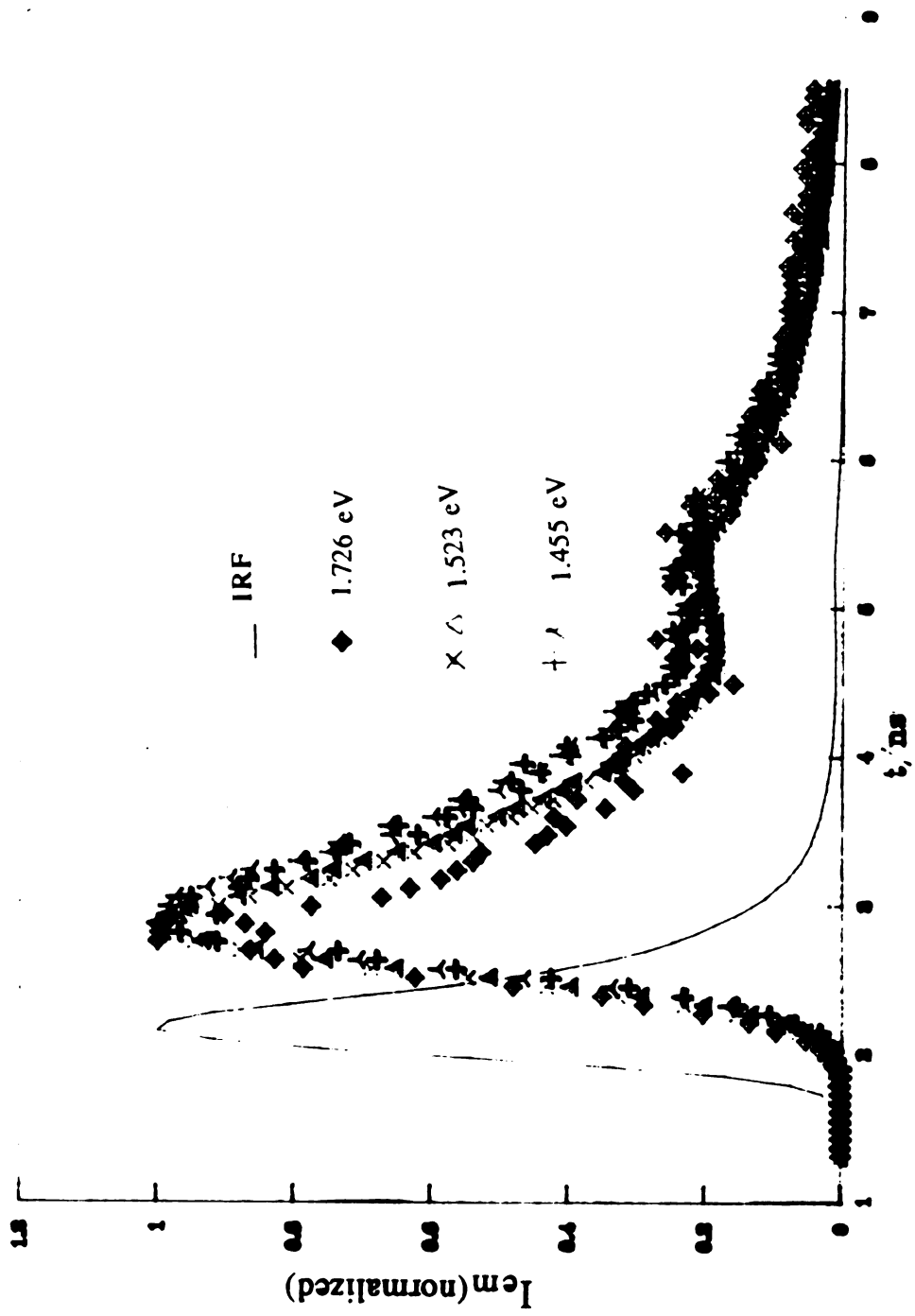

Fig. 9.9. Growth and fluorescence decay curves of $Na^+C221Na^-$ at different emission energies. The sample was at 77 K and the left-most curve is the IRF.

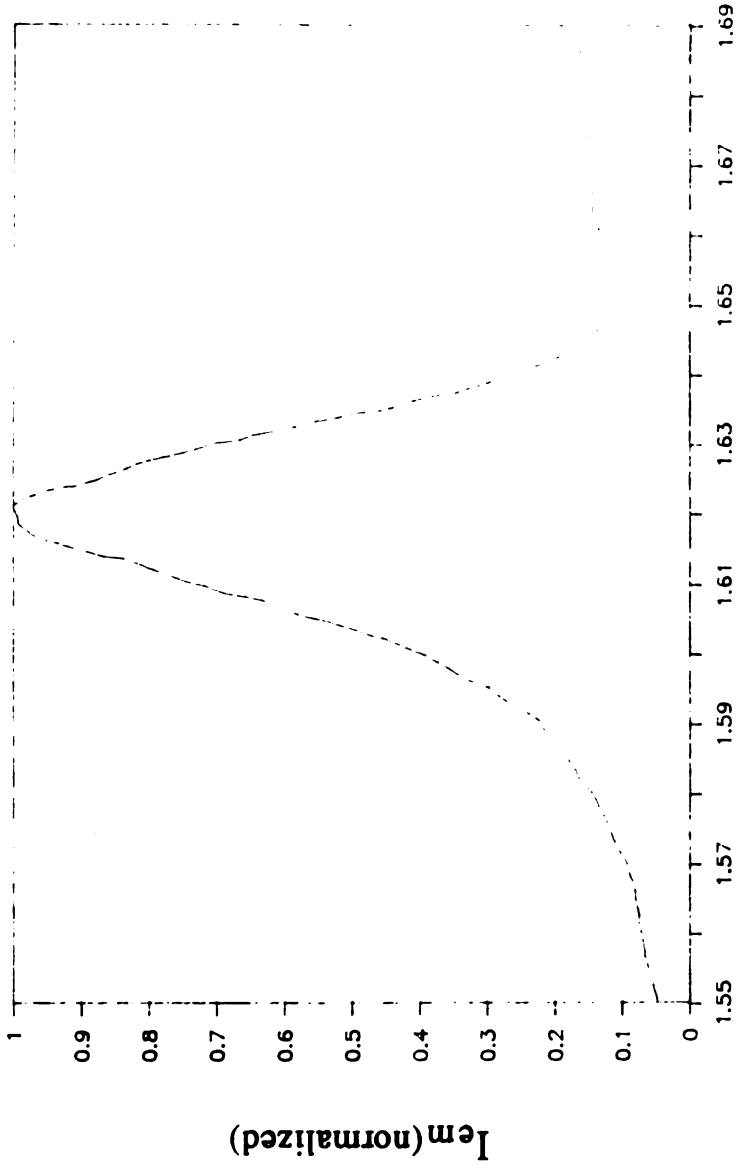

Fig. 9.10. The fluorescence spectrum of $Cs^{+}HMHCYNa^{-}$ at 32 K.

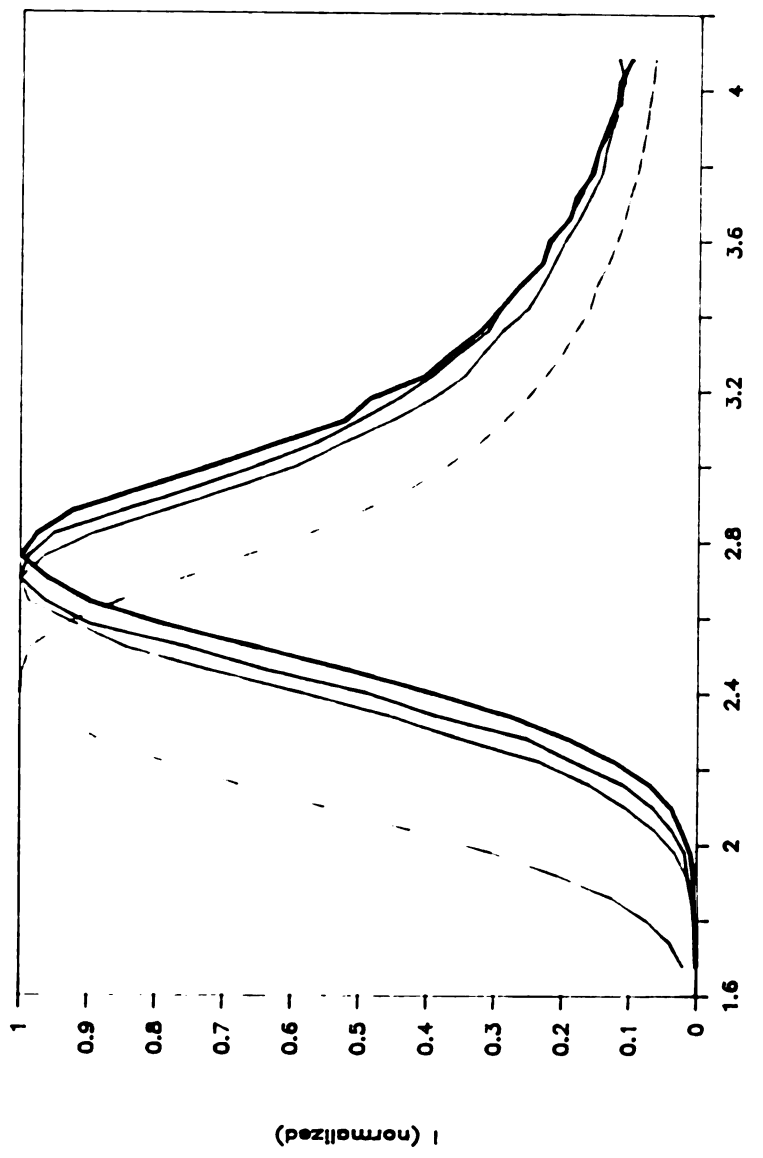

Fig. 9.11. Growth and fluorescence decay curves of $Cs^{+}HMHCYNa^{-}$ at 32K but different energies. The emission energies are, from the right to the left: 1.6 eV, 1.62 eV and 1.635 eV. The left-most curve is the IRF.

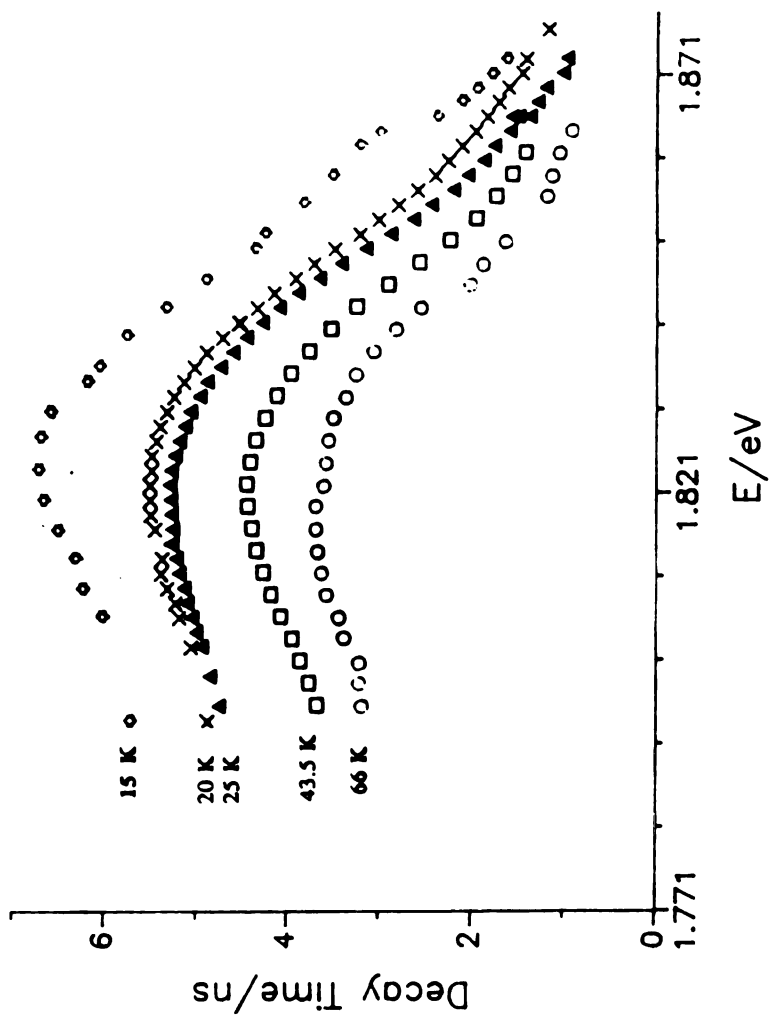

Fig. 9.12. The average fluorescence decay time constant of $Na^{+}C222Na^{-}$ at various temperatures.

CHAPTER X

TIME-DEPENDENT POLARIZATION ANISOTROPY

Introduction

One of the advantages of the single photon counting system is that it can be used to study time dependent polarization anisotropy.

As we have described before, the excitation light used is from lasers and is polarized. Therefore the fluorescence emitted from the emission centers might also be polarized, because only the species with a component of the absorption transition moment in the same direction as the polarization vector of the incident light will be excited. Due to the interaction with other atoms or applied fields, the polarization of the fluorescence compared to that of the incident light may vary from sample to sample or with temperature. For example, a chromophore molecule loses its fluorescence polarization by collision with solvent molecules.[10.1] The fluorescence polarization p can be defined as:[10.2]

$$p = (I_p - I_s)/(I_p + I_s) \qquad (10.1)$$

where I_p and I_s are the fluorescence intensity components parallel and perpendicular to the plane of polarization of the laser beam respectively. The time-dependent anisotropy is defined as:

$$\Delta\tau = \tau_p - \tau_s \qquad (10.2)$$

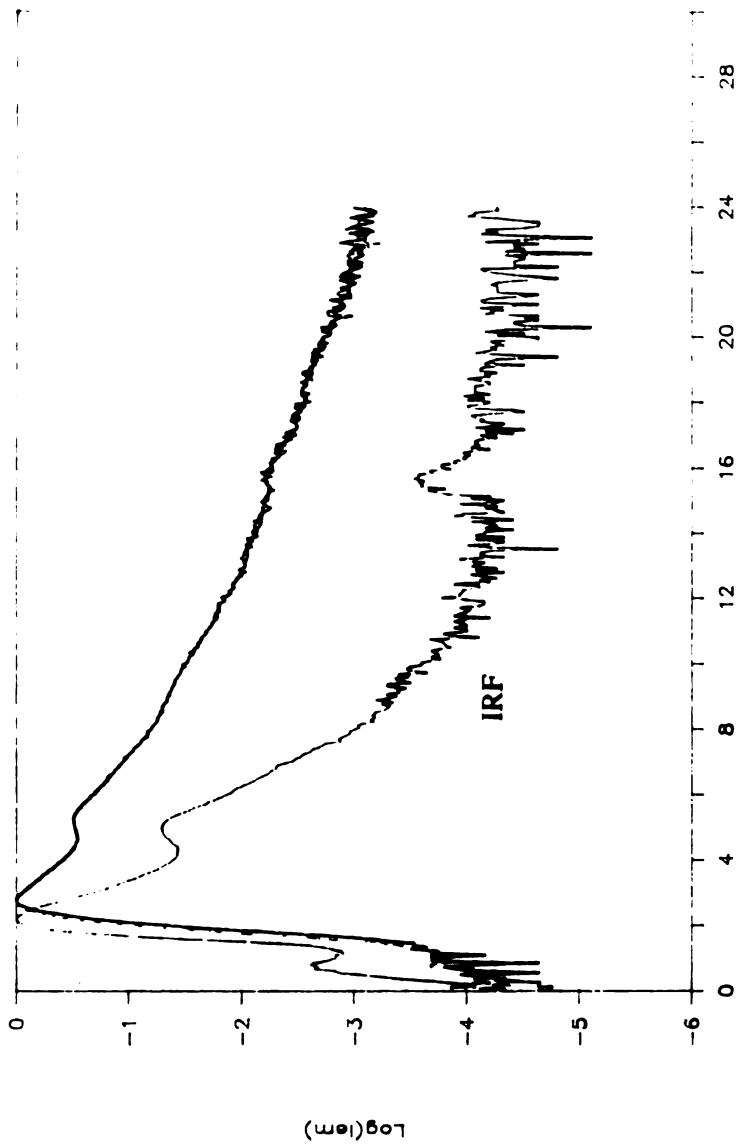

Fig. 10.1. Decay curves of fluorescence at 77 K from undoped polycrystals of $Na^+C222Na^-$. There are three curves in the figure. The left-most one is the IRF, and the others are I_p, and I_s, which are indistinguishable.

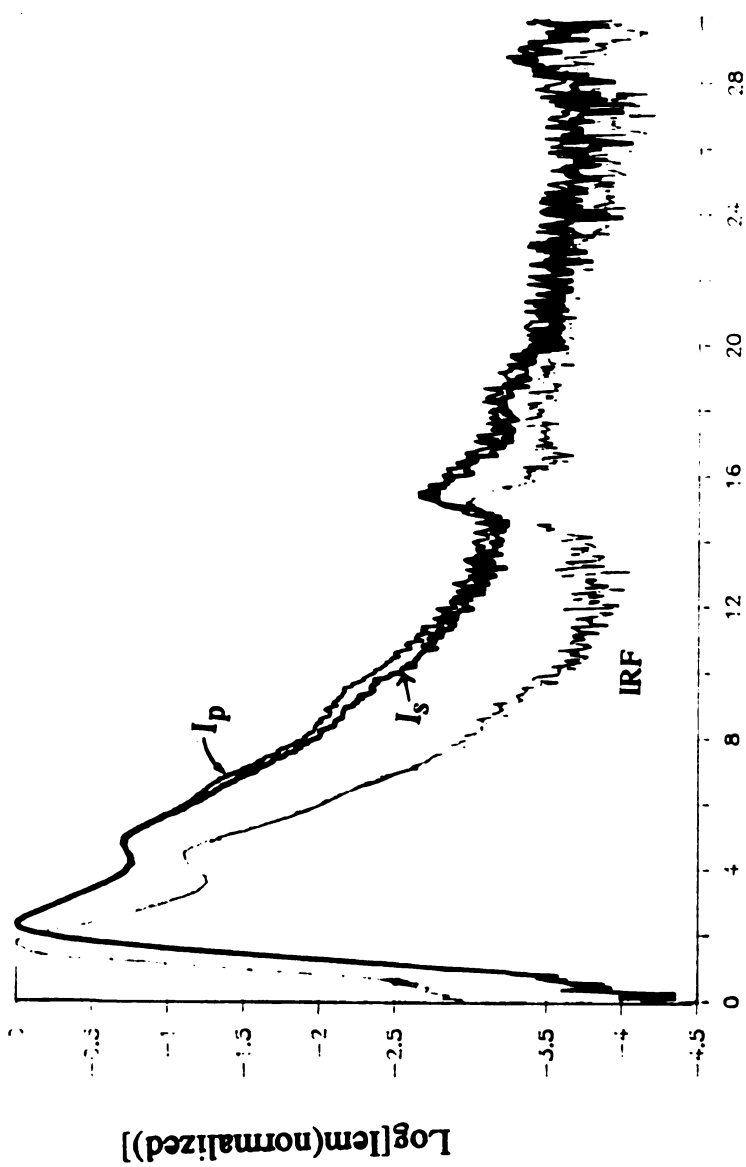

Fig. 10.2. Decay curves of I_p and I_s at 77 K from doped polycrystals of $Na^+C222Na^-$. The left-most curve is the IRF while the other two curves have slightly different decay behaviors. Note that the overall decay is faster than for the undoped sample shown in the previous figure.

where τ_p and τ_s are fluorescence decay constants of I_p and I_s respectively.

Experimentation

The experimental design is shown in Fig. 2.3. We use a polarization rotator inserted before and a polarizing filter after the sample chamber. The instrument configuration was fixed and one parameter, for example the temperature of sample, was changed. We also changed the order of measurement of Ip and Is randomly to check for the presence of systematic errors.

Experimental results

1). Observation of $\Delta\tau$ from $Na^+C222Na^-$.

The samples used to produce the data shown in Fig. 10.1. and Fig. 10.2 were undoped and doped polycrystals respectively. The sample that gave the result shown in Fig. 10.3 was an assembly of single crystals recrystallized from the same preparation used to produce Fig. 10.2. All the decay curves shown in Figs. 10.1 to 10.3 were obtained at 77 K. The sample used to produce Fig. 10.4 was the same sample as that used for Fig. 10.2, but the temperature used for Fig 10.4 was 180 K. The EPR spectra from the three samples were shown previously in Fig. 5.4. From these results we conclude that:

(a). The time-dependent anisotropy $\Delta\tau$, of undoped $Na^+C222Na^-$ and of the doped but then recrystallized sample is zero within experimental error. This study was also carried out at other temperatures below 77 K, with similar results.

(b). The $\Delta\tau$ of doped $Na^+C222Na^-$ is positive.

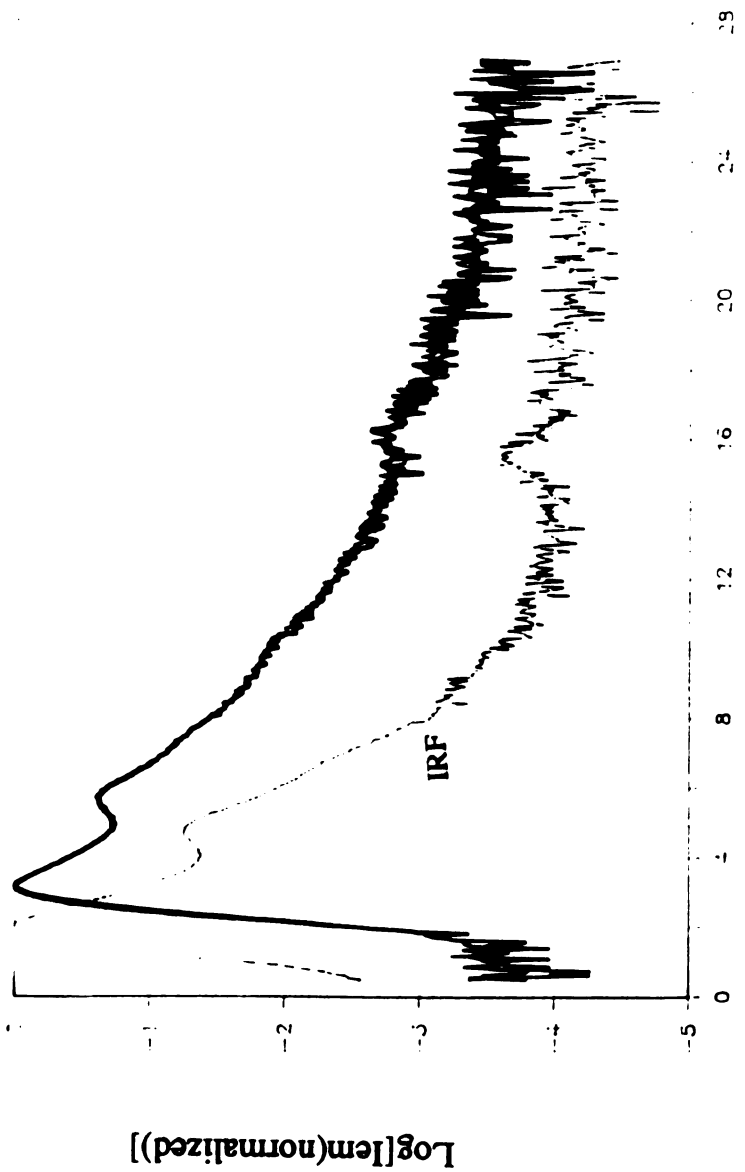

Fig. 10.3. Decay curves of I_p and I_s from single crystals of $Na^+C222Na^-$. The measurement is carried at 77 K. Note again the longer overall lifetime.

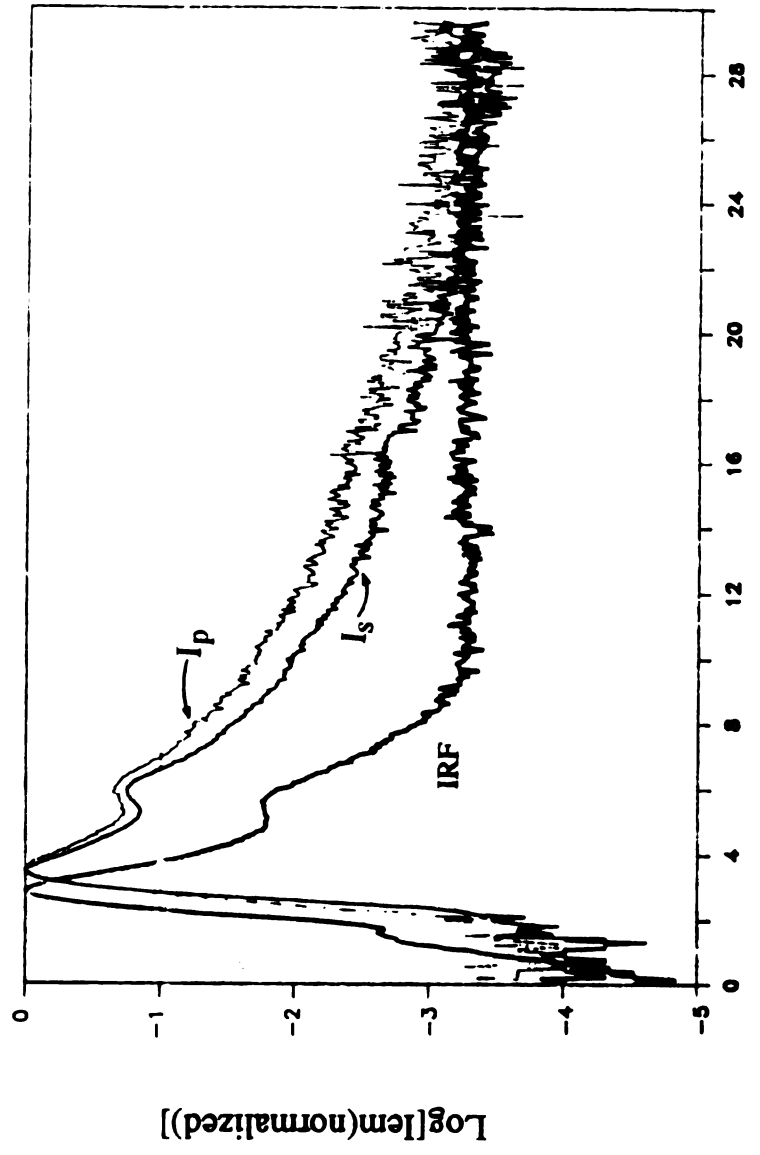

Fig. 10.4. Decay curves of I_p and I_s from defect-doped polycrystals of $Na^+C222Na^-$. The measurement was carried at 180K.

(c). The $_{\Delta}\tau$ of doped $Na^{+}C222Na^{-}$ is larger at 180 K than that at 77 K.

2). Observation of $_{\Delta}\tau$ from $Na^{+}C221Na^{-}$, $Cs^{+}HMHCYNa^{-}$ and $Rb^{+}HMHCYNa^{-}$.

The $_{\Delta}\tau$ results from $Na^{+}C221Na^{-}$, $Cs^{+}HMHCYNa^{-}$ and $Rb^{+}HMHCYNa^{-}$ are shown in Figs. 10.6 to 10.8. These experiments were carried out at 77 K. It is clear from these figures that $_{\Delta}\tau$ for the three compounds are non-zero except that the last one shows practically no anisotropy.

Discussion

A method of leading edge matching after normalization was used in this study, which is a modification of the usual leading edge matching. The method of leading edge matching is described elsewhere,[10.3] which can be used to obtain both P and $_{\Delta}\tau$ as defined in equation (10.1) and (10.2). The modification made to this method is that both Ip and Is, were normalized, which means we do not attempt to determine the magnitude of polarization p. The necessity for this procedure is due to the instrumentation used. Beside the sample under study, the instrument can also affect polarization, because the mirrors, lenses and diffraction grating respond differently to different polarizations of the light.[1.15] However the lifetime constant τ and the τ difference are instrumentation independent. Therefore we decided to study the difference in the decay times, $\Delta\tau = \tau_p - \tau_s$ where τ_p and τ_s are the decay time constants parallel and perpendicular to the excitation.

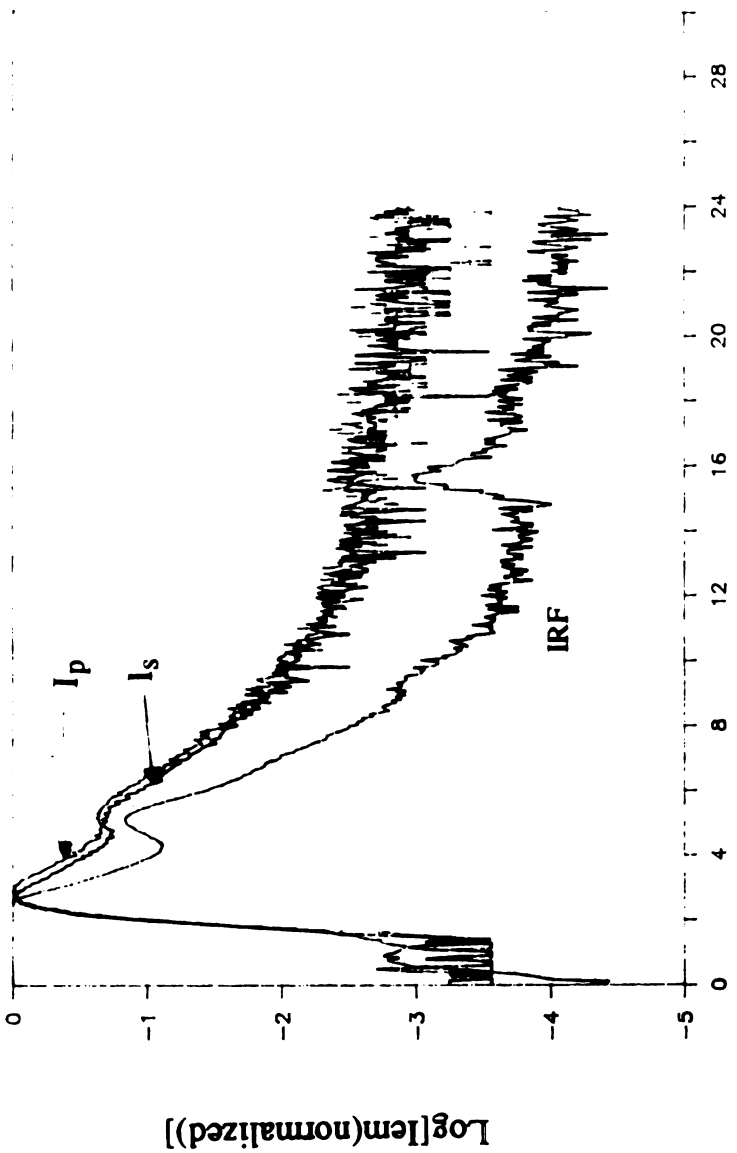

Fig. 10.5. Fluorescence decay curves of I_p and I_s from $Na^+C221Na^-$. The measurement was carried out at 77K.

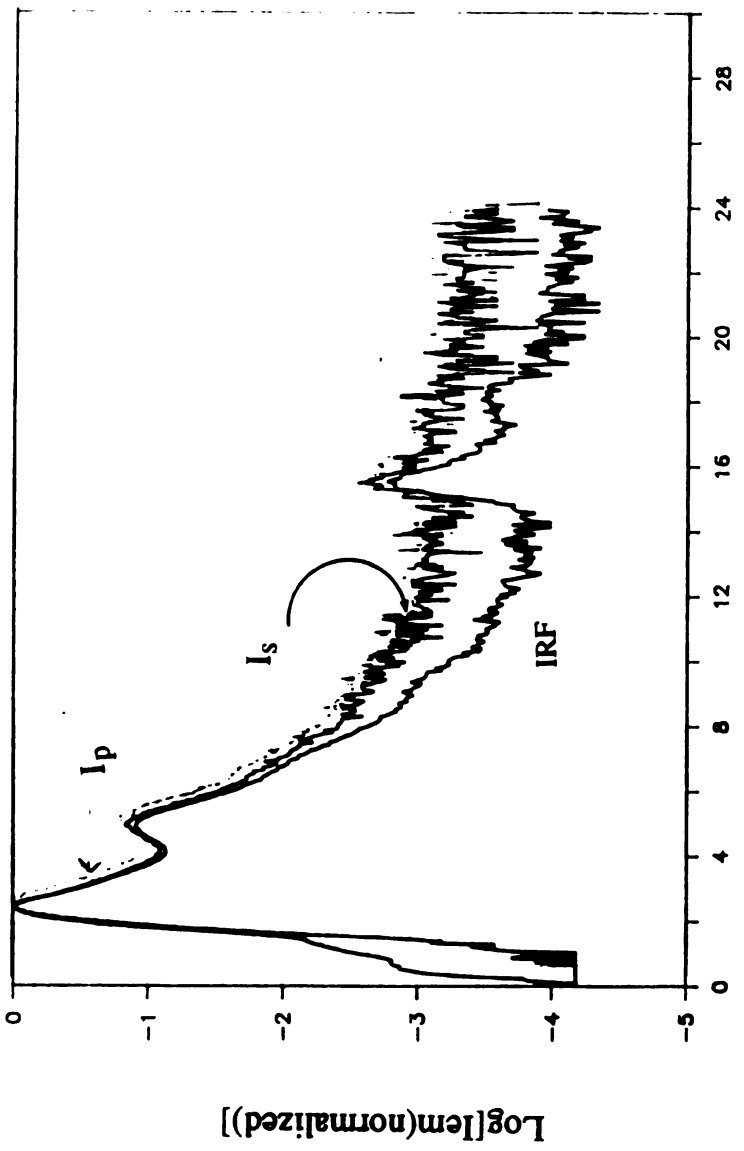

Fig. 10.6. Fluorescence decay curves of I_p and I_s from $Cs^+HMHCYNa^-$. The measurement was carried out at 77K.

This study was designed to see whether the two parameters, temperature and sample doping, introduce any differences in the decay times at two polarization settings. The results are reliable and reproducible. For example, the experimental conditions used to obtain Fig. 10.2, and 10.4 were identical except for temperature. Similarly, the conditions used to obtain Figs. 10.1 and 10.3 were the same except that the sample used for Fig. 10.1 was undoped while that for Fig. 10.3 was doped.

The major observations are:

(1). The value $\Delta\tau = 0$ was found for undoped $Na^+C222Na^-$ crystals.

(2). $\Delta\tau > 0$ for doped $Na^+C222Na^-$, $Na^+C221Na^-$, $Cs^+HMHCYNa^-$.

(3). $\Delta\tau(180\ K) > \Delta\tau(77K)$ for doped $Na^+C222Na^-$.

The observations described above can be explained with the aid of the exciton hopping model. The exciton, being a quasi-particle or elementary excitation wave is mobile. The exciton will travel through the crystalline lattice before being annihilated. The annihilation can be accompanied by photon emission or radiationless decay. The excitation light is polarized and so is the exciton Poynting vector. If the exciton diffuses from one position to another, its polarization memory will be lost by the interaction. As a result, the polarization carried by the fluorescence will be completely lost. On the other hand if the exciton is trapped after hopping only a short distance, and it is converted to a photon, the polarization might be

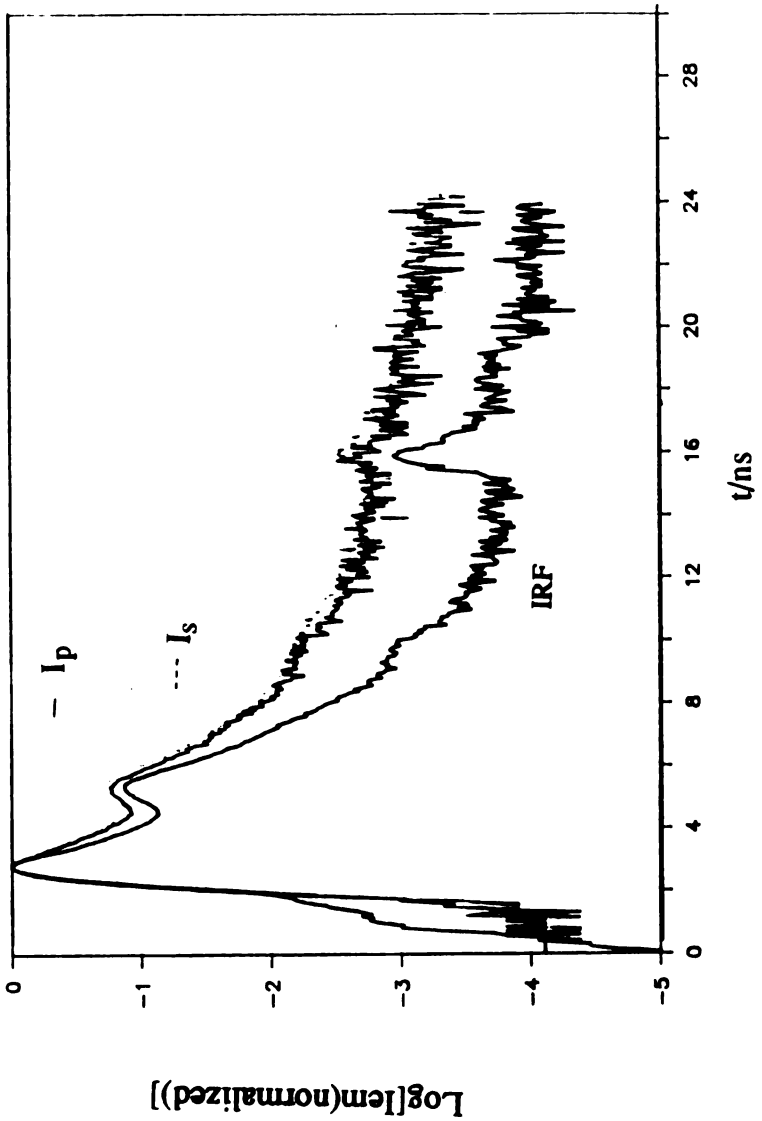

Fig. 10.7. Decay curves of I_p and I_s from $Rb^+HMHCYNa^-$ at 77K.

partially retained. Therefore, the larger the concentration of traps in the crystals, the larger the expected value of $\Delta\tau$.

This interpretation can be used to explain items (1) and (2) above. Compared to the undoped samples, the doped polycrystals sample of $Na^+C222Na^-$ has a higher EPR intensity, which corresponds to a higher concentration of unpaired electrons or traps. Also, according to the EPR studies and magnetic susceptibilities, $Na^+C221Na^-$, $Cs^+HMHCYNa^-$ and $Rb^+HMHCYNa^-$ have significant amounts of unpaired electrons trapped in crystals.[10.4] However, the reason that $\Delta\tau$ is larger at higher temperatures, is not clear at the present time.

The magnitude of polarization p as defined in equation 10.1 or other similar ways is related to the crystalline structure, through the symmetry of the ligand field of the emission centers, and is therefore a very important quantity. The study of polarization p, is significant and should be continued.

References

10.1. R. Drake, et al In "Photophysics of Synthetic Polymers" (Phillips, D. and Roberts, A. J., eds) pp. 150-160. Science Reviews, Northwood, 1982).

10.2. D. Clarke, J. F. Grainger, Polarized Light and Optical measurement, International Series of Monographs in Natural Phylosophy, General Ed. D. Ter Haar, Vo. 35, 1971.

10.3. Chapter 8 of ref. 1.15.

10.4. Dae Ho Shin, Ph. D. Dissertation, Michigan State University, 1992.

CHAPTER XI

SUMMARY AND CONCLUSIONS

This dissertation describes studies of $Na^+C222Na^-$ and five other sodides. The main observations can be summarized as follows:

A. $\underline{Na}^+\underline{C222Na}^-$.

Four fluorescence bands, the G_V band, the "epr band", the 1.76 eV band and the RT band, have been observed.

1). The G_V band is the dominant emission band from high quality crystals at $T < 77$ K. The fluorescence behavior is reversible and reproducible under low excitation densities and low temperatures.

2). The peak position of the G_V band is at 1.84 eV. There are two features of this band that are sample independent. The first feature is that the spectral shape on the high energy side is Gaussian. The second feature is that the spectral shape on the low energy side obeys Urbach's rule.

3). The G_V band results from the superposition of two emission bands, the A band centered at 1.847 eV and the B band centered at 1.823 eV.

4). During radiative transitions, energy transfer from the A band to the B band and to other low energy states occurs, but the individual band position are invariant with time.

5). At relatively high laser excitation densities, fluorescence bleaching and recovery are observed. The fluorescence recovery is more pronounced from defect-doped polycrystals than from undoped crystals.

6). The fluorescence from defect-doped polycrystals is observed to have polarization anisotropy.

7). The "epr band" has a peak position at approximately 1.8 eV which appears to result from defects or trapped electrons doped in the polycrystals.

8). The 1.76 eV-band is broad (as wide as 0.1 eV) and may be a mixture of several bands. The band seems to result from the effect of laser irradiation.

9). The RT band is the band seen at room temperature. The RT band has a peak position of 1.7 eV and a width of 0.5 eV. This band is ascribed to excitonic emission related to grain boundaries in the crystals.

10). Optical absorption studies were carried out on thin films of $Na^+C222Na^-$ and $Rb^+(15C5)_2Na^-$ at 10 to 270 K. When T increases, the absorbance on the low energy side of the spectrum, which is centered at 1.85 eV, increases slightly when $T < 200$ K. However the relative magnitude of this low-energy absorbance increases dramatically at temperatures above about 200 K so that there is a pronounced red-shift of the total spectrum.

B. Other sodides

1). Other sodides have a number of common properties. For example, except for $Rb^+(HMHCY)Na^-$, the main emission band at low temperature is structureless, the emission has a Stoke's shift of about 0.1 eV and the lifetime versus energy has a plateau shape on the low energy side.

2). The fluorescence intensity from sodides other than $Na^+C222Na^-$ is at least three orders-of-magtitude weaker than that from $Na^+C222Na^-$ and the decay time constants are about one order-of-magtitude shorter than that from $Na^+C222Na^-$.

3). Fluorescence emitted from the other sodides studied have a non-zero polarization residual, $\Delta\tau$.

CONCLUSION

The single fluorescence band with peak energy at 1.84 eV observed from high quality crystals is a superposition of two bands, the A band, with energy centered at 1.847 eV, and the B band, with energy centered at 1.822 eV. The B band is responsible for the the Urbach behavior. Both bands are excitonic. There is an energy transfer from A to B.

Defects/trapped-electrons serve to quench the fluorescence which lowers its intensity and increases the decay rate. However these defects/trapped-electrons do not affect the spectral shape.